

MULTIFUNCTIONAL IRON OXIDE NANOPARTICLES
FOR
BIOMEDICAL APPLICATIONS

by

YAOLIN XU

YUPING BAO, COMMITTEE CHAIR

C. HEATH TURNER
STEPHEN M.C. RITCHIE
CHRISTOPHER S. BRAZEL
CAROL DUFFY

A DISSERTATION

Submitted in partial fulfillment of the requirements
for the degree of Doctor of Philosophy
in the Department of Chemical & Biological Engineering
in the Graduate School of
The University of Alabama

TUSCALOOSA, ALABAMA

2014

Copyright Yaolin Xu 2014
ALL RIGHTS RESERVED

ABSTRACT

This dissertation focuses on the preparation of multifunctional nanoparticles through the integration of iron oxide nanoparticles with other desired moieties. Iron oxide nanoparticles have been widely explored in localized therapy, targeted delivery, and magnetic resonance imaging. However, inaccessible MRI instruments for most research labs and lack of targeting ligands limits the further exploration of iron oxide nanoparticles in routine tumor diagnosis and efficient therapy. Therefore, the preparation of dual-imaging or targeted nanoparticles is highly desirable. In our studies, fluorescent gold nanoclusters or anti-disialoganglioside-GD2 monoclonal antibodies are integrated onto iron oxide nanoparticle surfaces. The gold nanoclusters provide additional fluorescent imaging capability, which can be easily accessed in common research labs. The conjugation of cancer cell-targeting antibodies allows for specific localization of nanoparticles. Indeed, these are the two central themes of this dissertation.

To prepare multifunctional nanoparticles, high-quality iron oxide nanoparticles were first synthesized in organic solvents following a modified "heat-up" method. During synthesis, a modification was made by introducing a co-surfactant (trioctylphosphine oxide-TOPO). TOPO facilitated the subsequent ligand exchange process because it weakly bound to nanoparticle surfaces and prevented the formation of densely-packed surfactant coatings. As a result, hydrophilic molecules (such as polyacrylic acid, polyethylenimine, glutathione and dopamine) were capable of replacing the original ligands, yielding water-soluble iron oxide nanoparticles. In addition to water solubility, dopamine coatings offered nanoparticles additional conjugation

capability upon surface oxidization. These surface-oxidized nanoparticles can directly conjugate with amine and/or thiol group-contained molecules through Michael addition and/or Schiff base formation.

Using this conjugation strategy, dual-imaging nanoparticles were prepared by integrating dopamine-coated nanoparticles with protein (such as bovine serum albumin, trypsin and lysozyme) - encapsulated fluorescent gold nanoclusters. All integrated nanoparticles maintained their functionalities and structural integrity in biological environments. Furthermore, effects of protein characteristics on the photo-chemical properties of gold nanoclusters and integrated nanoparticles were systematically examined.

Similarly, cancer cell-targeting molecules (e.g. anti-GD2 monoclonal antibodies) were conjugated onto dopamine-coated nanoparticles. After conjugation, antibodies retained their high targeting specificity, suggested by our cellular targeting studies. More promisingly, conjugated nanoparticles were capable of transporting into cytosols, which opens up new possibilities in cancer-curing drug loading and targeted therapy.

Besides these already-published works, we have studied the biological responses of human monocytes to different surface-charged iron oxide nanoparticles (manuscript in preparation). For dual-imaging nanoparticles, their stability and bio-imaging potential will be evaluated in phorbol myristate acetate (PMA)-treated monocytes using differential interference contrast (DIC) and confocal microscopy.

DEDICATION

This dissertation is dedicated to everyone who helped, guided and encouraged me throughout my Ph.D. career and life.

LIST OF ABBREVIATIONS AND SYMBOLS

<i>NPs</i>	Nanoparticles
<i>MRI</i>	Magnetic resonance imaging
<i>FDA</i>	Food and Drug Administration
<i>PAA</i>	Polyacrylic acid
<i>PEI</i>	Polyethylenimine
<i>GSH</i>	Glutathione
<i>HEPES</i>	4-(2-hydroxyethyl)-1-piperazineethanesulfonic acid
<i>MES</i>	2-(N-morpholino)ethanesulfonic acid
<i>PBS</i>	Phosphate buffered saline
<i>OA</i>	Oleic acid
<i>TOPO</i>	Trioctylphosphine oxide
<i>DMSO</i>	Dimethyl sulfoxide
<i>DMSA</i>	Dimercaptosuccinic acid
<i>TCEP</i>	Tris(2-carboxyethyl)phosphine
<i>EDC</i>	1-ethyl-3-[3-(dimethylamino)propyl]carbodiimide hydrochloride
<i>BSA</i>	Bovine serum albumin
<i>DNA</i>	Deoxyribonucleic acid
<i>Tris</i>	2-amino-2-hydroxymethyl-propane-1,3-diol
<i>FBS</i>	Fetal bovine serum
<i>IMEM</i>	Iscove's Modified Dulbecco's Media
<i>EMEM</i>	Eagle's minimal essential medium
<i>DAPI</i>	4',6-diamidino-2-phenylindole
<i>SPB</i>	Sodium-phosphate buffer
<i>MoAb</i>	Monoclonal antibody
<i>PIs</i>	Isoelectric points

<i>MFI</i>	Mean fluorescence intensity
<i>RU</i>	Relative units
<i>M-H curve</i>	Magnetization versus applied magnetic field curve
<i>TEM</i>	Transmission electron microscopy
<i>HAADF</i>	High-angle annular dark-field imaging
<i>HRTEM</i>	High resolution transmission electron microscopy
<i>EDX</i>	Electron dispersive X-ray
<i>FCS</i>	Fluorescent correlation spectroscopy
<i>FTIR</i>	Fourier transform infrared spectroscopy
<i>ATR</i>	Attenuated total reflectance
<i>DLS</i>	Dynamic light scattering
<i>AGM</i>	Alternating gradient magnetometer
<i>ICP-MS</i>	Inductively coupled plasma mass spectrometry
<i>TC-SPC</i>	Time-correlated single photon counting
<i>UV-vis</i>	Ultraviolet-visible
τ_{ave}	Intensity-weighted average lifetime
χ^2	Reduced chi-square values
$\lambda_{em,max}$	Fluorescent emission peak

ACKNOWLEDGEMENTS

First, I would like to express my sincere thanks to my advisor, Professor Yuping Bao. Without her continuous guidance and encouragement, I could never successfully complete my doctoral projects and Ph.D. career. I also gratefully appreciated her valuable advice and patience on my writing, presentation, and communication skills.

I would also like to thank my committee members, Professor C. Heath Turner, Professor Stephen M.C. Ritchie, Professor Christopher S. Brazel, and Professor Carol Duffy, for their comments and suggestions on my dissertation research. Special thanks go to Professor C. Heath Turner, who greatly supported me on research awards and the fellowship application with his valuable recommendation letters.

I wish to express my thanks to Dr. Kim H. Lackey from Department of Biological Sciences and the research scientist, Dr. Yin Qin, from Alabama Innovation and Mentoring of Entrepreneurs center (AIME). Dr. Lackey greatly helped me on my TEM sample preparation, experimental protocol assessment, and facility training. The assistance from Dr. Qin on FTIR and TGA measurements, and her insightful discussion and detailed analysis significantly advanced my research. Without their great help, I would definitely not have my work finished on schedule.

I also want to thank all the past and current lab members, who are willing to give me help and support whenever I need them.

Last, but certainly not least, I am greatly grateful for the lifelong love, belief, and mental support from my family, which are always the spiritual incentive for me to accomplish more in both my research career and life path.

CONTENTS

ABSTRACT.....	ii
DEDICATION.....	iv
LIST OF ABBREVIATIONS AND SYMBOLS	v
ACKNOWLEDGEMENTS.....	vii
LIST OF TABLES	xii
LIST OF FIGURES	xiii
CHAPTER 1 INTRODUCTION.....	1
REFERENCES	6
CHAPTER 2 WATER-SOLUBLE IRON OXIDE NANOPARTICLES WITH HIGH STABILITY AND SELECTIVE SURFACE FUNCTIONALITY	8
2.1 Introduction.....	9
2.2 Experimental methods	10
2.2.1 Chemicals.....	10
2.2.2 Preparation of the iron oleate complex	11
2.2.3 Synthesis of iron oxide nanoparticles	11
2.2.4 Ligand exchange process	11
2.2.5 Stability tests.....	12
2.2.6 Characterization of iron oxide nanoparticles	12
2.3 Results and discussions.....	13
2.4 Conclusion	25
2.5 References.....	27
2.6 Supporting information.....	30
2.6.1 Calculation of the required amount of ligands for the exchange process.....	30
2.6.2 Fluorescent dye conjugation on GSH-coated NPs	30
2.6.3 Effect of the divalent cation on the stability of charged NPs	31

CHAPTER 3	MAKE CONJUGATION SIMPLE: A FACILE APPROACH TO INTEGRATED NANOSTRUCTURES	33
3.1	Introduction.....	34
3.2	Experimental methods	36
3.2.1	Dopamine attachment onto iron oxide nanoparticles	36
3.2.2	Surface activation of dopamine-coated iron oxide nanoparticles	37
3.2.3	Preparation of fluorescent gold nanoclusters	37
3.2.4	Integration of activated iron oxide nanoparticles with fluorescent gold nanoclusters.....	37
3.2.5	Characterization	38
3.3	Results and discussion	38
3.4	Conclusion	48
3.5	References.....	50
3.6	Supporting information.....	52
3.6.1	Dopamine oxidation.....	52
3.6.2	Role of specific amino acids in nanocluster formation.....	52
3.6.3	Bright field TEM image of the integrated nanoparticles	54
3.6.4	Stability tests of integrated nanoparticles	55
CHAPTER 4	THE ROLE OF PROTEIN CHARACTERISTICS IN THE FORMATION AND FLUORESCENCE OF AU NANOCCLUSERS	58
4.1	Introduction.....	59
4.2	Experiments	61
4.2.1	Chemicals.....	61
4.2.2	Synthesis of protein-encapsulated gold nanoclusters	61
4.2.3	Lifetime measurements	62
4.2.4	Stability tests.....	62
4.2.5	Immobilization effects	63
4.2.6	Characterization	64
4.3	Results and discussion	64
4.4	Conclusions.....	82
4.5	References.....	84
4.6	Supporting information.....	87

CHAPTER 5	A LINKER-FREE METHOD FOR THE EFFECITVE CONJUGATION OF BIOACTIVE MOIETIES ONTO IRON OXIDE NANOPARTICLES	93
5.1	Introduction.....	95
5.2	Materials and methods	97
5.2.1	Materials	97
5.2.2	Nanoparticle synthesis	98
5.2.3	Surface modification.....	98
5.2.4	Antibody conjugation.....	98
5.2.5	Cell culture.....	99
5.2.6	Cellular targeting with antibody conjugated nanoparticles	100
5.2.7	Cell targeting and competition experiments	101
5.3	Results and discussion	102
5.3.1	Synthesis and functionalization of dopamine-coated iron oxide nanoparticles.....	102
5.3.2	Characterization of antibody-conjugated iron oxide nanoparticles	106
5.3.3	Cell targeting evaluation of antibody-conjugated iron oxide nanoparticles.....	107
5.3.4	Cellular uptake of antibody-conjugated nanoparticles	111
5.4	Conclusion	115
5.5	References.....	117
5.6	Supporting information	120
CHAPTER 6	CONCLUSIONS AND FUTURE WORKS.....	121
REFERENCES	126

LIST OF TABLES

4.1 The characteristics of four model proteins.....	65
---	----

LIST OF FIGURES

2.1	Schematic illustration of the ligand exchange process using PAA, PEI, or GSH	14
2.2	As-synthesized iron oxide NPs coated with OA and TOPO ligands: (a) TEM image, (b) DLS plot, and (c) FTIR spectrum	15
2.3	Water-soluble NPs coated with PAA, PEI, and GSH: (a-c) TEM images, (d-f) photographs, (g) DLS plots, (h) zeta-potential measurements, and (i) magnetic measurements.....	17
2.4	FTIR spectra of the ligands and ligand-coated NPs: (a) PAA, (b) PEI, and (c) GSH	19
2.5	DLS plots of iron oxide NPs coated with (a) PAAs of different molecular weights, (b) PEI of different molecular weights, and (c) PAA polymers at different ligand-to-NP ratios.....	21
2.6	DLS plots of NP water dispersions at different pH: (a) PAA-coated, (b) PEI-coated, and (c) GSH-coated	22
2.7	NP water dispersions in PBS, HEPES, MES, or NaCl solutions: (a-c) DLS plots of PAA-, PEI-, and GSH-coated NPs; (d-f) zeta-potentials of PAA-, PEI-, and GSH-coated NPs ..	23
S2.1	The emission (black) and excitation (red) scans of the dye-conjugated GSH coated NPs after magnetic separation	31
S2.2	Photographs of GSH-coated NP dispersions: (a) original solution, (b) after addition of Mg^{2+} , and (c) Mg^{2+} removed from solution.....	32
3.1	(a) TEM image of the dopamine-coated iron oxide nanoparticles (10 nm), (b) FTIR spectra of free dopamine, dopamine-coated, and activated dopamine-coated nanoparticles, and (c) time-dependent UV-vis spectra of dopamine-coated iron oxide nanoparticles after activation	40
3.2	BSA-encapsulated Au nanoclusters: (a) fluorescent emission excited at 520 nm and excitation scan for emission peak of 680 nm plots, (b) photographs of nanocluster solution under room (left) and UV light (right), (c) bright-field TEM image, and (d) HAADF-TEM image	41
3.3	Integrated structure of iron oxide nanoparticles and Au nanoclusters: (a) fluorescent emission (excited at 520 nm) and excitation scans for 680 nm emission, (b) photographs of free BSA-Au nanoclusters-1 and the integrated nanostructures-2 under a 365 nm UV radiation, (c) magnetic moment versus applied magnetic fields curves of nanoparticles	

	and the integrated nanostructures, (d) photographs of the integrated nanostructures under magnetic fields	45
3.4	Integrated structure of iron oxide nanoparticles and Au nanoclusters: (a) HRTEM image, (b) HAADF-TEM image, (c) DLS plots, (d) zeta-potentials, and (e) EDX spectrum.....	47
S3.1	UV-vis absorption spectra of (a) time-dependent oxidation of free dopamine solution, and (b) dopamine-coated iron oxide nanoparticle solution	52
S3.2	UV-vis absorption spectra of HAuCl ₄ solution at pH 2-the original solution, pH 6-right after dilution into water, 30 min and 1 h after dilution.....	53
S3.3	UV-vis absorption spectra of HAuCl ₄ and BSA (a), arginine (b), Lysine (c), histidine (d) reaction solution, and (e & f) photographs of reaction mixtures	54
S3.4	Bright field TEM image of the integrated nanoparticles	55
S3.5	The integrated nanoparticles in HEPES buffer: (a) HAADF image, and (b) bright field TEM image	56
S3.6	UV-vis absorption spectra of the integrated nanoparticles in various buffers: (a), PBS, (b) HEPES, (c), MES, (d) reaction solution and (e & f) photographs of reaction mixtures....	57
4.1	Protein-encapsulated Au nanoclusters: fluorescent emission (black)/excitation (red) spectra and TEM images of Au nanoclusters generated from BSA (a and e), trypsin (b and f), lysozyme (c and g), and pepsin (d and h).....	66
4.2	Fluorescent emission (black)/excitation (red) spectra and TEM images of Au nanoclusters generated from excess trypsin (a and b), and lysozyme (c and d)	69
4.3	Time-resolved fluorescence lifetime analysis of: (a) Lyso-Au (b) Try-Au, and (c) BSA-Au nanoclusters.....	71
4.4	FTIR spectra of protein-encapsulated Au nanoclusters and its corresponding free proteins under denatured conditions: (a) BSA, (b) trypsin, and (c) lysozyme	74
4.5	pH and buffer condition effects on the fluorescent emission of Au nanoclusters generated by: (a-c) BSA, (d-f) trypsin, and (g-i) lysozyme	76
4.6	Temperature and UV-radiation effects on the fluorescent emissions of the Au nanoclusters generated by: (a-c) BSA, (d-f) trypsin, and (g-i) lysozyme.....	78
4.7	Protein-Au nanoclusters immobilized on iron oxide nanoparticle surface: fluorescent emission/excitation plots and TEM images of BSA (a and b), trypsin (c and d), and lysozyme (e and f).....	81
4.8	The fluorescent emission/excitation plots of protein-Au nanoclusters immobilized on the inner surface of glass vials: (a) BSA, (b) trypsin, and (c) lysozyme	82

S4.1	UV-vis spectra of protein-Au nanoclusters generated from trypsin and lysozyme	87
S4.2	(a) a UV-visible spectrum of pepsin-Au nanostructures, (b) a photo image of pepsin-Au nanoparticles in solution	88
S4.3	Fluorescent emission and excitation plots of protein-Au nanoclusters generated with the same amine group to Au ratios: (a) BSA, (b) trypsin, and (c) lysozyme; and protein-Au nanoclusters generated with the same tyrosine/tryptophan to Au ratios: (d) BSA, (e) trypsin, and (f) lysozyme	89
S4.4	FTIR spectra of proteins and denatured proteins in basic environments: (a) BSA, (b) trypsin, and (c) lysozyme.....	90
S4.5	Fluorescent emission plots of protein-Au nanoclusters in solution and powder forms (a) BSA-Au nanoclusters, (b) trypsin-Au nanoclusters, and (c) lysozyme-Au nanoclusters	91
S4.6	Fluorescent emission/excitation plots of Au nanoclusters before and after addition of iron oxide nanoparticles: (a and d) BSA-Au nanoclusters, (b and e) trypsin-Au nanoclusters, and (c and f) lysozyme-Au nanoclusters.....	92
5.1	Dopamine functionalized iron oxide nanoparticles: (a) TEM image, (b) high resolution TEM image, (c) DLS plot, and (d) zeta-potential plot.....	104
5.2	FTIR spectra of dopamine-coated iron oxide nanoparticles before and after oxidation..	105
5.3	Antibody conjugated iron oxide nanoparticles: (a) TEM image, (b) Zeta-potential plot, (c) DLS plot, and (d) FTIR spectrum	107
5.4	Binding evaluation of hu14.18MoAb-conjugated iron oxide nanoparticles to neuroblastoma cells (CHLA-20): (Fluorescence microscopy (400X) of CHLA-20 cells or normal fibroblasts treated with unconjugated (a, c) or antibody-conjugated (b, d) nanoparticles and Alexa 488-anti-human IgG antibody. (e) Flow cytometry of cell auto-fluorescence (clear histogram) and antibody-conjugated nanoparticles bound to cells (tinted histogram). (f) Flow cytometry binding curves of hu14.18MoAb (antibody) and hu14.18MoAb-conjugated nanoparticles (antibody-NP) to CHLA-20 cells. Averages \pm SD of three experiments.NP, nanoparticles. DAPI, nuclear counterstain. MFI, mean fluorescence intensity. RU, relative units	109
5.5	Perls staining using Prussian blue reaction detecting iron for (a) unconjugated and (b) antibody-conjugated iron oxide nanoparticles.(c) Quantification by ferrozine reaction of the iron content of CHLA-20 cells following treatment with medium alone (no NP), unconjugated (NP) or antibody-conjugated nanoparticles (antibody-NP). (d) Flow cytometry evaluation of the biocompatibility of the dopamine-coated iron oxide nanoparticles by propidium iodide exclusion, following cell treatment with medium alone (no NP), unconjugated (NP) or antibody-conjugated nanoparticles (antibody-NP). Averages \pm SD of three independent experiments are shown.....	111

5.6	Comparison of nanoparticle recognition and internalization on CHLA-20 and PC-3 cells: (a and c) cells treated with dopamine-coated nanoparticles for four hours, (e and g) cells treated with antibody-conjugated NPs for four hour, and (i and k) cells treated with antibody-conjugated NPs for 12 hour, (b, d, f, h, j ,l) higher magnification of the areas that red/blue-dashed circle indicates	113
5.7	The binding competition experiments on CHLA-20 cells: (a) GD2 unblocked CHLA-20 cells treated with antibody-conjugated NPs for four hours, (c) GD2 blocked CHLA-20 cells treated with antibody-conjugated nanoparticles for four hours. (b and d) Higher magnification of the areas that red-dashed circle indicates	114
5.8	Schematic drawing of Hu14.18MoAb antibody conjugation with iron oxide nanoparticles (left section) and their targeting efficiency tests on GD2-positive (CHLA-20) and GD2-negative (PC-3) cells (right section)	116
S5.1	HRTEM images of dopamine-coated iron oxide nanoparticles, where the possible poly-dopamine patches were highlighted with red circles	120
S5.2	DLS plot of iron oxide nanoparticles in hexane	120

CHAPTER 1

INTRODUCTION

Iron oxide nanoparticles have been extensively studied for biomedical applications, such as biosensing,¹ magnetic resonance imaging (MRI),² magnetic bio-separation,³ drug delivery⁴ and localized hyperthermia therapy.⁵ Among various applications, the use of iron oxide nanoparticles as MRI contrast agents⁶ and for iron deficiency therapy⁷ has been clinically approved by the Food and Drug Administration (FDA). However, the sensitivity and imaging resolution of MRI limits its use in monitoring biological process on molecular level,⁸ and MRI scanners are normally inaccessible to common research labs. Therefore, introducing other imaging capabilities to iron oxide nanoparticles will expand their applications in both fundamental research and technological fields.

The clinical use of iron oxide nanoparticles as MRI contrast agents has been limited mainly due to lack of targeting ligands, and the nanoparticles could only passively accumulate in the liver and spleen.^{2, 9} Therefore, conjugation of targeting moieties onto iron oxide nanoparticle surfaces can greatly broaden their applicability, improve imaging efficiency, and reduce administration doses.

In this dissertation, I mainly focus on the preparation of two types of multifunctional nanoparticles: (1) gold nanocluster-integrated nanoparticles for additional high-sensitivity fluorescent imaging, and (2) antibody-conjugated nanoparticles for efficient and selective cancer cell targeting. To achieve multi-functionality on a single platform, each component should be

well developed and characterized. Most importantly, the integration method needs to be carefully selected to perform efficient conjugation between components without any loss of properties. *In vitro* biological evaluations of the integrated nanostructures are also essential, which includes studies of the nanoparticle stability, integrity and performance in biological buffers, physiological conditions, and cellular cultures.

The first step to achieve multifunctional nanoparticles is the preparation of high quality iron oxide nanoparticles. Currently, high-quality nanoparticles are generally synthesized in organic solvents at high temperatures.¹⁰⁻¹⁴ For our work, iron oxide nanoparticles were prepared using a modified "heat-up" method, which allows the production of iron oxide nanoparticles with great size and shape control. This process also has great potential for scale-up reactions. One of the keys to our procedure is the introduction of trioctylphosphine oxide (TOPO) as a co-surfactant during nanoparticle synthesis. This modification is critical for the subsequent ligand exchange reaction for the preparation of water-soluble nanoparticles. First, TOPO weakly bound to the nanoparticle surfaces.¹⁵ Second, the bulky structure of TOPO prevented the formation of densely-packed surfactant layers on nanoparticle surfaces.¹⁶ Therefore, the weak binding and loose packing make TOPO sites as starting points for hydrophilic ligands to attached and facilitate the ligand exchange reactions.

Utilizing the weak binding of TOPO, we effectively attached various hydrophilic molecules onto iron oxide nanoparticle surfaces, such as polyacrylic acid (PAA), polyethylenimine (PEI), and glutathione (GSH). All three molecules have stronger binding affinity to iron oxide nanoparticle surfaces than that of TOPO, which enabled the successful replacement of hydrophobic coatings. The resultant water-soluble iron oxide nanoparticles presented great solubility, selective surface functionality and surface charges (positive and negative).

Nanoparticle surface charges resulted from ionized functional groups of hydrophilic ligands, and their ionizable properties varied with the pH of the nanoparticle solutions. Additionally, the iron oxide nanoparticles showed great stability in Good's buffers (such as 4-(2-hydroxyethyl)-1-piperazineethanesulfonic acid (HEPES) and 2-(N-morpholino) ethanesulfonic acid (MES)), but nanoparticle aggregation was observed in PBS buffer. This buffer-dependent stability provided new insight into the behaviors of water-soluble nanoparticles in biological environments, and valuable information for further bioconjugation.

Using the same ligand exchange method, we also successfully attached dopamine onto nanoparticle surfaces, and this surface functionalization is critical for the subsequent conjugation. The catechol groups on nanoparticle surfaces can be easily oxidized under alkaline conditions. The oxidized or activated form, dopamine-quinone, can effectively react with amine and/or thiol group-contained molecules through Michael addition and/or Schiff base formation.¹⁷ Compared to the traditional linker-chemistry method,¹⁸ the use of activated dopamine coatings for direct conjugation eliminates the use of chemical linkers and harsh conjugation conditions, while providing robust binding and preserving the activity of conjugating molecules to the greatest extent. Specific affinity interaction using biotin-streptavidin was another commonly-used conjugation route.¹⁹ But reduced specificity was observed from biotin-labeled nanoparticles due to their non-specific interactions with any biotin-binding proteins.

With our innovative and facile conjugation strategy, magnetic-fluorescent nanoparticles were prepared by integrating dopamine-coated nanoparticles with protein (such as bovine serum albumin, trypsin and lysozyme) - encapsulated fluorescent gold nanoclusters.^{20, 21} Fluorescent components were chosen because of their high sensitivity of *in vitro* biomolecule detection^{22, 23} and *in vivo* tumor imaging,²⁴ which compensated for the MRI sensitivity limitation. All

integrated nanoparticles maintained their functionalities and structural integrity in biological environments. Furthermore, the effects of protein characteristics on formation and fluorescent properties of gold nanoclusters were systematically examined. The experimental results indicated that the nanocluster formation was greatly affected by the balance of amine- and tyrosine/tryptophan-containing residues. The cysteine contents had great impact on the nanocluster fluorescent properties. The protein size critically influenced the nanocluster long-term stability and photo-stability, and also had effects on fluorescent properties of immobilized nanoclusters. These detailed studies provide valuable information in the design and synthesis of fluorescent gold nanoclusters, subsequently benefiting their potential applications in biological and biomedical fields.

Iron oxide nanoparticles with cancer cell-targeting functionality were also successfully prepared by conjugating anti-disialoganglioside-GD2 monoclonal antibodies with activated, dopamine-coated nanoparticles. Disialoganglioside-GD2 antigens are expressed on neuroblastoma cancer cells, tumors of neuroectodermal origin, as well as most melanomas,^{27, 28} but rarely on healthy tissues.²⁹ With the specific reorganization of GD2 antigen-expressing cells, efficient targeting and therapy can be accomplished. The biological activities of the antibody were fully retained after conjugation onto nanoparticles, suggested by the selective targeting experiments performed on GD2-positive cancer cells. Promisingly, the membrane-anchored nanoparticles were capable of transporting into cytosols, which open up new possibilities in cancer-curing drug loading and targeted therapy in the future.

Chapter 2 presents the preparation and characterization of high-quality water-soluble iron oxide nanoparticles, including buffer-dependent nanoparticle stability tests. In chapter 3, iron oxide nanoparticles were functionalized with dopamine, a molecule that can be activated in basic

solution for further conjugation. After activation, the nanoparticles can directly integrate with protein-encapsulated gold nanoclusters for the preparation of magnetic-fluorescent dual-imaging nanoparticles. The integrated nanostructures of dopamine-coated nanoparticles with trypsin- and lysozyme-gold nanoclusters are presented in chapter 4. In this chapter, the effects of protein characteristics on the formation, fluorescence, photo-stability and immobilization of gold nanoclusters are also discussed in detail. Chapter 5 mainly focuses on the preparation and characterization of antibody-conjugated nanoparticles. The targeting capability of the antibody after conjugation was further studied on GD2 positive cancer cells. Finally, the on-going work of the effects of nanoparticle surface charges on the innate immune response of human monocyte cells and future work on the integrity of the integrated nanostructures in biological systems will be introduced in Chapter 6..

REFERENCES

1. Perez, J. M.; Josephson, L.; O'Loughlin, T.; Hogemann, D.; Weissleder, R. *Nat. Biotechnol.* **2002**, *20*, 816-820.
2. Hamm, B.; Staks, T.; Tapuiz, M.; Maibauer, R.; Speidel, A.; Huppertz, A.; Frenzel, T.; Lawaczeck, R.; Wolf, K. J.; Lange, L. *Jmri-J. Magn. Reson. Im.* **1994**, *4*, 659-668.
3. Setchell, C. H. *J. Chem. Technol. Biotechnol. B-Biotechnol.* **1985**, *35*, 175-182.
4. Jain, T. K.; Morales, M. A.; Sahoo, S. K.; Leslie-Pelecky, D. L.; Labhasetwar, V. *Mol. Pharm.* **2005**, *2*, 194-205.
5. Pankhurst, Q. A.; Connolly, J.; Jones, S. K.; Dobson, J. *J. Phys. D-Appl. Phys.* **2003**, *36*, R167-R181.
6. Tassa, C.; Shaw, S. Y.; Weissleder, R. *Acc. Chem. Res.* **2011**, *44*, 842-852.
7. Schwenk, M. H. *Pharm.* **2010**, *30*, 70-79.
8. Fang, C.; Zhang, M. Q. *J. Mater. Chem.* **2009**, *19*, 6258-6266.
9. Baiu, D. C.; Brazel, C. S.; Bao, Y. P.; Otto, M. *Curr. Pharm. Des.* **2013**, *19*, 6606-6621.
10. Rockenberger, J.; Scher, E. C.; Alivisatos, A. P. *J. Am. Chem. Soc.* **1999**, *121*, 11595-11596.
11. Hyeon, T.; Lee, S. S.; Park, J.; Chung, Y.; Bin Na, H. *J. Am. Chem. Soc.* **2001**, *123*, 12798-12801.
12. Xie, J.; Peng, S.; Brower, N.; Pourmand, N.; Wang, S. X.; Sun, S. H. *Pure Appl. Chem.* **2006**, *78*, 1003-1014.
13. Park, J.; An, K. J.; Hwang, Y. S.; Park, J. G.; Noh, H. J.; Kim, J. Y.; Park, J. H.; Hwang, N. M.; Hyeon, T. *Nat. Mater.* **2004**, *3*, 891-895.
14. Yu, W. W.; Falkner, J. C.; Yavuz, C. T.; Colvin, V. L. *Chem. Comm.* **2004**, *20*, 2306-2307.
15. Palchoudhury, S.; Xu, Y. L.; An, W.; Turner, C. H.; Bao, Y. P. *J. Appl. Phys.* **2010**, *107*, 09B311.
16. Bao, Y. P.; Beerman, M.; Pakhomov, A. B.; Krishnan, K. M. *J. Phys. Chem. B* **2005**, *109*, 7220-7222.
17. Lee, H.; Rho, J.; Messersmith, P. B. *Adv. Mater.* **2009**, *21*, 431-434.

18. Park, J. H.; von Maltzahn, G.; Zhang, L. L.; Derfus, A. M.; Simberg, D.; Harris, T. J.; Ruoslahti, E.; Bhatia, S. N.; Sailor, M. J. *Small* **2009**, *5*, 694-700.
19. Wilchek, M.; Bayer, E. A.; Livnah, O. *Immunol. Lett.* **2006**, *103*, 27-32.
20. Xu, Y. L.; Palchoudhury, S.; Qin, Y.; Macher, T.; Bao, Y. P. *Langmuir* **2012**, *28*, 8767-8772.
21. Xu, Y. L.; Sherwood J.; Qin, Y.; Crowley D.; Bonizzonic M.; Bao Y. *Nanoscale* **2014**, *3* 1515–1524.
22. Weiss, S. *Science* **1999**, *283*, 1676-1683.
23. Sako, Y. *Mol. Syst. Biol.* **2006**, *2*, 56.
24. Olson, E. S.; Jiang, T.; Aguilera, T. A.; Nguyen, Q. T.; Ellies, L. G.; Scadeng, M.; Tsien, R. Y. *Proc. Natl. Acad. Sci. U. S. A.* **2010**, *107*, 4311-4316.
25. Yang, Q.; Liu, J.; Chen, H.; Wang, X.; Huang, Q.; Shan, Z. *Prog. Chem.* **2011**, *23*, 880-892.
26. Liu, C. L.; Wu, H. T.; Hsiao, Y. H.; Lai, C. W.; Shih, C. W.; Peng, Y. K.; Tang, K. C.; Chang, H. W.; Chien, Y. C.; Hsiao, J. K.; Cheng, J. T.; Chou, P. T. *Angew. Chem., Int. Ed.* **2011**, *50*, 7056-7060.
27. Modak, S.; Cheung, N. K. *Cancer Invest.* **2007**, *25*, 67-77.
28. Yoshida, S.; Fukumoto, S.; Kawaguchi, H.; Sato, S.; Ueda, R.; Furukawa, K. *Cancer Res.* **2001**, *61*, 4244-4252.
29. Navid, F.; Santana, V. M.; Barfield, R. C. *Curr. Cancer Drug Targets* **2010**, *10*, 200-209.

CHAPTER 2

WATER-SOLUBLE IRON OXIDE NANOPARTICLES WITH HIGH STABILITY AND SELECTIVE SURFACE FUNCTIONALITY

(Published in *Langmuir* **2011**, 27, 8990-8997)

Yaolin Xu, Ying Qin, Soubantika Palchoudhury, and Yuping Bao*

ABSTRACT

The water dispersibility and stability of high quality iron oxide nanoparticles synthesized in organic solvents are major issues for biomedical and biological applications. In this paper, a versatile approach for preparing water soluble iron oxide nanoparticles with great stability and selective surface functionality ($-\text{COOH}$, $-\text{NH}_2$, or $-\text{SH}$) was demonstrated. The hydrophobic nanoparticles were first synthesized by the thermal decomposition of an iron oleate complex in organic solvent. Subsequently, the hydrophobic coatings of nanoparticles were replaced with polyacrylic acid, polyethylenimine, or glutathione, yielding charged nanoparticles in aqueous solution. Two parameters were found to be critical for obtaining highly stable nanoparticle dispersions: the original coating and the surfactant-to-nanoparticle ratio. These charged nanoparticles exhibited different stabilities in biological buffers, which were directly influenced by the surface coatings. This report will provide significant practical value in exploring the biological or biomedical applications of iron oxide nanoparticles.

2.1 Introduction

Iron oxide nanoparticles (NPs) have been extensively studied for biomedical applications, such as in targeted delivery, localized therapy, and as contrast agents for magnetic resonance imaging (MRI).¹⁻³ The water solubility and surface functionality of NPs are key parameters to their interactions with biological systems. The surface coating, in particular, directly affects NP cellular uptake,⁴ biodistribution,⁵ blood circulation,⁶ and metabolism.⁷ Depending on the application, the efficacy of NPs can be directly influenced by the surface coatings. For example, the surface coatings significantly alter the relaxivity of iron oxide NPs as MRI contrast agents.⁸ Currently, high quality iron oxide NPs regarding monodispersity, size distribution, and crystallinity are normally produced in organic solvents at high temperatures.⁹⁻¹³ Therefore, using surface modification to achieve NP water solubility and functionality for further conjugation is essential and remains an outstanding challenge. An ideal method should offer efficient phase transfer, minimal aggregation, great stability, and versatile functional groups for further conjugation.

Typically, the NPs can be transferred from organic solvents to aqueous solutions through attachment of an amphiphilic layer¹⁴⁻¹⁷ or replacement of the hydrophobic coatings by hydrophilic molecules.^{8,18,19} The attachment of an amphiphilic layer via hydrophobic-hydrophobic interactions forms a lipid-bilayer like structure, leading to a full encapsulation of the NP core and its original ligands. The great challenge with this process is the possibility of encapsulation of multiple NPs, causing much increase in the hydrodynamic sizes. Filtration and separation are always performed to get small sized and well dispersed water soluble NPs.¹⁵ Furthermore, this process creates an immediate hydrophobic layer (~ 3 nm) around the NP core, which limits water access and affects the efficacy of iron oxide NPs as MRI contrast agents.²⁰

Alternatively, several ligands have been explored to replace the hydrophobic coatings of iron oxide NPs, such as polyethylene glycol (PEG),²¹ polyethylenimine (PEI),⁸ dendrons,²² and 1,2-diols.^{18,19} These reports provide an important conceptual foundation for our systematic study of the exchange process. To the best of our knowledge, studies have not been performed to investigate the effects of the NP original coatings on the subsequent ligand exchange process. Further, detailed studies on the stability of the NP water dispersions in various biological conditions are needed.

Here, we have systematically investigated parameters affecting the phase transfer process of iron oxide NPs from organic solvent to aqueous solutions. It was discovered that the original coatings of the NPs and the ligand-to-NP ratio were critical to achieve efficient ligand exchange. This process generates well-dispersed water soluble NPs with selective surface functionality (e.g., -COOH, -NH₂, and -SH). These functional groups offer various bio-conjugation possibilities, one of which was demonstrated using thiol-reactive dye molecules. These functionalized NPs showed great stability in Goods buffers, such as 4-(2-hydroxyethyl)-1-piperazineethanesulfonic acid (HEPES) and 2-(N-morpholino)ethanesulfonic acid (MES). However, buffer concentration-dependent aggregation was observed for all three types of NPs in phosphate buffered saline (PBS). This phenomenon was attributed to the formation of salt bridges from the multivalent ions with the charged functional groups on NP surfaces. Interestingly, this aggregation behavior was reversible by removing the multivalent ions. This set of data will provide great practical value for exploring the biological and biomedical applications of iron oxide NPs.

2.2 Experimental Methods

2.2.1 Chemicals

Reagents were purchased from Sigma–Aldrich, otherwise as indicated, including: iron chloride (FeCl_3 , ACROS, 98 %), sodium oleate (TCL, 95 %), oleic acid (OA, Fisher, 95 %), trioctylphosphine oxide (TOPO, 90%), 1-octadecene (90 %), chloroform (99%), polyacrylic acid (PAA) (5 kDa – 50 wt%, partial salt, 15 kDa – 35 wt%, sodium salt, and 100 kDa – 35 wt%), polyethylenimine (PEI) (10 kDa and 60 kDa – 50 wt% aqueous solution), glutathione (GSH, Alfa Aesar, 97 %, reduced), dimethyl sulfoxide (DMSO, VWR, 99 %).

2.2.2 Preparation of the iron–oleate complex

Iron oleate complex was prepared as follows: ferric chloride (6.5 g) was mixed with sodium oleate (36.5 g) in a solvent mixture (hexane, 140 mL and ethanol, 80 mL, and 60 mL de-ionized water) at 65 °C for four hours. After phase separation, the organic phase containing iron oleate complex was washed with de-ionized water and dried inside a chemical hood overnight at room temperature. The entire process was performed in air without inert gas protection, and the obtained brown paste was used as the precursor for iron oxide NP synthesis.

2.2.3 Synthesis of iron oxide NPs

Iron oxide NPs were synthesized by heating the iron oleate complex (2.5 g) in 1-octadecene (10 mL) in the presence of TOPO/OA (TOPO-0.2 g, OA-0.22 mL). The reactants were kept at 100 °C for 1 hour to remove the residual solvents before heating up to 320 °C. After reacting at 320 °C for 2.5 hours, the reaction mixture was cooled down to room temperature. The as-synthesized NPs were precipitated out of solution by centrifugation and then dried under vacuum overnight. The well-dried powder was then re-dispersed into chloroform under sonication to obtain the stock solution of 5 mg / mL for the ligand exchange process.

2.2.4 The ligand exchange process

The ligand exchange process was conducted by mixing the NP stock solution with the exchange ligands in a bipolar solvent, DMSO, at room temperature for 48 hours. Specifically, 1 ml stock solution (5 mg/ mL) was mixed with PAA (5, 15, or 100 kDa), PEI (10 or 60 kDa), or GSH in 50 mL DMSO. The molar ratio of the exchange ligand-to-NP surface Fe atoms was set roughly at 5:1. After 48 hour reaction at room temperature, the iron oxide NPs were magnetically collected and re-dispersed into water (pH = 7) at a concentration of 1 mg / mL. These water-soluble NPs were stable at room temperature for months without notable precipitation.

2.2.5 Stability tests

The pH dependent tests were conducted by carefully adjusting the NP dispersion (pH = 7) to the target values (5 or 9) with HCl or NaOH. The pH-adjusted NP dispersions were then sonicated in water bath for 10 min to ensure the uniformity across the solution. After set at room temperature for another 10 min, the pH value was rechecked to ensure the targeted pH values. When no pH changes of the NP solution, the hydrodynamic size of the NP dispersion was studied with DLS. The stability study in various buffer solutions was started with the preparation of buffer stock solution (100 mM, pH = 7). The stock solution for PBS buffer (10x) was used as purchased. Subsequently, the NP solution was added into the stock solutions to reach three targetted concentration (5, 10, and 50 mM). The well mixed buffer solution was set at room temperture for 10 min and then their hydrodynamic sizes and zeta-potentials were studied.

2.2.6 Characterization of iron oxide NPs

The morphology and size of iron oxide NPs were studied using Hitachi 7860 Transmission electron microscope (TEM). The Fourier transform infrared spectroscopy (FTIR) spectra were collected on a PerkinElmer Spectrum 100 FT-IR spectrometer (Bucks, UK), equipped with an attenuated total reflectance (ATR) cell by accumulation of 4 scans with a

resolution of 2 cm^{-1} . The hydrodynamic size and surface charges of NPs in aqueous solution were evaluated using Zetasizer nano series dynamic light scattering (DLS).

2.3 Results and discussions

This work presents a systematic study of creating stable aqueous dispersion of iron oxide NPs with selective functionality through ligand exchange. The exchange process is illustrated in Figure 2.1, where the original coatings of iron oxide NPs (oleic acid -OA and trioctylphosphine oxide-TOPO) are replaced by three biocompatible molecules: polyacrylic acid (PAA), PEI, or glutathione (GSH). The PAA polymer is a very common electrolyte used for controlling the adsorption behaviors of surfaces; the PEI polymer is a widely used cation polymer for cell adhesion²³ and gene delivery.²⁴ GSH is a tri-peptide with a special peptide linkage between the carboxyl group of the glutamic acid side-chain and the amino group of the cysteine, which is a natural antioxidant in cellular system.²⁵

The original coatings of the NPs played an important role during the ligand exchange process. If NPs were coated with OA ligand only, NP aggregation was always observed and well-dispersed NPs could not be obtained even with filtration. To ensure an effective exchange process, the TOPO ligand was introduced as a co-surfactant during the synthesis. The use of the TOPO ligand has two fundamental importance to the subsequent ligand exchange process. First, TOPO has a weaker binding affinity to iron oxide NP surfaces, as compared to that of the OA ligand.²⁶ Second, the bulky C_8 tails of the TOPO molecule prevent them from forming a densely packed layer on the NP surfaces.²⁷ Both of these effects offer preferred sites for hydrophilic ligands to bind, initiating the ligand exchange process.

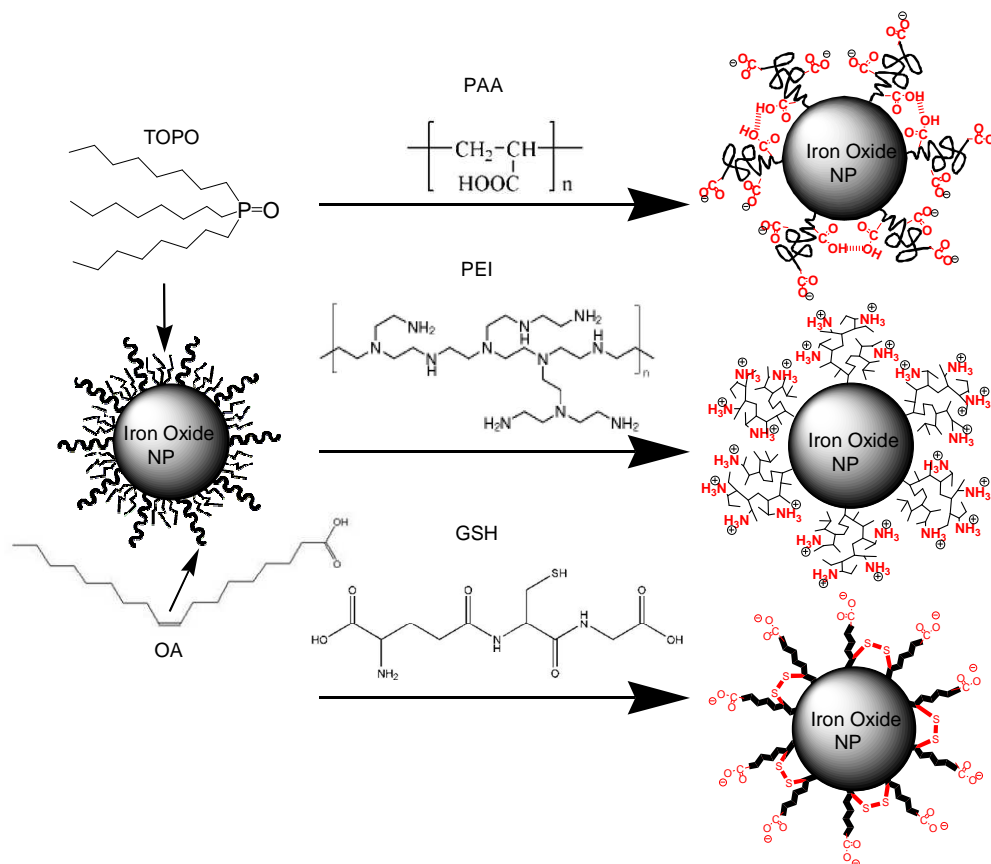


Figure 2.1. Schematic illustration of the ligand exchange process using PAA, PEI or GSH.

The exchange process illustrated in Figure 2.1 assumes that the original coatings of iron oxide NPs are fully replaced by the hydrophilic molecules (e.g., PAA, PEI or GSH). The carboxylic groups of PAA molecules are partially attached on the NP surfaces and the rest of them protrude out from the surface and render the NP solubility. Similarly, PEI molecules interact with iron oxide NPs through portion of the amine groups. These anionic and cationic polymers provide not only surface charges for electrostatic repulsion, but also steric repulsion from the polymer chains. For GSH molecules, the $-NH_2$ groups are believed to interact with the NPs because of the stronger binding affinity of amine groups to iron oxide surfaces compared to that of the carboxylic groups.²⁶ The thiol groups between neighboring molecules form disulfide

bonds, which further stabilize the NPs. A similar mechanism has been proposed to understand the stability of dimercaptosuccinic acid (DMSA) coated iron oxide NPs.¹⁹

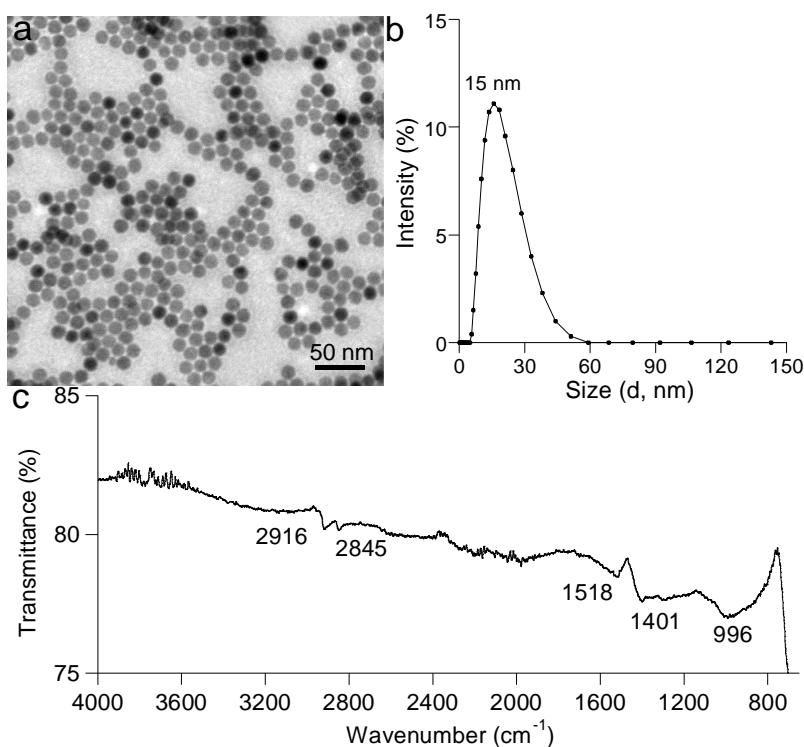


Figure 2.2. The as-synthesized iron oxide NPs coated with OA and TOPO ligands: (a) TEM image, (b) DLS plot, and (c) FTIR spectrum.

Figure 2.2a shows the TEM image of 12 nm monodispersed OA and TOPO coated iron oxide NPs synthesized using our modified heat-up method.²⁸ The hydrodynamic size of these NPs is around 15 nm, which agrees very well with the anticipated size (12 nm inorganic core plus about 3.4 nm shell), as shown in Figure 2b. The narrow dynamic light scattering (DLS) plot also suggests free of aggregation of the NPs in organic solution. The Fourier transform infrared spectroscopy (FTIR) spectrum of the well-dried as-synthesized NPs exhibits the characteristic C-H stretch at 2916 and 2845 cm⁻¹. The broad bands at 1518 and 1401 cm⁻¹ can be assigned to the surface-complexed carboxyl groups of OA molecules.²⁹ The binding of TOPO molecules onto NPs is indicated by the broad band around 996 cm⁻¹ from the -P=O groups.³⁰

To bring the as-synthesized hydrophobic NPs into aqueous solution, a subsequent ligand exchange process was preceded by mixing the NP chloroform solution with the appropriate ligand in dimethyl sulfoxide (DMSO). The relative ratio of the NP-to-ligand was calculated to ensure the ratio of the surface iron atoms to ligands are roughly 1 to 5 (Supporting Information). The use of the dipolar solvent, DMSO, was critical to obtain a homogeneous solution of the hydrophobic NPs and the hydrophilic exchange molecules. After the mixture was reacted in a shaking incubator for 48 h, the NPs were precipitated out of solution by magnetic separation and resuspended in water (pH 7) without any filtration or dialysis separation. The efficacy of the ligand exchange process was monitored by the hydrodynamic sizes and the zeta-potentials of the resultant NPs.

Figure 2.3a-c shows the TEM images of the PAA-, PEI-, and GSH-coated iron oxide NPs in water. Compared with the as-synthesized NPs (Figure 2.2a), the uniformity, morphology, and core size of the NPs did not show evident change. All the NP water dispersions are transparent without any noticeable precipitation (Figure 2.3d-f). The concentration of the water dispersion was roughly estimated to be 1 mg/mL according to the mass concentration of the stock solution. The maximum concentration was obtained by making NP aqueous solution of 5 and 10 mg/mL using PAA-coated NPs as an example. The 5 mg/mL solution remained well dispersed after a week, but the 10 mg/mL solution exhibited notable precipitation after 3 days. Therefore, we consider 10 mg/mL as the highest concentration.

The hydrodynamic sizes of the PAA- and PEI-coated NPs are about 28 and 30 nm, and the GSH-coated NPs are around 23 nm (Figure 2.3g). The relatively larger sizes for PAA- and PEI-coated NPs are due to the long polymer chains and possible formation of hydrogen bonding

between adjacent NPs, as observed in our previous study.³³ The 16 nm size increase for PAA-coated NPs is also consistent with the reported PAA-coated up-conversion fluorescent NPs.³⁴

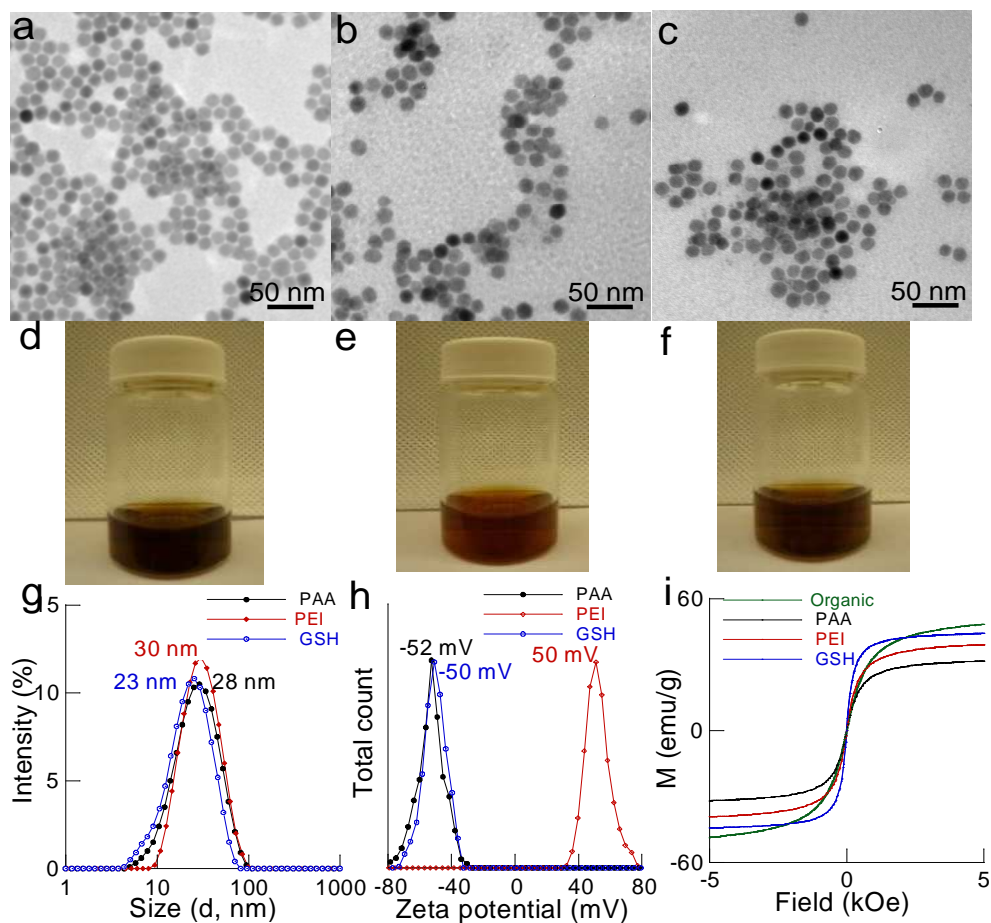


Figure 2.3 Water-soluble NPs coated with PAA, PEI, and GSH: (a-c) TEM images, (d-f) photographs, (g) DLS plots, (h) zeta-potential measurements, and (i) magnetic measurements.

The zeta-potential value of a NP dispersion is an indicator of its stability, where a colloidal system is generally stable if its zeta potential is higher than 30 mV or smaller than -30 mV.³³ The high absolute values of all three NP water dispersions (-52 mV, PAA-coated, +51 mV, PEI-coated, and -50 mV, GSH-coated) indicate their high stability (Figure 2.3h). The negatively charged PAA-coated NPs and the positively charged PEI-coated NPs are due to the ionized $-\text{COO}^-$ and $-\text{NH}_3^+$ groups. The negative zeta-potential of the GSH-coated NPs further

supports our hypothesis that the -NH_2 groups are attached onto the NP surfaces, leaving the carboxylic groups out for water solubility.

Figure 2.3i shows the magnetization (M) versus applied magnetic field (H) curves of iron oxide NPs before and after ligand exchange. All the samples were superparamagnetic without pronounced change except for the decrease in the saturation magnetization. The saturation magnetization of the original NPs was 55 emu/g, where the mass includes the surface coating (about 15%). After ligand exchange, the saturation magnetizations of the NPs decreased to 31 emu/g for PAA-coated NPs, 39 emu/g for PEI-coated NPs, and 45 emu/g for GSH-coated NPs. The decrease in magnetizations was likely due to the increased weight percentage of the organic coatings. For example, the surface coating percentage increased to 36% for PAA-coated NPs based on our iron concentration analysis using inductively coupled plasma mass spectrometry (ICP-MS).

The FTIR spectra of the PAA-, PEI-, and GSH-coated iron oxide NPs further confirmed the success of the ligand exchange process. Compared to the spectrum of pure PAA, the intensive -COOH bands (1704 and 1251 cm^{-1}) disappeared for PAA-coated NPs due to the attachment to NP surfaces and ionization. The attachment of PAA molecules onto iron oxide NP surfaces have been previously reported for NPs synthesized using a polyol method.^{31,34} The new IR band at 1009 cm^{-1} for PAA-coated NPs corresponds to -S=O stretching from the residual DMSO molecules on the NP surface.³⁵ The decreased intensity and shift of the -NH_2 and -NH wagging band from 758 cm^{-1} to 718 cm^{-1} for PEI-coated iron oxide NPs suggests bond formation between the functional groups and NP surfaces. In addition, a shift was also observed for -NH stretch bands (3336 and 3240 cm^{-1}) and -NH bend (1590 cm^{-1}).^{36,37} The band at 1014 cm^{-1} was only observed in PEI-coating NPs, likely from the adsorbed DMSO molecules.

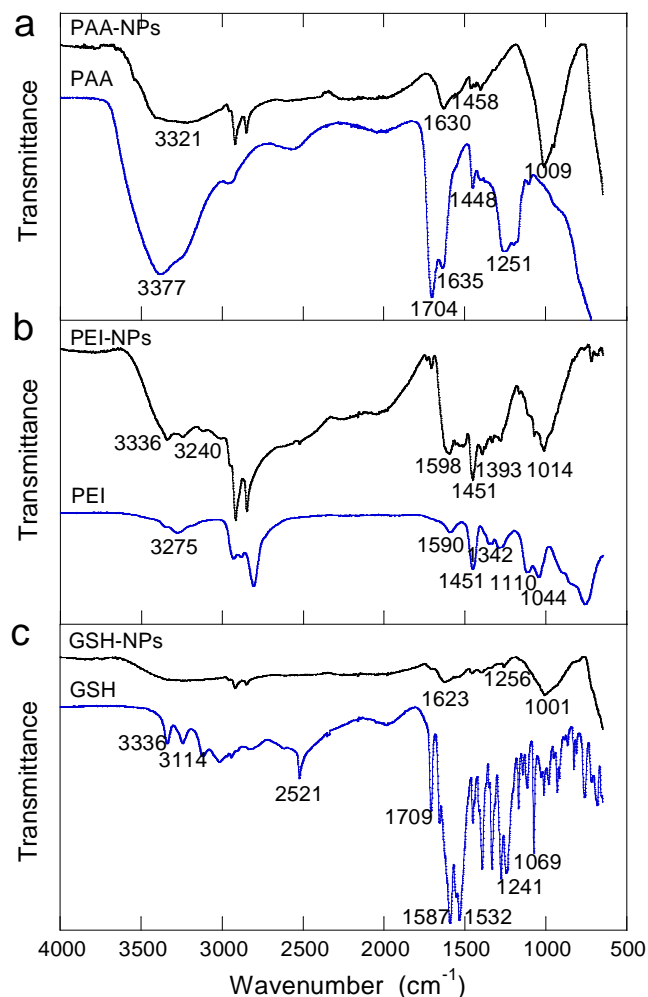


Figure 2.4 FTIR spectra of the ligands and ligand-coated NPs: (a) PAA, (b) PEI, and (c) GSH.

The FTIR spectrum (Figure 2.4c) of pure GSH molecules exhibits many feature peaks from various functional groups, including -NH_2 (3336 , 3114 , 1587 and 1241 cm^{-1}), -SH (2521 cm^{-1}) -COOH (-1709 cm^{-1}), and amides (1532 cm^{-1}). This spectrum agrees very well with the published FTIR spectrum of GSH molecules.³⁸ In contrast, the GSH-coated NPs showed several distinct broad peaks. The faded and broad peak around 3500 cm^{-1} suggests the attachment of -NH_2 groups onto NP surfaces. The interaction between -NH_2 and NPs is further supported by disappearance of the NH_2 scissoring band at 1587 cm^{-1} . The shift of the carboxylic band from 1709 cm^{-1} to 1623 cm^{-1} indicates that the carboxylic groups are either bond to the NP surface or

ionized. Two -COOH groups are present in a GSH molecule, one of which is right next to the -NH₂ group and the other is at the other end of the chain. Therefore, it is highly possible that the one next to the -NH₂ groups binds to the NPs as well. The IR band of -SH group at 2521 cm⁻¹ disappeared for GSH-coated NPs due to the disulfide bond formation. Unfortunately, the IR band of the disulfide bonds (470 cm⁻¹)³⁹ is below the detection limit of our instrument. Along with the zeta-potential study, the FTIR spectrum further confirmed our hypothesis of the -NH₂ groups attached onto NP surfaces. The -S=O stretching (1001 cm⁻¹) of DMSO molecules was also observed for the GSH-coated NPs. To further verify the presence of disulfide bond, a thiol-reactive dye conjugation experiment was performed. After activation of the -SH groups with (tris(2-carboxyethyl)phosphine) (TCEP), the dye molecules were successfully conjugated onto the GSH-coated NPs (Supporting Information). This experiment firmly confirmed the presence of -SH groups on GSH-coated NPs, offering a versatile platform for bio-conjugation.

In addition to the original coatings, the effects of the ligand molecular weight and relative ratios of ligand-to-NP were investigated to understand the exchange condition effects on NP dispersion. Figure 5a shows the DLS plots of iron oxide NPs coated with PAA molecules (5, 15, and 100 kDa). Only several nanometer increase was observed when PAA polymers of higher molecular weights were used, suggesting that the polymers largely twisted on the NP surfaces, rather than stretch out linearly. A similar behavior was observed for PEI-coated NPs when PEI polymers of different molecular weight (10 and 60 kDa) were used (Figure 2.5b). It is important to maintain at least 5 times excess ligands to NP surface Fe atoms to ensure well-dispersed NP dispersions with controlled sized. Figure 2.5c shows the DLS plots of the NP dispersions produced with different PAA-to-NP surface Fe atom ratios. When the ratio was less than 5, a

much increase in particle hydrodynamic sizes (28 to 65 nm) was observed. In contrast, the ratio of 1:15 did not significantly alter the hydrodynamic sizes (28 and 32 nm).

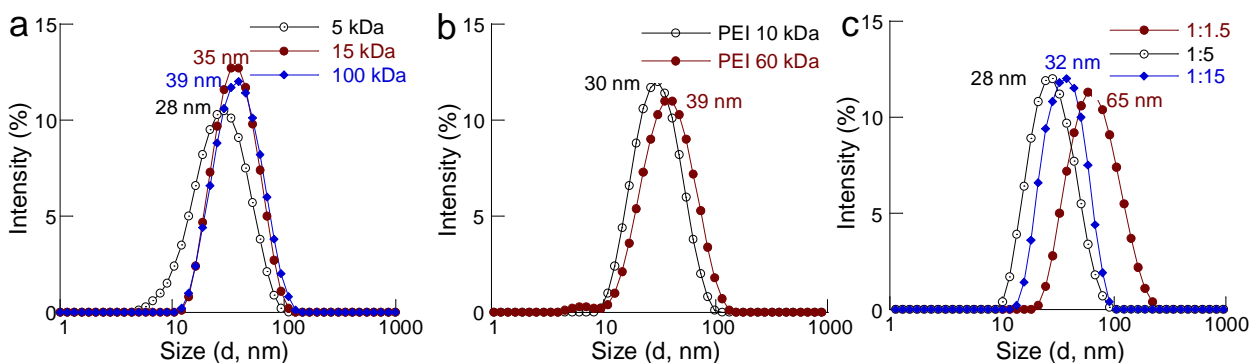


Figure 2.5 DLS plots of iron oxide NPs coated with (a) PAAs of different molecular weights, (b) PEI of different molecular weights, and (c) PAA polymers at different ligand-to-NP ratios.

Beyond the water solubility, several other parameters are critically important for preparing water soluble NPs. The size, size distribution, and surface functionality are considered to be among the keys parameters in determining the interaction of NPs in living systems.^{40, 41} The surface functionality not only directly influences the biological interaction, but also provide means for targeting or recognition conjugation. Biological conjugation processes are generally performed in biological buffers, such as MES buffer for 1-Ethyl-3-[3-dimethylaminopropyl]carbodiimide hydrochloride (EDC) conjugation. The physiochemical properties of NPs in solution are dynamic, and can be altered by the environment. The initially-defined properties, in particular, the hydrodynamic sizes and surfaces, do not necessarily predict their performance during applications. Therefore, it is important to evaluate their dynamic properties in corresponding environments. Here, we studied the size and surface charge alternation in aqueous solution at different pH and in typical biological buffers at pH 7, such as PBS, HEPES, and MES buffers. The emphasis of this study is to understand the stability of NP dispersion towards aggregation under different conditions.

The PAA-, PEI, and GSH-coated NPs are charged because of the presence of ionized COO^- or -NH_3^+ groups. The ionizable property of these groups is dependent on the pH of the NP dispersion. The pH of the as-produced NP dispersions (pH =7) were adjusted to 5 or 9 and their hydrodynamic sizes were subsequently measured to understand their stability (Figure 2.6). The charges on the linear chains of the PAA molecules repel each other, leading to an extended and rigid-rod confirmation. Lowering the pH of the NP dispersion decreases the surface charge density and subsequently the electrostatic repulsion between the NPs. The protonation of the carboxylic groups also increase the propensity to form hydrogen bonds. Therefore, a size increase from 28 to 52 nm was observed when decreasing the pH of the NP dispersion to 5. In contrast, the hydrodynamic size of PAA-coated NPs at pH 9 only increased 2 nm (Figure 2.6a). At higher pH, more positive cation ions were adsorbed to the polymer chains closer to NP surfaces, making the polymer chains more rigid and stretched.⁴²

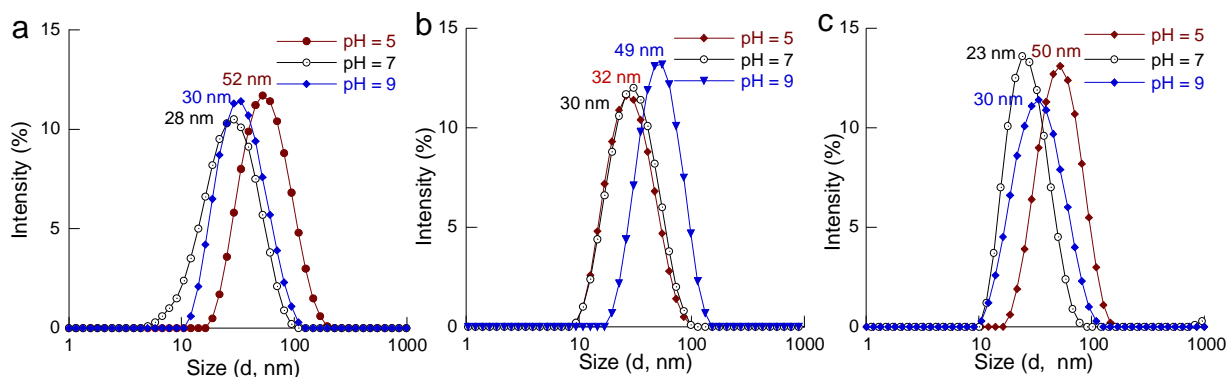


Figure 2.6 DLS plots of NP water dispersions at different pH: (a) PAA-coated, (b) PEI-coated, and (c) GSH-coated.

Similarly, the hydrodynamic sizes of PEI-coated NPs at pH 5 and 7 are close when the -NH_2 groups are protonated, but a noticeable increase in size was observed when the -NH_2 groups in deprotonated condition at higher pH (Figure 2.6b). For GSH-coated NPs, both the zeta potential and FTIR measurements indicated that the amino groups are attached onto the NP

surfaces with $-\text{COO}^-$ groups protruding out from the surfaces. The size alternation of GSH-coated NPs was similar with PAA-coated NPs (Figure 2.6c).

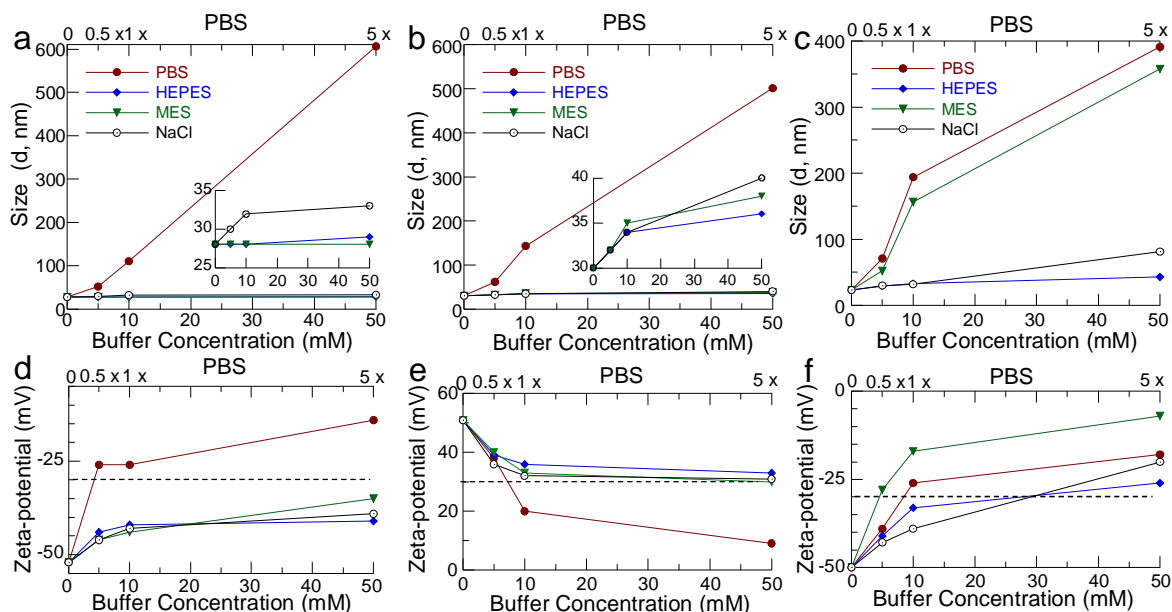


Figure 2.7 NP water dispersions in PBS, HEPES, MES, or NaCl solutions: (a-c) DLS plots of PAA-, PEI-, and GSH-coated NPs, (d-f) zeta-potentials of PAA-, PEI-, and GSH-coated NPs.

The stability of charged NPs in water dispersion is generally affected by the ionic strength of the solution due to ion screening. However, the PAA-coated up-conversion fluorescence NPs were reported to be very stable in PBS buffer.³² We evaluated the stability of PAA-, PEI-, and GSH-coated iron oxide NPs in different buffer solutions by monitoring their hydrodynamic sizes and zeta-potentials (Figure 2.7). Different from the reported PAA-coated up-conversion fluorescence NPs, all three types of the charged NPs showed significant size alternation in PBS, but relatively stable in HEPES, MES, or NaCl solutions except for GSH-coated NPs in MES buffer (Figure 2.7 a-c).

The hydrodynamic sizes (Figure 2.7a) of the PAA-coated NPs increased with the buffer concentration from 28 nm (water) to 52 nm (0.5x PBS), 110 nm (1x PBS), and 606 nm (5x PBS); the hydrodynamic sizes of the PEI-coated NPs changed from 30 nm (water) to 62 nm (0.5x

PBS), 143 nm (1x PBS), and 501 nm (5x PBS); the hydrodynamic sizes of the GSH-coated NPs varied from 23 nm (water) to 71 nm (0.5 x PBS), 194 nm (1x PBS), and 391 nm (5 x PBS). The size increase for PAA- and GSH-coated NPs was believed from the formation of cation salt bridge between two carboxylic groups and a divalent cation, such as Mg^{2+} or Ca^{2+} . These divalent cations are present in the PBS buffer. The effect of divalent cations was further verified by adding $MgCl_2$ solution into the NP dispersion and NPs were precipitated out of solution within 30 second (Supporting Information). The formation of divalent cation salt bridge has been commonly observed with polyelectrolyte molecules.^{43,44} The size increase for PEI-coated NPs in PBS can be explained in a similar way by forming anion bridge between multivalent phosphate group and amino groups.

Compared with NPs in PBS, the PAA-coated NPs are very stable in HEPES and MES buffers, but some level of aggregation was observed with increasing the salt concentration (Figure 2.7a-insert). The PEI-coated NPs showed slightly size increase in HEPES and MES solutions, likely due to the larger negatively charged buffer molecule adsorption on the surface, subsequently decreasing the charge density (Figure 2.7b-insert). Different from PAA- and PEI-coated NPs, GSH-coated NPs showed a significant size increase in MES buffer, but relatively stable in HEPES buffer. The aggregation of GSH-coated NPs in MES is not fully understood at this point, but one possible reason would be partial replacement of GSH by MES molecules via the sulfonate groups. The slight size variation in NaCl solution is mainly from the ion screening.

Consistent with the hydrodynamic sizes, the absolute values of the zeta-potentials of all three types of NPs decrease as sizes increases, suggesting unstable water dispersion and anticipated precipitation of NPs (Figure 2.7d-f). For example, the zeta-potentials of PAA-coated NPs changed from -52 mV (water) to -32 mV (0.5x PBS), -24 mV (1x PBS), and -14 mV (5x

PBS); the zeta-potentials of PEI-coated NPs decreased from 51 mV (water) to 38 mV (0.5x PBS), 20 mV (1x PBS), and 9 mV (5x PBS); the zeta-potentials of GSH-coated NPs varied from -50 mV (water) to -39 mV (0.5x PBS), -26 mV (1x PBS), and -18 mV (5x PBS). The absolute zeta-potentials values of PAA- and PEI coated NPs in HEPES, MES, and NaCl solutions were over 30, indicating their stability. GSH-coated NPs showed zeta-potentials changes in all the conditions, especially at higher buffer or salt concentrations. This stability test reveals new insight into the charged NPs in biological conditions, providing useful information for bioconjugation conditions.

2.4 Conclusions

Water soluble iron oxide NPs with great stability and selective surface functionalities were produced through a ligand exchange process. The original surface coatings and the ligand-to-NP ratio were found to be critical to achieve well-dispersed NP water dispersions. NPs with small hydrodynamic sizes, free of aggregation, and narrow size distribution were obtained without any filtration or post-separation treatments. These water soluble NPs are stable in HEPES, MES buffers, but not stable in PBS buffers with divalent ions. This controllable ligand exchange process will offer significant practical values in exploring the biological and biomedical applications of iron oxide NPs.

Acknowledgement

This work is supported by NSF-DMR 0907204 and in part by an ORAU Junior Faculty Enhancement Award. We acknowledge the UA Central Analytical Facility (CAF) and the Biological Science Department for the use of TEM.

Supporting Information Available

Description of ligand-to-NP ratio calculation, thiol-reactive dye conjugation, and salt bridge formation experiment. This materials is available free of charge via the Internet at <http://pubs.acs.org>.

2.5 References

1. Pankhurst, Q. A.; Connolly, J.; Jones, S. K.; Dobson, J., *J. Phys. D: Appl. Phys.* **2003**, *36*, R167-R181.
2. Laurent, S.; Forge, D.; Port, M.; Roch, A.; Robic, C.; Elst, L. V.; Muller, R. N. *Chem. Rev.* **2010**, *110*, 2574-2574.
3. Fang, C.; Zhang, M. *J. Mater. Chem.* **2009**, *19*, 6258-6266.
4. Clift, M. J. D.; Rothen-Rutishauser, B.; Brown, D. M.; Duffin, R.; Donaldson, K.; Proudfoot, L.; Guy, K.; Stone, V. *Toxicol. Appl. Pharmacol.* **2008**, *232*, 418-427.
5. Chouly, C.; Pouliquen, D.; Lucet, I.; Jeune, J. J.; Jallet, P. *J. Microencapsulation* **1996**, *13*, 245-255.
6. Moghimi, S. M.; Hunter, A. C.; Murray, J. C. *Pharmacol. Rev.* **2001**, *53*, 283-318.
7. Lunov, O.; Syrovets, T.; Rucker, C.; Tron, K.; Nienhaus, G. U.; Rasche, V.; Mailander, V.; Landfester, K.; Simmet, T. *Biomaterials* **2010**, *31*, 9015-9022
8. Duan, H.; Kuang, M.; Wang, X.; Wang, Y.; Mao, H.; Nie, S. *J. Phys. Chem. C* **2008**, *112*, 8127-8131.
9. Rockenberger, J.; Scher, E. C.; Alivisatos, A. P. *J. Am. Chem. Soc.* **1999**, *121*, 11595-11596.
10. Hyeon, T.; Lee, S. S.; Park, J.; Chung, Y.; Bin Na, H. *J. Am. Chem. Soc.* **2001**, *123*, 12798-12801.
11. Xie, J.; Peng, S.; Brower, N.; Pourmand, N.; Wang, S.; Sun, S., *Pure Appl. Chem.* **2006**, *78*, 1003-1014.
12. Park, J.; An, K. J.; Hwang, Y. S.; Park, J. G.; Noh, H. J.; Kim, J. Y.; Park, J. H.; Hwang, N. M.; Hyeon, T. *Nat. Mater.* **2004**, *3*, 891-895.
13. Yu, W. W.; Falkner, J. C.; Yavuz, C. T.; Colvin, V. L. *Chem. Commun.* **2004**, 2306-2307.
14. Gonzales, M.; Krishnan, K. M., *J. Magn. Magn. Mater.* **2007**, *311*, 59-62.
15. Prakash, A.; Zhu, H. G.; Jones, C. J.; Benoit, D. N.; Ellsworth, A. Z.; Bryant, E. L.; Colvin, V. L. *ACS Nano* **2009**, *3*, 2139-2146.
16. Yu, W. W.; Chang, E.; Sayes, C. M.; Drezek, R.; Colvin, V. L., *Nanotechnology* **2006**, *17*, 4483-4487.
17. Shen, L.; Laibinis, P. E.; Hatton, T. A. *J. Magn. Magn. Mater.* **1999**, *194*, 37-44.
18. Binder, W. H.; Weinstabl, H.; Sachsenhofer, R. *J. Nanomater.* **2008**, 383020, 1-10.
19. Fauconnier, N.; Pons, J. N.; Roger, J.; Bee, A. *J. Colloid Interface Sci.* **1997**, *194*, 427-433.

20. Tromsdorf, U. I.; Bigall, N. C.; Kaul, M. G.; Bruns, O. T.; Nikolic, M. S.; Mollwitz, B.; Sperling, R. A.; Reimer, R.; Hohenberg, H.; Parak, W. J.; Forster, S.; Beisiegel, U.; Adam, G.; Weller, H., *Nano Lett.* **2007**, *7*, 2422-2427.
21. Herve, K.; Douziech-Eyrolles, L.; Munnier, E.; Cohen-Jonathan, S.; Souce, M.; Marchais, H.; Limelette, P.; Warmont, F.; Saboungi, M. L.; Dubois, P.; Chourpa, I. *Nanotechnology* **2008**, *19*, 465608(1-7).
22. Hofmann, A.; Thierbach, S.; Semisch, A.; Hartwig, A.; Taupitz, M.; Ruhl, E.; Graf, C. *J. Mater. Chem.* **2010**, *20*, 7842-7853.
23. Lakard, S.; Herlem, G.; Propper, A.; Kastner, A.; Michel, G.; Valles-Villarreal, N.; Gharbi, T.; Fahys, B. *Bioelectrochem.* **2004**, *62*, 19-27.
24. Xia, T.; Kovoichich, M.; Liang, M.; Meng, H.; Kabehie, S.; George, S.; Zink, J. I.; Nel, A. E. *ACS Nano* **2009**, *3*, 3273-3286.
25. Pompella, A.; Visvikis, A.; Paolicchi, A.; De Tata, V.; Casini, A. F. *Biochem. Pharmacol.* **2003**, *66*, 1499-1503.
26. Palchoudhury, S.; Xu, Y.; An, W.; Turner, C. H.; Bao, Y. *J. Appl. Phys.* **2010**, *107*, 09B311(1-3).
27. Bao, Y.; Beerman, M.; Pakhomov, A. B.; Krishnan, K. M. *J. Phys. Chem. B* **2005**, *109*, 7220-7222.
28. Palchoudhury, S.; Xu, Y.; Goodwin, J.; Bao, Y., *J. Mater. Chem.* **2011**, *21*, 3966-3970.
29. Fang, C.; Bhattarai, N.; Sun, C.; Zhang, M., *Small* **2009**, *5*, 1637-1641.
30. Young, A. G.; Al-Salim, N.; Green, D. P.; McQuillan, A. J., *Langmuir* **2008**, *24*, 3841-3849.
31. Keshavarz, S.; Xu, Y.; Hrdy, S.; Lemley, C.; Mewes, T.; Bao, Y. *IEEE Trans. Magn.* **2010**, *46*, 1541-1543.
32. Yi, G. S.; Chow, G. M. *Chem. Mater.* **2007**, *19*, 341-343.
33. Taboada, E.; Rodriguez, E.; Roig, A.; Oro, J.; Roch, A.; Muller, R. N. *Langmuir* **2007**, *23*, 4583-4588.
34. Ge, J.; Hu, Y.; Biasini, M.; Dong, C.; Guo, J.; Beyermann, W. P.; Yin, Y. *Chem.-Eur. J.* **2007**, *13*, 7153-7161.
35. Fawcett, W. R.; Kloss, A. A. *J. Phys. Chem.* **1996**, *100*, 2019-2024..
36. Ba, C.; Langer, J.; Economy, J. *J. Membr. Sci.* **2009**, *327*, 49-58.
37. Herlem, G.; Gharbi, T.; Ben Sedrine, N. *J. Mol. Struct.-Theochem.* **2010**, *945*, 27-32.
38. Shayani-Jam, H.; Nematollahi, D. *Chem. Commun.* **2010**, *46*, 409-411.
39. Dimitrova, M.; Turmanova, S.; Vassilev, K. *React. Kinet. Mech. Catal.* **2010**, *99*, 69-78.

40. Oh, W. K.; Kim, S.; Choi, M.; Kim, C.; Jeong, Y. S.; Cho, B. R.; Hahn, J. S.; Jang, J. *ACS Nano* **2010**, *4*, 5301-5313.
41. Zhang, S.; Li, J.; Lykotrafitis, G.; Bao, G.; Suresh, S. *Adv. Mater.* **2009**, *21*, 419-424.
42. Aulich, D.; Hoy, O.; Luzinov, I.; Brucher, M.; Hergenroder, R.; Bittrich, E.; Eichhorn, K. J.; Uhlmann, P.; Stamm, M.; Esser, N.; Hinrichs, K. *Langmuir* **2010**, *26*, 12926-12932.
43. Huang, R. Y. M.; Gao, C.; Kim, J. J. *J. Appl. Polym. Sci.* **1983**, *28*, 3063-3073.
44. Liu, S.; Ghosh, K.; Muthukumar, M. *J. Chem. Phys.* **2003**, *119*, 1813-1823.

2.6 Supporting informations

2.6.1. Calculation of the required amount of ligands for the exchange process

The molar ratio between hydrophilic molecules and Fe atoms on NP surface was set at 5 to 1, where the amount of Fe atoms on a NP surface was roughly estimated as follows. NPs in 1 mL stock solution (5 mg/mL) was precipitated out and dried under vacuum. The rough mass (5 mg) was then divided by the mass of a single NP [$m=(1/6)\pi d^3\rho$], where ρ is the bulk density of iron oxide (5.24 g/cm³), the d is the measured NP diameter from a transmission electron microscopy (TEM) image. The resultant NP numbers was then divided by the Avogadro constant ($N_A = 6.023\times 10^{23}$), yielding the molar amount of NPs. The number of surface Fe atoms was estimated using the volume of one NP divided by the volume of a cubic unit cell (cell parameter = 8.5 Å). Then, 18% of the unit cells were assumed to locate on the NP surfaces and one Fe atom from each surface unit cell was on the NP surface. The molar amount of the ligands was set 5 times more than the surface Fe atom.

2.6.2. Fluorescent dye conjugation of GSH-coated NPs

To verify the existence of disulfide bonds on GSH-coated NP surfaces, a conjugation experiment was performed using thiol-reactive red fluorescent dye (Texas Red C2- maleimide, Invitrogen). Specifically, a 10-fold molar excess of (tris(2- carboxyethyl)phosphine) (TCEP) was added to the GSH-coated NP solution to activate the thiol groups. The dye molecules were then introduced to the solution and the reaction was preceded for two hour under room temperature. Finally, the dye-conjugated NPs were magnetically separated from the solution and re-dispersed into water. Figure S2.1 shows the emission and excitation scans of the dye-conjugated NPs in water after magnetic separation.

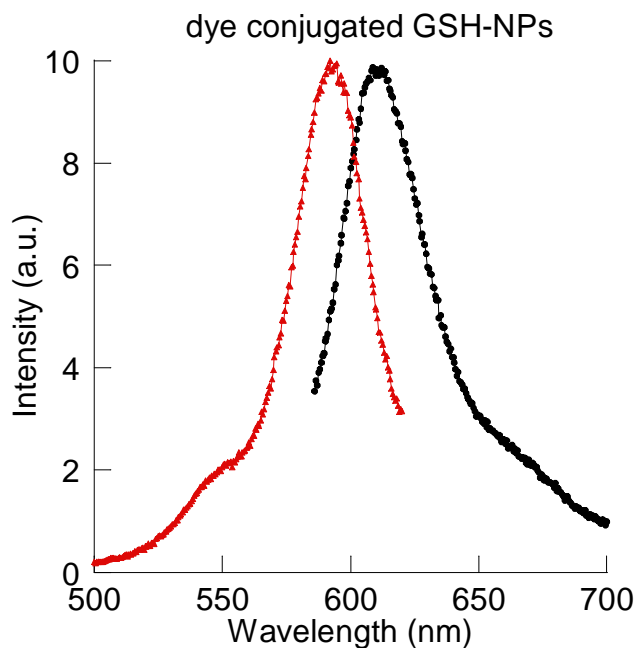


Figure S2.1 The emission (black) and excitation (red) scans of the dye-conjugated GSH-coated NPs after magnetic separation.

2.6.3. Effect of the divalent cation on the stability of charged NPs

Using GSH-coated NPs as an example, we studied the effects of divalent cations on the stability of the NP dispersion. Specifically, MgCl_2 water solution (5 mM) was mixed with the NP solution (Figure S2.2a). The NPs were precipitated out of solution within 30 second, yielding a clear, colorless solution (Figure S2.2b). Interestingly, the precipitated NPs can be redispersed into water again after repeated magnetic separation and washing three times.

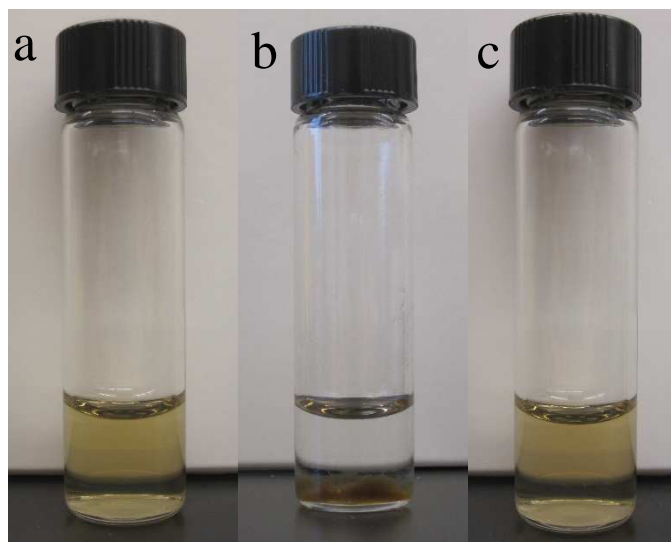


Figure S2.2 Photographs of GSH- coated NP dispersions: (a) original solution, (b) after addition of Mg^{2+} , and (c) Mg^{2+} removed from solution.

CHAPTER 3

MAKE CONJUGATION SIMPLE: A FACILE APPROACH TO INTEGRATED NANOSTRUCTURES

(Published in *Langmuir* **2012**, 28, 8767-8772)

Yaolin Xu, Soubantika Palchoudhury, Ying Qin, Thomas Macher, and Yuping Bao*

ABSTRACT

We report a facile approach to the conjugation of protein-encapsulated gold fluorescent nanoclusters to the iron oxide nanoparticles through catechol reaction. This method eliminates the use of chemical linkers and can be readily extended to the conjugation of biological molecules and other nanomaterials onto nanoparticle surfaces. The key to the success was producing water soluble iron oxide nanoparticle with active catechol groups. Further, advanced electron microscopy analysis of the integrated gold nanoclusters and iron oxide nanoparticles provided direct evidence of the presence of a single fluorescent nanocluster per protein template. Interestingly, the integrated nanoparticles exhibited enhanced fluorescent emission in biological media. These studies will provide significantly practical value in chemical conjugation, the development of multifunctional nanostructures, and exploration of multifunctional nanoparticles for biological applications.

KEYWORDS

Multifunctional nanoparticles · imaging probes · conjugation · integrated nanostructures

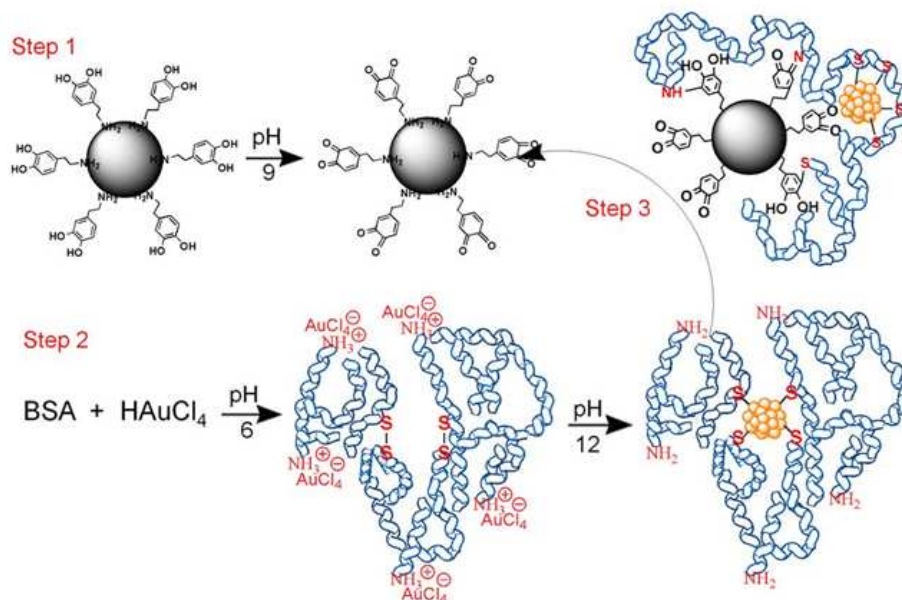
3.1 Introduction

Recent interest in nanomaterial fabrication has gone beyond the production of a single material. Integration of multiple nanocomponents provides the capability of performing multi-tasks on a single platform.¹⁻³ Among various multifunctional nanostructures, magnetic-fluorescent nanoparticles have drawn much attention because of the clinically-proven *in vivo* imaging capability of iron oxide nanoparticles⁴ and the high sensitivity of *in vitro* fluorescent imaging.^{5, 6} Iron oxide nanoparticles have been clinically used as negative (T_2) contrast agents for magnetic resonance imaging, a complementary contrast agent to the positive (T_1) gadolinium complex contrast agent. Apart from being contrast agents, iron oxide nanoparticles have great potential in cancer therapy and nanoparticle imaging.⁷ Therefore, iron oxide (magnetite or maghemite) has been the natural choice as the magnetic component. In contrast, the fluorescent component can be chosen from organic dyes, fluorescent proteins, or quantum dots. Extensive effort has been made to integrate magnetic and fluorescent nanocomponents, aiming to create a “two-in-one” platform.^{8, 9} The integration strategies of these two components generally fall into the following categories: (1) magnetic nanoparticles and the fluorescent components (organic dyes or quantum dots) are encapsulated inside a shell (micelles,¹⁰ silica,¹¹ liposomes,¹² or polymers¹³). (2) magnetic nanoparticles are coated with a porous silica shell containing fluorescent dyes or inorganic ion complexes.^{14, 15} (3) magnetic nanoparticles are directly conjugated to the fluorescent components.¹⁶ (4) magnetic nanoparticles and quantum dots form contact core-shell structures,^{17, 18} or heterodimers.¹⁹ Common challenges of all these modalities include complexity of the synthetic procedures, significant size increases, and interparty influences between the fluorescent and magnetic components. Here, a new type of magnetic-fluorescent nanoparticles using gold (Au) nanoclusters as the fluorescent component is reported,

which overcomes most of the existing challenges, such as issues related to size increase, potential toxicity, synthetic complexity, and water solubility.

Au fluorescent nanoclusters represent a new class of fluorescent tags, which have several advantages over others,²⁰ such as aqueous synthesis, low potential *in vivo* toxicity, tumor imaging capability, and minimal effects on the biological function of the labeled bioentities.²¹ The integration of fluorescent nanoclusters and iron oxide nanoparticles will not only lead to a new type of bifunctional nanoparticles, but also open up a number of opportunities in simultaneous imaging and therapy.

We report a facile approach to the integration of magnetic iron oxide nanoparticles and fluorescent Au nanoclusters. This process utilizes the catechol reaction between the active surface of dopamine-coated iron oxide nanoparticles and the bovine serum albumin (BSA)-encapsulated Au nanoclusters. The use of the activated dopamine surface for direct conjugation is the major innovative design of this paper, which eliminates the use of chemical linkers and specialized conditions for chemical conjugation. Importantly, this conjugation can be generalized for attaching biological molecules and other nanostructures to the iron oxide nanoparticle surfaces. Another important finding of this work is the observation of the presence of a single nanocluster per BSA protein molecule by advanced electron microscopy. These integrated nanostructures are highly stable in biological environments in terms of structural integrity and optical property. In the process of preparing this manuscript, a study of the conjugation of Au nanoclusters onto iron oxide nanoparticle surfaces through 1-Ethyl-3-(3-dimethylaminopropyl)carbodiimide (EDC cross-linker) was reported.²²



Scheme 3.1 Schematic illustration of the facile approach to magnetic-fluorescent bifunctional nanoparticles.

An overview of this facile approach with three consecutive steps is shown in scheme 3.1:

(1) preparation of iron oxide nanoparticles with an active surface, (2) synthesis of BSA-encapsulated Au nanoclusters, and (3) integration of iron oxide nanoparticles and Au nanoclusters through catechol reaction.

3.2 Experimental methods

3.2.1 Dopamine attachment onto iron oxide nanoparticles

Iron oxide nanoparticles were synthesized using a modified heat-up method,²³⁻²⁵ where a weak binding ligand, trioctylphosphine oxide, was added during synthesis. The iron oleate complex (2.5 g, 2.8 mmol) was heated up to 320 °C in 1-octadecene (10 mL, 90%) in the presence of TOPO (90%)/OA(97%) (TOPO-0.2 g, 0.5 mmol, OA-0.22 mL, 0.7 mmol). After 2.5 hours, the reaction mixture was cooled down to room temperature and the as-synthesized nanoparticles were precipitated out of solution by centrifugation and then dried under vacuum overnight. The well-dried powder was then re-dispersed into chloroform under sonication to

obtain the stock solution of 5 mg/ mL. This modification allows for complete ligand exchange by other hydrophilic molecules, as previously demonstrated.²³ In brief, 1 mL of iron oxide chloroform solution (5 mg/mL) was mixed with dopamine·HCl (1.7 mg) in 49 mL of dimethyl sulfate oxide (DMSO). After 48 h mixing at room temperature, the iron oxide nanoparticles were collected by centrifugation and re-dispersed in water (1 mg/mL).

3.2.2 Surface activation of dopamine-coated iron oxide nanoparticles

The pH of nanoparticle solution was adjusted to 9 with NaOH (1M) to activate the dopamine coatings. The nanoparticle solution was then sonicated for 10 min to accelerate the activation process and kept at room temperature. After 4 h activation, these nanoparticles were used for the conjugation with the fluorescent Au nanoclusters.

3.2.3 Preparation of fluorescent gold nanoclusters

The fluorescent gold nanoclusters were synthesized using a similar method reported by Ying,²⁶ but with a higher Au to BSA ratio. Specifically, BSA powder (50 mg) was first dissolved in water (1 mL, 18.2 Ω), followed by the addition of cold HAuCl₄ solution (0.2 wt%, 3.4 mL). The reaction mixture was reacted at room temperature for an hour, allowing for the complexation between BSA and Au ions. Finally, NaOH (0.5 mL, 1M) was added into this mixture to trigger the reduction of Au ions and subsequent formation of Au nanoclusters. After 4 h reaction at 45 °C, the yellowish Au nanocluster solution was collected for characterization and conjugation.

3.2.4 Integration of activated iron oxide nanoparticles with fluorescent gold nanoclusters

To obtain the integrated nanoparticles, activated dopamine-coated nanoparticle solution (0.5 mL, 1 mg/mL) was simply mixed with the as-synthesized BSA-Au nanocluster solution (4.9 mL). After 12 h reaction at room temperature, the conjugated nanoparticles were magnetically separated out of the solution and re-dispersed in water for further characterization and stability

studies. The magnetic separation was performed by placing a permanent magnet next to the sample vial for half an hour and then the solution was removed with disposal pipettes. To ensure the removal of free nanoclusters, this process was repeated twice.

3.2.5 Characterization

The morphology and size of iron oxide nanoparticles were examined under bright field TEM and the gold nanocluster attachment was confirmed with HAADF imaging (FEI Tecnai, F-20, 200 kV). The surface chemistry of the nanoparticles was studied by FTIR spectroscopy. The hydrodynamic sizes and the surface charges of the nanoparticles in aqueous solution were measured using a Zetasizer nano series dynamic light scattering (DLS). The fluorescence of BSA-encapsulated Au nanoclusters and conjugated nanoparticles were studied using a Cary Eclipse fluorescence spectrophotometer. The UV-vis spectra were collected on a Shimadzu UV-visible spectrophotometer (UV-1700 series). The magnetic moment versus applied magnetic field (M-H) curves were measured using an alternating gradient magnetometer (AGM). The quantum yields of the BSA-Au nanoclusters and the integrated nanoparticles were calculated by comparing the wavelength-integrated fluorescence intensities of the samples to that of a Texas red dye with known quantum yield of 66% from molecular probe.

3.3 Results and discussion

The first step to the fluorescent-magnetic bifunctional nanoparticles is the formation of an active surface on the iron oxide nanoparticles. Iron oxide (maghemite) nanoparticles were synthesized *via* a modified heat-up method in organic solvent.^{23-25,27} The introduction of a weak capping molecule, trioctylphosphine oxide, during synthesis is critical for the attachment of hydrophilic ligands after synthesis.²⁴ Dopamine, a catechol amine molecule, was used as the capping ligand of the iron oxide nanoparticles for subsequent surface activation. Here, we

believe that the amino group of dopamine interacts with the iron oxide nanoparticle, leaving the catechol group protruding out for further conjugation. The amino group attachment is primarily applicable to the iron oxide nanoparticles produced in organic solvent. In contrast, iron oxide nanoparticles synthesized *via* the co-precipitation method at high pH will interact with the catechol groups through the surface hydroxyl groups, leaving the amino groups out.^{22, 28} The availability of the catechol groups on the nanoparticle surfaces is critically important to the direct conjugation of biological molecules.

Figure 3.1a shows the transmission electron microscopy (TEM) image of the well-dispersed dopamine-coated, 10 nm iron oxide nanoparticles in water. The interaction between dopamine and the iron oxide nanoparticle was studied using Fourier transform infrared spectroscopy (FTIR) (Figure 3.1b). Compared to that of the free dopamine, the FTIR spectrum of dopamine-coated nanoparticles showed several band shifts related to the primary amine group. The two -NH_2 stretching peaks of the free dopamine in the range of $3200\text{-}3400\text{ cm}^{-1}$ became a single broad peak at 3327 cm^{-1} after interacting with iron oxide nanoparticles. This broad peak is likely merged with the hydroxyl stretching in the similar region. After interacting with iron oxide nanoparticles, the dopamine -NH_2 bending (1577 and 1469 cm^{-1}) merged together with the -C=C- stretching in the range of $1460\text{-}1617\text{ cm}^{-1}$ and a much broader peak was observed. Further, the band of the -NH_2 wagging (815 cm^{-1})²⁹ shifted to a lower wavelength, another indicator of the attachment of amino groups to the nanoparticle surfaces.

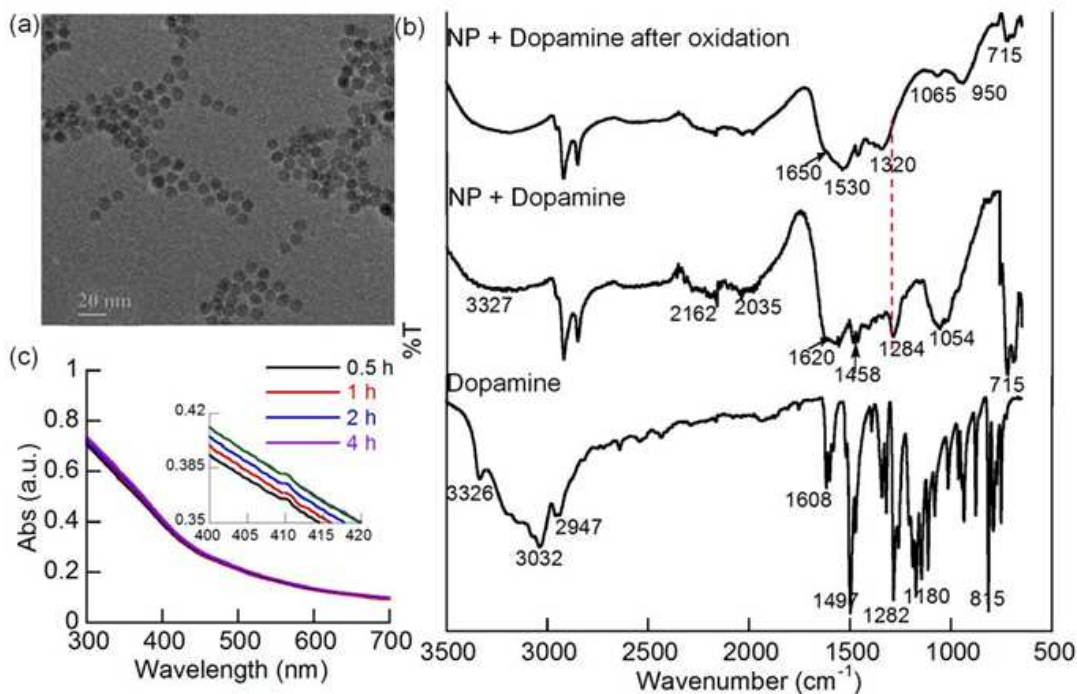


Figure 3.1 (a) TEM image of the dopamine-coated iron oxide nanoparticles (10 nm), (b) FTIR spectra of free dopamine, dopamine-coated, and activated dopamine-coated nanoparticles, and (c) time-dependent UV-vis spectra of dopamine-coated iron oxide nanoparticles after activation.

This observation was consistent with our previous studies that the amino group has a preferable binding to iron oxide nanoparticles over other functional groups.^{24,27} The presence of the catechol groups on the nanoparticle surface was also supported by the negative zeta-potential (-42 mV) of the dopamine-coated nanoparticles. Otherwise, the amino groups on the nanoparticle surfaces will lead to a positive zeta-potential. The characteristic band of the -C-O stretching (1282 cm^{-1}) was unchanged before and after the attachment. The catechol groups on the nanoparticle surfaces can be easily oxidized into dopamine-quinone at higher pH (> 9), creating an active surface for further conjugation.

The surface activation was achieved by simply adjusting the pH of the nanoparticle solution to 9. The IR spectrum of the activated nanoparticle surface was shown in Figure 3.1b. The appearance of the broad band at 1650 cm^{-1} is the characteristic of -C=O band in quinone

structure.³⁰ The disappearance of the characteristic band of -C-O at 1282 cm^{-1} is another indicator of the dopamine oxidation. The oxidation process was also monitored with UV-vis spectroscopy (Figure 3.1c). Because of the strong absorption of iron oxide nanoparticles, the absorption of the oxidized dopamine molecules was not well resolved. However, the typical absorption peak (409 nm) of the oxidized dopamine was clearly visible in the detailed scan (Figure 3.1c-insert). This absorption matched well with the oxidized free dopamine (Figure S3.1). Both the FTIR and the UV-vis spectra confirmed the dopamine oxidation on the iron oxide nanoparticle surfaces. The activated dopamine groups will allow for the direct conjugation of biological molecules through Michael addition and/or Schiff base formation.^{31, 32}

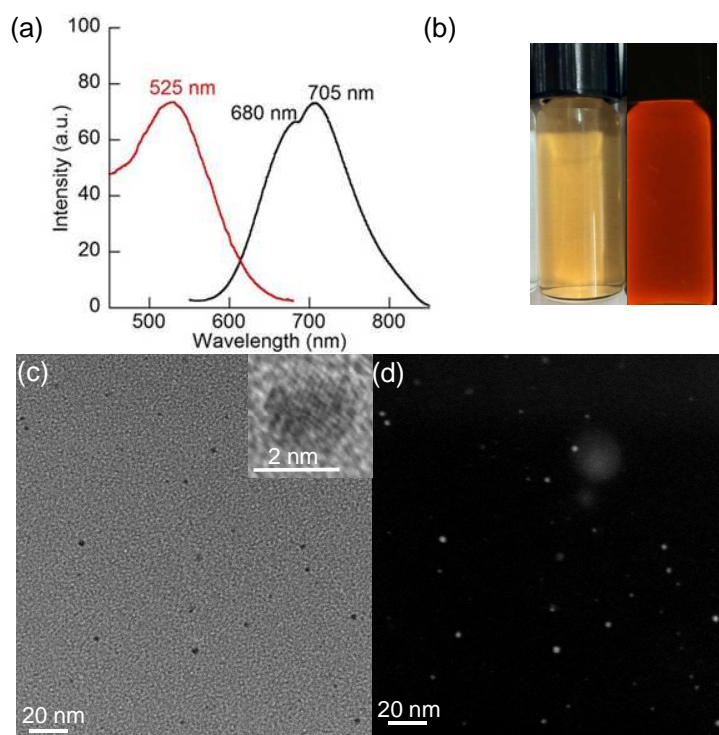


Figure 3.2 BSA-encapsulated Au nanoclusters: (a) fluorescent emission excited at 520 nm and excitation scan for emission peak of 680 nm plots, (b) photographs of nanocluster solution under room (left) and UV light (right), (c) bright field TEM image, and (d) HAADF TEM image.

The fluorescent Au nanoclusters were produced using BSA as a template and reducing agent, following a similar method reported by Ying.²⁶ Here, a higher Au to BSA ratio (26:1) was

used to minimize the presence of free BSA proteins, because the free BSA will affect the conjugation efficiency. Figure 3.2a shows the fluorescent emission and excitation plots of the Au nanoclusters. The broad emission peaks at 680 and 705 nm are likely due to the inhomogeneous size of the Au nanoclusters. The yellowish solution of the BSA-encapsulated Au nanoclusters showed intense red emission under UV-radiation (365 nm) (Figure 3.2b). The TEM image of these nanoclusters also indicated the polydispersity of the nanoclusters (Figure 3.2c). The high resolution (HRTEM) of a typical 2 nm BSA-Au nanocluster indicated the crystalline nature of these nanoclusters (Figure 3.2c-insert). Direct observation of these small nanoclusters (< 2 nm) under bright field TEM is highly challenging. Therefore, high-angle annular dark-field (HAADF) imaging was applied because of its sensitivity to heavier elements (Figure 3.2d), where Au nanoclusters became clearly visible.

The formation mechanism of Au nanoclusters was believed to involve the initial complexation of protein-Au ions and subsequent reduction of Au ions by tyrosine residues at a higher pH. However, the role of specific amino acids remains unresolved. We hypothesize that the AuCl_4^- ions initially interact with the amino groups (*e.g.*, lysine and arginine) of the BSA through electrostatic interactions. Even though the Au-thiol group (-SH) interaction is much stronger, the disulfide bonds are hidden within the secondary structure of the protein and inaccessible in the pH range of 5-7.³³ These disulfide bonds will gradually become available at higher pH. With increasing the pH, the Au(III) complexes were quickly reduced into Au(I) complexes until further reduction by tyrosine. The reduction from Au(III) to Au(I) can be monitored by UV-vis spectroscopy. The HAuCl_4 solution (pH 2) has a strong absorption at 217 nm and a shoulder at 287 nm due to the ligand-to-metal charge transfer between Au(III) and Cl^- .³⁴ The reduction from Au(III) to Au(I) complexes were mainly due to the pH increase of the

reaction solution, where the pH of the HAuCl_4 reagent solution was 2 and the BSA solution was adjusted to 6. The pH effect was verified by measuring the absorption of the diluted HAuCl_4 solution in water (pH 6), where the absorption of Au(III) at 287 nm disappeared and the strong absorption at 217 nm shifted to lower wavelength (Figure S3.2a). The possibility of the ligand replacement effect during pH increase (e.g. Cl^- to OH^-) was studied by adding NaCl into the solution to ensure the presence of Au chloride complexes. Similar shifts in the absorption spectra were observed (Figure S3.2b). Therefore, we believe that the spectrum shift is related to the reduction of Au(III) to Au(I). This spectrum shift was used to study the interaction between specific amino acids and HAuCl_4 .

To study the role of the specific amino acids within BSA, lysine (1.71 mg), arginine (3.32 mg), and histidine (0.94 mg) water solutions (pH 6) were prepared, where the amounts of amino acids were set to be equivalent to the amino acid amounts in 25 mg of BSA. After mixing with 1.7 mL HAuCl_4 solution, the absorption spectra were collected (Figure S3.3). Similar to BSA, lysine- and arginine- Au mixtures exhibited shifts in the 217 nm band and a much broader 287 nm shoulder. The broadened band centered around 290 nm is a characteristic of ion-pair formation between ligands and Au ions.³⁵ The complexed solution of lysine-Au and arginine-Au remained clear, similar to that of BSA-Au solution. In contrast, the solution mixture of histidine and HAuCl_4 turned dark red, an indicator of the Au nanoparticle formation. Based on these observations, we suggested that the complexation between BSA and AuCl_4^- ions was likely involved lysine and arginine, but not histidine residues. Further pH increase to 12 triggered the reduction of the Au(I) complexes to Au atoms by tyrosine and subsequent nanocluster formation. Importantly, at this pH, the disulfide bonds are accessible to Au nanoclusters, allowing for the formation of stable S-Au-S motif capped Au nanoclusters in the protein template. The presence

of Au(I) within the Au nanoclusters have been reported by various groups.^{26, 36} The as-synthesized BSA-Au nanocluster solution was yellowish color and stable at room temperature for months.

To obtain the magnetic-fluorescent integrated nanostructure, the iron oxide nanoparticles with activated dopamine surfaces were simply mixed with the as-synthesized BSA-Au nanoclusters and incubated at room temperature for 12 h. The conjugated nanoparticles were then magnetically separated out of the solution and re-dispersed in water. This integration process utilized the facile interaction between the activated catechol groups and the amino or thiol groups of the BSA protein. The significance of this conjugation is the elimination of additional chemical linkers and specifically required conjugation conditions.

Figure 3.3a shows the fluorescent emission and excitation plots of the integrated nanoparticles after the removal of the free BSA-Au nanoclusters by two magnetic separations. Compared to the two emission peaks (680 and 705 nm, Figure 3.2a) of the unconjugated nanoclusters, only one emission peak at 680 nm was observed. The two emission peaks were likely resulted from the dynamic conformation of BSA. After immobilized on the nanoparticle surfaces, the dynamic conformation of BSA was significantly reduced. The integrated nanoclusters on the nanoparticle surfaces were not as bright as the unconjugated Au nanoclusters (Figure 3.3b); however, the intensive red emission of the integrated nanostructure could be clearly seen. The fluorescent emission intensity reduction was mainly due to the much lower nanocluster concentration than the free BSA-Au nanocluster solution.

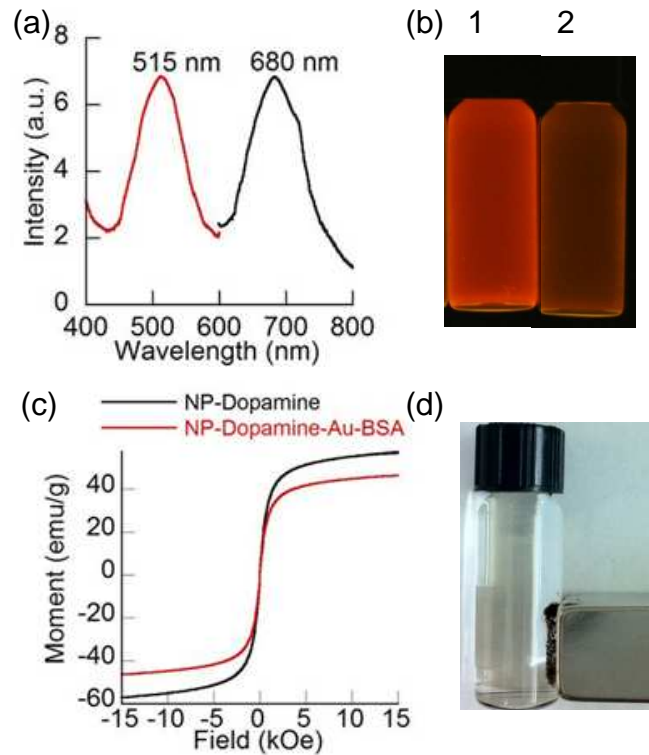


Figure 3.3 The integrated structure of iron oxide nanoparticles and Au nanoclusters: (a) fluorescent emission (excited at 520 nm) and excitation scans for 680 nm emission, (b) photographs of free BSA-Au nanoclusters-1 and the integrated nanostructures-2 under a 365 nm UV radiation, (c) magnetic moment versus applied magnetic fields curves of nanoparticles and the integrated nanostructures, (d) photographs of the integrated nanostructures under magnetic fields.

To quantify the fluorescent emission, the quantum yields of the free BSA-Au nanoclusters and the nanoclusters on the iron oxide nanoparticles surfaces were calculated. By comparing the wavelength-integrated fluorescence intensities of the samples to that of a standard fluorescent dye with known quantum yield, the quantum yields were estimated to be 0.065 for free nanoclusters and 0.08 for the nanoclusters on the nanoparticle surface. The slight increase in the quantum yield was not well understood at this point, but, further studies are on-going to study the photo-physical properties of the integrated nanostructure. The conjugation process did not greatly affect the magnetic properties of the iron oxide nanoparticles except for the decrease in

saturation magnetization (58 to 46 emu/g). Further, the rapid response of the integrated nanostructures to a magnet also indicated the strong magnetic property.

The small fluorescent nanoclusters under bright TEM were barely seen (Figure S3.4), but the HRTEM image of a typical integrated structure showed the presence of a single nanocluster on an iron oxide nanoparticle surface (Figure 3.4a). Further, the conjugated nanoclusters were clearly observed on the HAADF image (Figure 3.4b). Similar to the HRTEM observation, the HAADF image also suggested that one nanocluster was likely conjugated onto each iron oxide nanoparticle. This observation indirectly confirmed the assumption that all the Au atoms were made up of one nanocluster in each BSA molecule. This finding provided valuable information to the field, because the number of the Au atoms in each BSA molecule has been studied by mass spectroscopy, but the number of Au nanoclusters in each molecule remains unconfirmed. The exact numbers of Au nanoclusters on the iron oxide nanoparticle surface will be studied by anti-bunching experiments on florescent correlation spectroscopy (FCS) in the near future. This suggestion is supported by the observation that the small Au nanoparticle has only one favorable binding site to human serum albumin at domain I.³⁷ Further, it was also shown that the biological molecules have different packing density on a nanoparticle surface,³⁸ similar to the BSA molecule attachment to iron oxide nanoparticles. The conjugation of BSA-Au nanoclusters yielded a hydrodynamic size increase (24 to 39 nm) of the nanostructures as shown in Figure 3.4c. The extended tail of the DLS plot was likely from the undefined shape and size of the denatured BSA protein, because the Au nanoclusters were synthesized at very high pH (~12). The covalent conjugation of BSA-Au nanoclusters also shifted the negative zeta potential of the dopamine-coated nanoparticles from -42 to -37 mV (Figure 3.4d). Both the DLS plots and zeta-

potential measurements also support the successful conjugation of the nanoclusters to the iron oxide nanoparticle surfaces.

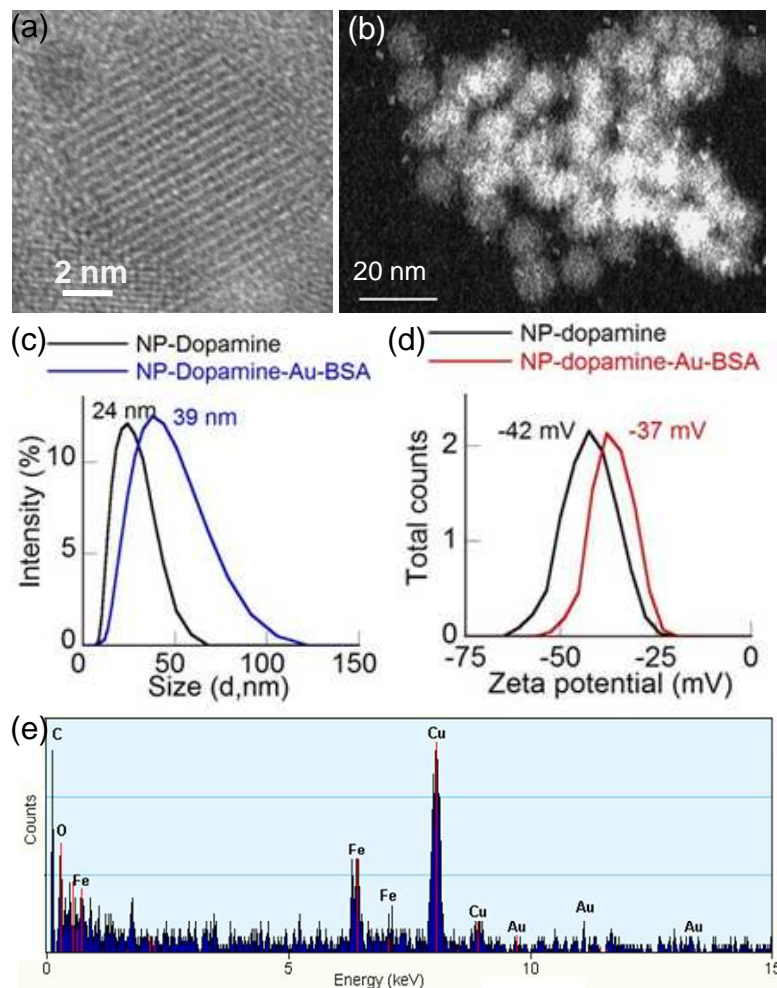


Figure 3.4 The integrated structure of iron oxide nanoparticles and Au nanoclusters: (a) HRTEM image, (b) HAADF TEM image, (c) DLS plots, (d) Zeta-potentials, and (e) EDX spectrum.

The structural integrity and the optical property of the integrated nanoparticles were studied in several biological buffers, including phosphate buffered saline (PBS), 4-(2-hydroxyethyl)-1-piperazineethanesulfonic acid (HEPES), 2-(N-morpholino)ethanesulfonic acid (MES), and EMEM cell growth medium. After 4 h incubation, the integrated nanoparticles remained their structural integrity based on the HAADF image (Figure S3.5). Interestingly, the intensity of the fluorescent emission increased in buffer solutions and returned to original after

re-dispersed in water (Figure S3.6). The fluorescent intensity increase was not fully understood at this point, further investigation will be performed to understand this phenomenon. One possible explanation is that the biological buffers temporally cross-linked the integrated nanoparticles together (Figure S3.5b), which limited their mobility, thus decreasing the collision probability between the nanoparticles. As a result, the external energy transfer rate and quantum yield could be increased, as suggested in Ref.39. Similarly, the temporal nanoparticle cross-linking could increase the local protein concentration; it was observed that protein adsorption led increase in the fluorescent intensity of Au nanoclusters.⁴⁰

3.4 Conclusion

In summary, a facile approach was reported for the integration of protein-stabilized fluorescent nanoclusters and the dopamine-coated iron oxide nanoparticles. This method is highly attractive because of its simplicity and versatility, where the catechol groups on nanoparticle surfaces can be readily activated by simply increasing the pH of the solution. No additional chemical linkers are needed for the conjugation. This approach will be highly useful to conjugate biological molecules with amino acid and/or thiol groups and are stable in slightly basic environments onto the surfaces of iron oxide nanoparticles. This conjugation principle was well demonstrated by the protein-encapsulated nanocluster conjugation. Another important contribution of this work is the direct observation of one nanocluster per nanoparticle conjugation by HAADF. This observation indirectly confirmed the assumption of one nanocluster per BSA molecule. The stability of the integrated nanoparticles in various buffers in terms of structural integrity and optical property suggested their potential in biological applications.

Acknowledgement

This work is supported by NSF-DMR 0907204. We acknowledge the UA Central Analytical Facility (CAF) and the Biological Science Department for the use of TEM. Y. Bao also acknowledges the State Key Laboratory of Molecular Engineering of Engineering, Shanghai, China.

Supporting Information

UV-vis absorption spectra of (a) time-dependent oxidation of free dopamine solution, (b) dopamine-coated iron oxide nanoparticle solution, (c) H₂AuCl₄ solution at different pH and with addition of NaCl, (d) Au amino acid complexes, and (e) integrated nanostructures in various buffers. HAADF and bright field TEM images of the integrated nanoparticles in HEPES buffer. This material is available free of charge via the Internet at <http://pubs.acs.org>.”

3.5 References

1. Lee, DE.; Koo, H.; Sun, IC.; Ryu, J. H.; Kim, K.; Kwon, IC. *Chem. Soc. Rev.* **2012**, *41*, 2652-2672.
2. Jin, Y.; Jia, C.; Huang, S.; O'Donnell, M.; Gao, X. *Nat. Commun.* **2010**, *1*(45).
3. Bao, Y.; Calderon, H.; Krishnan, K. M. *J. Phys. Chem. C* **2007**, *111*, 1941-1944.
4. Reimer, P.; Balzer, T. *Eur. Radiol.* **2003**, *13*, 1266-1276.
5. Weiss, S. *Science* **1999**, *283*, 1676-1683.
6. Sako, Y.; Yanagida, T. *Nat. Rev. Mol. Cell Biol.* **2003**, *4*, SS1-SS5.
7. Krishnan, K. M. *IEEE Trans. on Magn.* **2010**, *46*, 2523-2558.
8. Corr, S. A.; Rakovich, YP.; Gun'ko, YK. *Nanoscale Res. Lett.* **2008**, *3*, 87-104.
9. Quarta, A.; Corato, RD.; Manna, L.; Ragusa, A.; Pellegrino, T. *IEEE Trans. Nanobios.* **2007**, *6*, 298-308.
10. Park, JH.; Maltzahn, GV.; Ruoslahti, E.; Bhatia, SN.; Sailor, MJ. *Angew. Chem. Int. Ed.* **2008**, *47*, 7284-7288.
11. Yi, DK.; Selvan, ST.; Lee, SS.; Papaefthymiou, GC.; Kundaliya, D.; Ying, J. *J. Am. Chem. Soc.* **2005**, *127*, 4990-4991.
12. Beaune, G.; Menager, C.; Cabuil, V. *J. Phys. Chem. B* **2008**, *112*, 7424-7429.
13. Li, L.; Chen, D.; Zhang, Y.; Deng, Z.; Ren, X.; Meng, X.; Tang, F.; Ren, J.; Zhang, L. *Nanotechnology* **2007**, *18* (40).
14. Salgueirino-Maceira, V.; Correa-Duarte, M. A.; Spasova, M.; Liz-Marzan, L. M.; Farle, M. *Adv. Funct. Mater.* **2006**, *16*, 509-514.
15. Lu, C.; Hung, Y.; Hsiao, J. K.; Yao, M.; Chung, T.; Lin, Y.; Wu, S.; Hsu, S.; Liu, H.; Mou, C.; Yang, C.; Huang, D.; Chen, Y. *Nano Lett.* **2007**, *7*, 149-154.
16. Bertorelle, F.; Wilhelm, C.; Roger, J.; Gazeau, F.; Menager, C.; Cabuil, V. *Langmuir* **2006**, *22*, 5385-5391.
17. Gao, J.; Zhang, B.; Gao, Y.; Pan, Y.; Zhang, X.; Xu, B. *J. Am. Chem. Soc.* **2007**, *129*, 11928-11935.
18. Kim, H.; Achermann, M.; Balet, LP.; Hollingsworth, JA.; Klimov, VI. *J. Am. Chem. Soc.* **2005**, *127*, 544-546.
19. Gu, H.; Zheng, R.; Zhang, X.; Xu, B. *J. Am. Chem. Soc.* **2004**, *126*, 5664-5665.
20. Yang, Q.; Liu, J.; Chen, H.; Wang, X.; Huang, Q.; Shan, Z. *Prog. Chem.* **2011**, *23*, 880-892.

21. Liu, C.; Wu, H.; Hsiao, Y.; Lai, C.; Shih, C. W.; Peng, Y.; Tang, K.; Chang, H.; Chien, Y.; Hsiao, J.; Cheng, J.; Chou, P. *Angew. Chem. Int. Ed.* **2011**, *50*, 7056-7060.
22. Durgadas, CV.; Sharma, P.; Sreenivasan, K. *Nanoscale* **2011**, *3*, 4780-4787.
23. Palchoudhury, S.; Xu, Y.; An, W.; Turner, CH.; Bao, Y. *J. Appl. Phys.* **2010**, *107*, 09B311.
24. Xu, Y.; Qin, Y.; Palchoudhury, S.; Bao, Y. *Langmuir* **2011**, *27*, 8990-8997.
25. Palchoudhury, S.; Xu, Y.; Goodwin, J.; Bao, Y. *J. Mater. Chem.* **2011**, *21*, 3966-3970.
26. Xie, J.; Zheng, Y.; Ying, J. *J. Am. Chem. Soc.* **2009**, *131*, 888-889.
27. Palchoudhury, S.; Xu, Y.; Goodwin, J.; Bao, Y. *J. Appl. Phys.* **2011**, *109*, 07E314.
28. Shultz, MD.; Reveles, JU.; Khanna, SN.; Carpenter, EE. *J. Am. Chem. Soc.* **2007**, *129*, 2482-2487.
29. Stuart, BH. *Infrared Spectroscopy: Fundamentals and Applications*. John Wiley & Sons, NJ, USA, **2004**, pp. 80.
30. Wang, X.; Jin, B. K.; Lin, X. *Anal. Sci.* **2002**, *18*, 931-933.
31. Lee, H.; Rho, J.; Messersmith, PB. *Adv. Mater.* **2009**, *21*, 431-434.
32. Lee, H.; Dellatore, SM.; Miller, WM.; Messersmith, PB. *Science* **2007**, *318*, 426-430.
33. Katchalski, E.; Benjamin, GS.; Gross, V. *J. Am. Chem. Soc.* **1957**, *79*, 4096-4099.
34. Liang, X.; Wang, Z.; Liu, C. *Nanoscale Res. Lett.* **2010**, *5*, 124-129.
35. Esumi, K.; Suzuki, A.; Yamahira, A.; Torigoe, K. *Langmuir* **2000**, *16*, 2604-2608.
36. Guevel, X. L.; Hotzer, B.; Jung, G.; Hollemeyer, K.; Trouillet, V.; Schneider, M. *J. Phys. Chem. C* **2011**, *115*, 10955-10963.
37. Sen, T.; Mandal, S.; Haldar, S.; Chattopadhyay, K.; Patra, A. *J. Phys. Chem. C* **2011**, *115*, 24037-24044.
38. Li, Z.; Cheng, E.; Huang, W.; Zhang, T.; Yang, Z.; Liu, D.; Tang, Z. *J. Am. Chem. Soc.* **2011**, *133*, 15284-15287.
39. Xiang, D.; Zeng, G.; Zhai, K.; Li, L.; He, Z. *Analyst* **2011**, *136*, 2837-2844.
40. Shang, L.; Brandholt, S.; Stochmar, F.; Trouillet, V.; Bruns, M.; Nienhaus, GU. *Small* **2011**, *8*, 661-665.

3.6 Supporting information

3.6.1 Dopamine oxidation

Free dopamine solution was used as a comparison to the dopamine-coated nanoparticles. The dopamine water solution (0.4 mg/mL) was oxidized by adjusting its pH to 9 using NaOH. The time-dependent UV-vis absorption spectra were recorded, as shown in Figure S3.1. The dopamine-coated iron oxide nanoparticle solution itself exhibits a strong absorption in the range of 300 - 600 nm.

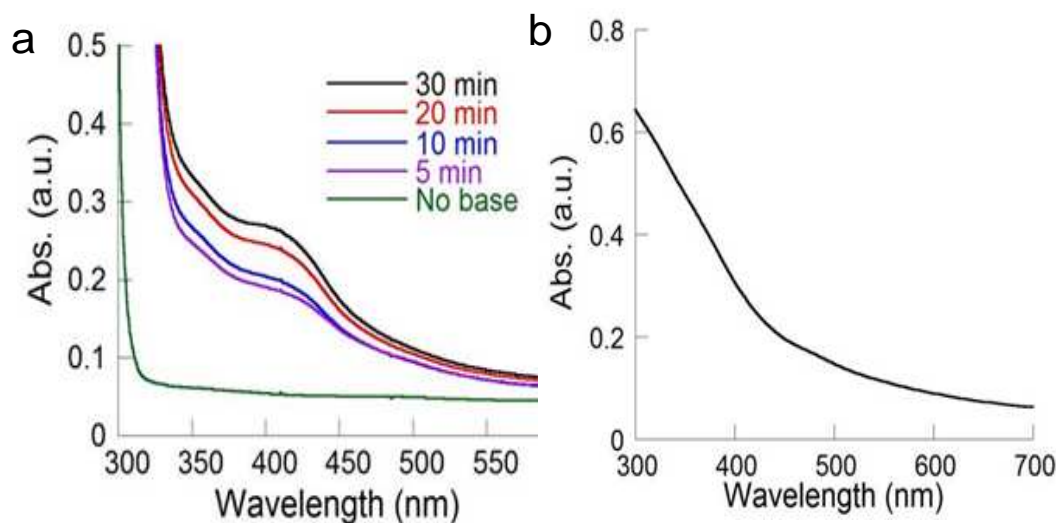


Figure S3.1 UV-vis absorption spectra of (a) time-dependent oxidation of free dopamine solution, and (b) dopamine-coated iron oxide nanoparticle solution.

3.6.2 Role of specific amino acids in nanocluster formation

HAuCl_4 solution is highly acidic (pH 2) and the AuCl_4^- complex exhibits two typical absorption bands (217 and 287 nm), as shown in Figure S3.2a. After diluted in water (pH 6), the absorption spectra of the HAuCl_4 solution shifted to lower wavelength (Figure S3.2a). We attributed the shifts to the reduction of the Au(III) to Au(I), because the pH dependent reduction potential of Au ions. To rule out the possibility of ligand replacement (e.g. Cl^- to OH^-), NaCl, with a molar ratio of 5:1 to Au was added to the solution, ensuring the presence of Au chloride

complexes. Similar shifts in the absorption spectra were observed (Figure S3.2b). Therefore, we believe that the spectrum shift is related to the reduction of Au(III) to Au(I). This spectrum shift was used to study the interaction between specific amino acids and HAuCl_4 .

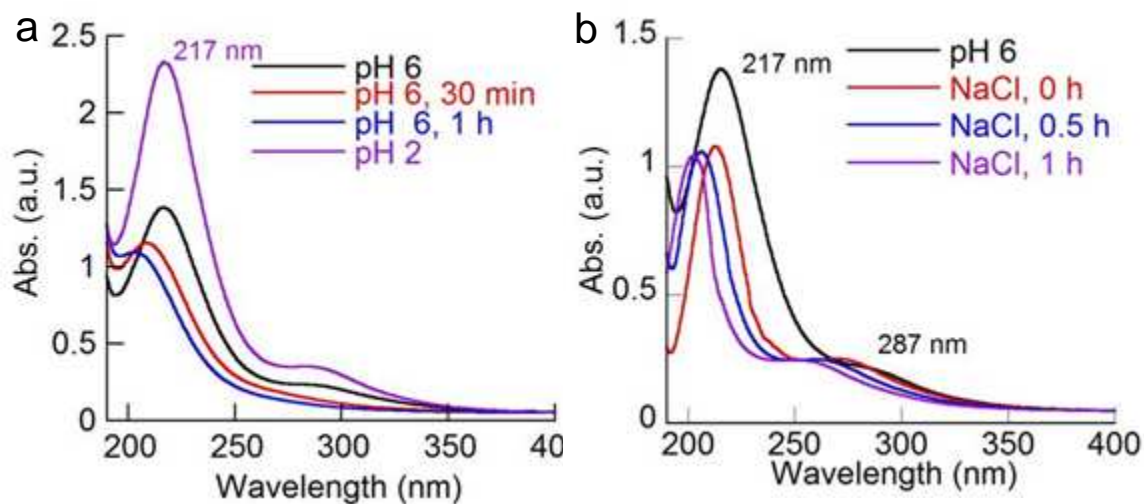


Figure S3.2 UV-vis absorption spectra of HAuCl_4 solution at pH 2- the original solution, pH 6- right after dilution into water, 30 min and 1 h after dilution.

To study the role of specific amino acids within BSA, lysine (1.71 mg), arginine (3.32 mg), and histidine (0.94 mg) water solution (pH 6) were prepared, where the amounts of amino acids were set to be equivalent to the amino acid amounts in 25 mg of BSA. Then, 1.7 mL HAuCl_4 solution were added to each amino acid solution and UV-vis spectra were collected (Figure S3.3)

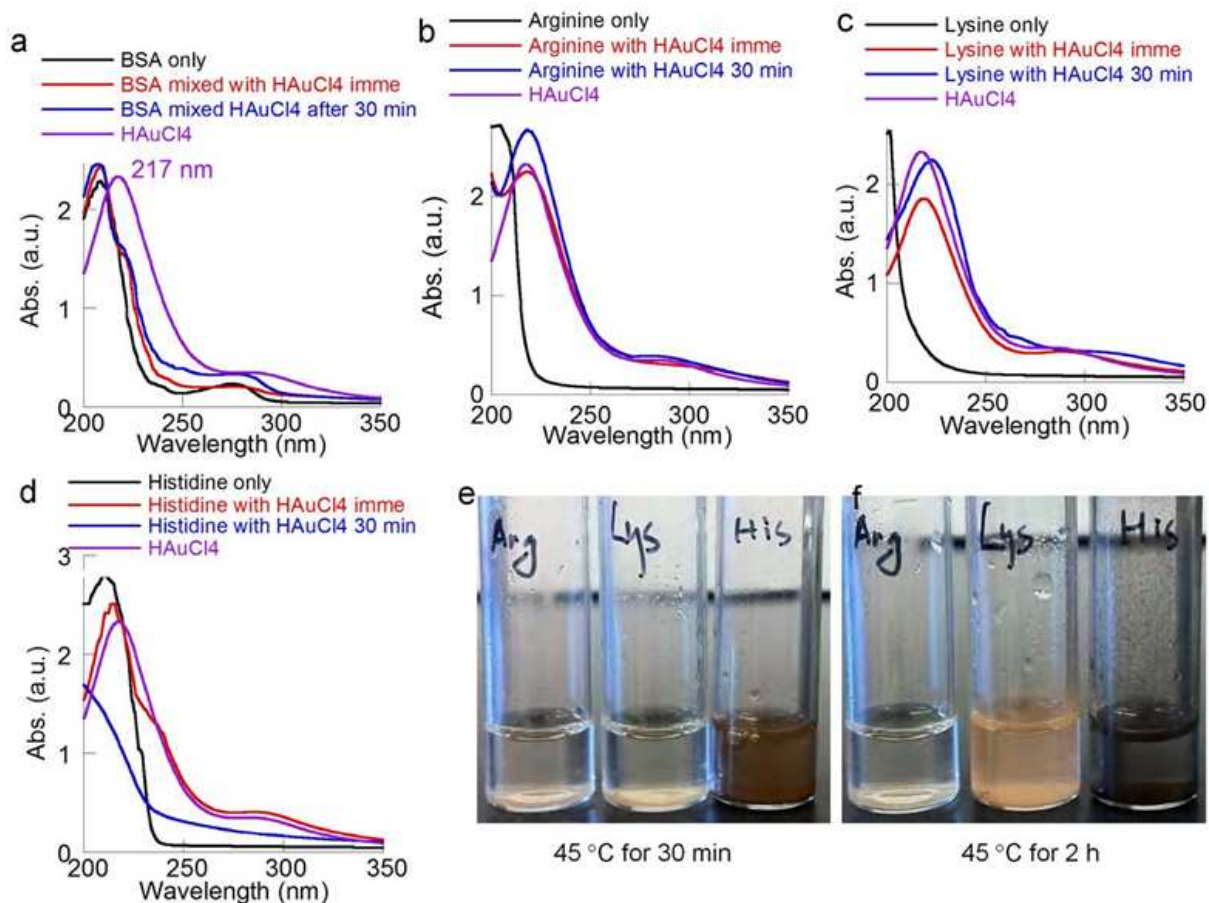


Figure S3.3 UV-vis absorption spectra of HAuCl₄ and BSA (a), arginine (b), Lysine (c), histidine (d) reaction solution, and (e & f) photographs of reaction mixtures.

3.6.3 Bright field TEM image of the integrated nanoparticles

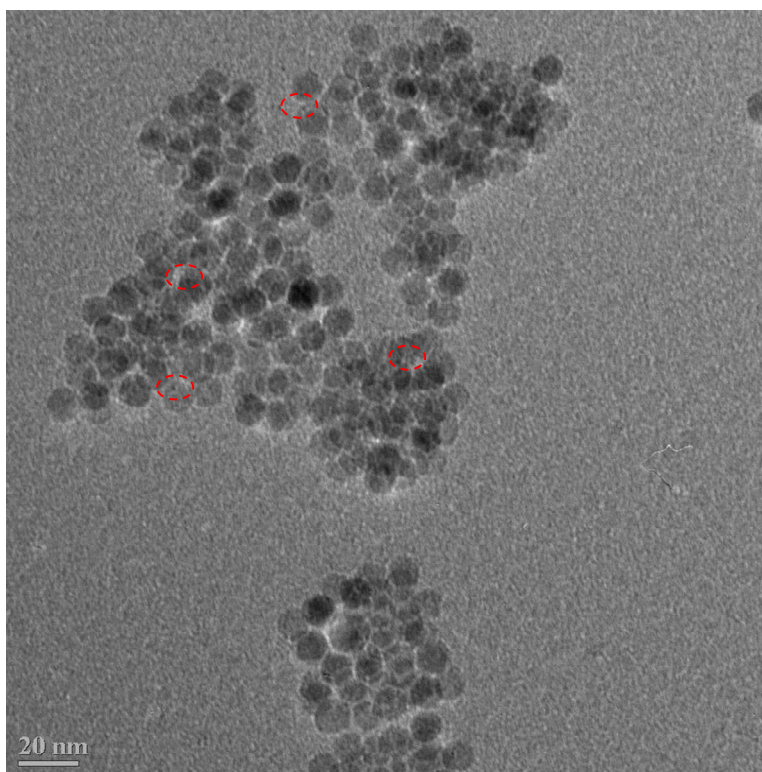


Figure S3.4 Bright field TEM image of the integrated nanoparticles.

3.6.4 Stability tests of integrated nanoparticles

Stability in biological buffers: The structural integrity and the optical property of the integrated nanoparticles were studied in various buffers, including PBS (1X), HEPES (10 mM), MES (10 mM) and EMEM (10 % FBS supplemented). In brief, the integrated nanoparticle solution (1 mL) was mixed with each buffer respectively at a volume ratio of 1:1. After 4 h mixing, the conjugated nanoparticles were magnetically separated out of the mixture and re-dispersed into 1 mL water. A typical TEM image of the integrated nanoparticles in MES buffer is shown in Figure S3.5. The fluorescent emission plots of the all samples are shown in Figure S3.6.

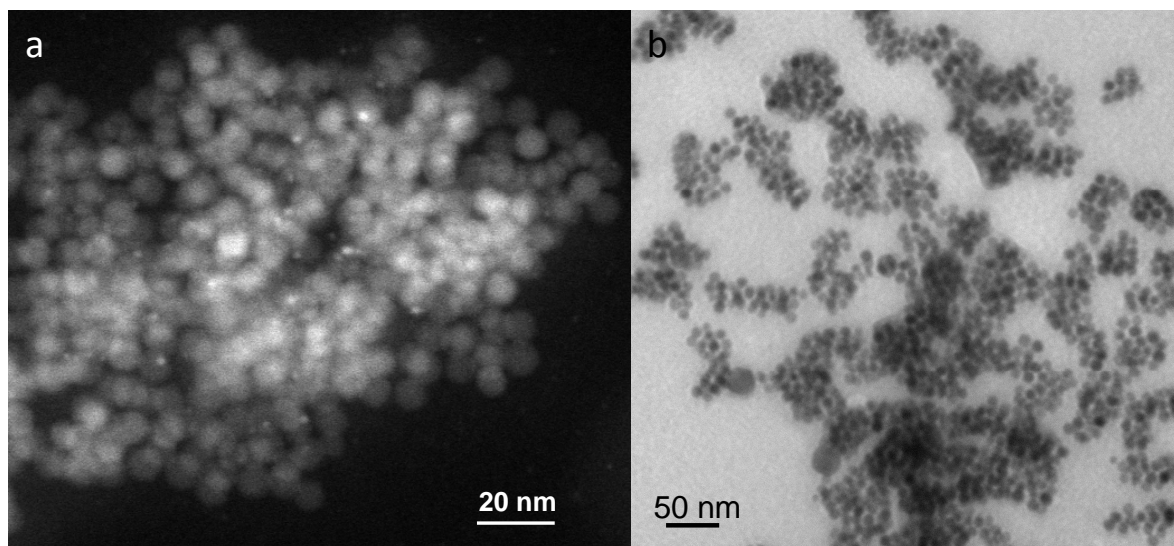


Figure S3.5. The integrated nanoparticles in HEPES buffer: (a) HAADF image, and (b) bright field TEM image.

pH stability test: The pH stability tests of the conjugated nanoparticles were conducted by adjusting the pH of the nanoparticle solution to 4. The stability of the integrated nanoparticles at high pH (12, during synthesis) and neutral pH (7, storage) has been demonstrated during synthesis and storage. The fluorescence emission plots of the integrated nanoparticles at neutral and acidic environment are shown in Figure S3.6e.

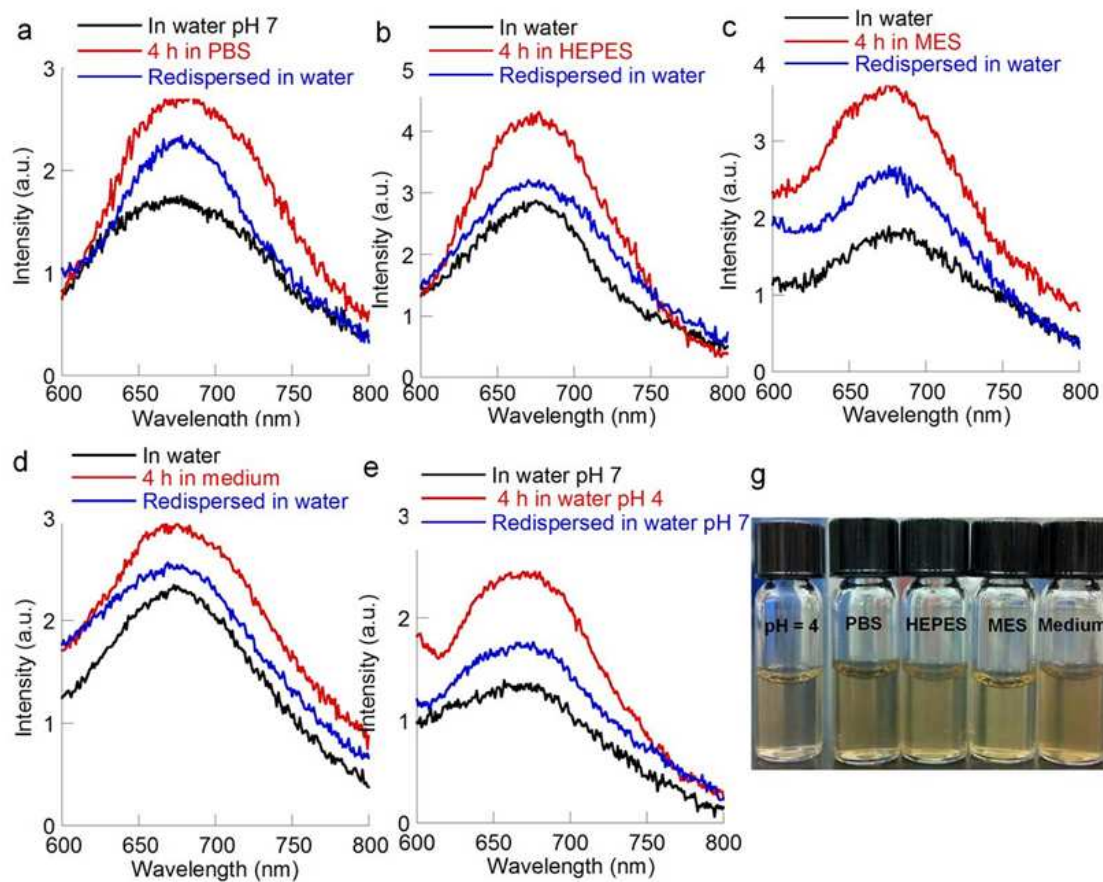


Figure S3.6. UV-vis absorption spectra of the integrated nanoparticles in various buffers: (a), PBS, (b) HEPES, (c), MES, (d) reaction solution and (e & f) photographs of reaction mixtures.

CHAPTER 4

THE ROLE OF PROTEIN CHARACTERISTICS IN THE FORMATION AND FLUORESCENCE OF AU NANOCCLUSERS

(Published in *Nanoscale* **2014**, 3, 1515–1524)

Yaolin Xu, Jennifer Sherwood, Ying Qin, Dorothy Crowley, Marco Bonizzoni, and Yuping Bao*

ABSTRACT

Protein-encapsulated gold nanoclusters have shown many advantages over other gold nanocluster systems, including green synthesis, biocompatibility, high water solubility, and the ease of further conjugation. In this article, we systematically investigated the effects of the protein size and amino acid content on the formation and fluorescent properties of gold nanoclusters using four model proteins (bovine serum albumin, lysozyme, trypsin, and pepsin). We discovered that the balance of amine and tyrosine/tryptophan containing residues was critical for the nanocluster formation. Protein templates with low cysteine content caused blue shifts in the fluorescent emissions and difference in fluorescent lifetimes of the Au nanoclusters. Furthermore, the protein size was found to be a critical factor for the photostability and long-term stability of Au nanoclusters. The size of the protein also affected the Au nanocluster behaviour after immobilization.

4.1 Introduction

Fluorescent gold (Au) nanoclusters have attracted much attention due to their emerging photophysical properties and potential applications in biolabeling and sensing.¹⁻⁴ Motivated by their potential applications, fluorescent Au nanoclusters have been synthesized using many different capping molecules, such as glutathione,⁵ dodecanethiol,⁶ dendrimer,^{7, 8} meso-2,3-dimercapsuccinic acid,⁹ Good's buffer,^{10, 11} DNA,¹²⁻¹⁴ and proteins.^{15, 16} Among these synthetic methods, protein-directed synthesis is particularly attractive, because proteins serve as environmentally-benign reducing and stabilizing molecules, require only mild reaction conditions, offer great water solubility and natural biocompatibility.¹⁵ Furthermore, the 3D complexed structure of the proteins can withstand a wide range of pH and can be easily conjugated with other systems. So far, a number of proteins have been explored for synthesizing fluorescent Au nanoclusters, including bovine serum albumin (BSA),¹⁶⁻¹⁸ lysozyme,^{19, 20} human transferrin,^{21, 22} lactoferrin,²³ trypsin,²⁴ pepsin,²⁵ insulin,²⁶ and horseradish peroxidase.²⁷ Depending upon the reaction conditions, the nanoclusters were formed either under protein-denatured conditions¹⁶ or native condition.²⁶ The protein-templates are expected to influence the nanocluster formation and property because of the diversity in amino acid contents and sequences of proteins.

Most mechanistic studies on the nanocluster formation and fluorescent emissions have been focused on BSA-encapsulated nanoclusters.^{17, 23} Our previous study showed that the amine-containing amino acids of the proteins were responsible for the Au ion uptake, and the increase of pH to 7 led to the reduction of Au (III) to Au(I); and then tyrosine or tryptophan reduced Au(I) to metallic Au at higher pH (> 10).²⁸ The fluorescent emission of BSA-Au nanoclusters was proposed to originate from Au₂₅ nanoclusters, which were composed of a Au₁₃ core and 12

Au(I) sulphur complex, forming six $-S-Au(I)-S-Au(I)-S-$ staple surface motifs.²⁸⁻³⁰ This hypothesis suggested that 18 thiol groups (cysteine residues) in a protein template were necessary to form the staple surface motifs. However, Au nanoclusters have been synthesized using proteins with much fewer cysteine residues than that of BSA, such as insulin (6 cysteines)²⁶ and trypsin (7 cysteines).²⁴ Thus, the stabilization mechanism of Au nanoclusters in proteins remains an open question.

Apart from the nanocluster formation, the optical properties of fluorescent nanoclusters are subject to various local environmental conditions, such as pH,³¹ the addition of chemicals,^{32, 33} and protein absorption.³⁴ It remains unclear how the protein templates affect the nanocluster behaviours under various environmental conditions. Furthermore, fluorescent Au nanoclusters are normally conjugated to other molecules or immobilized onto surfaces to serve as fluorescent tags or sensing signal. However, little has been done to investigate the immobilization effects on the fluorescent properties of Au nanoclusters.

In this article, we systematically investigated the fundamental issues related to protein-Au nanoclusters by comparing 4 model protein systems (*e.g.*, bovine serum albumin-BSA, lysozyme, trypsin, and pepsin). Specifically, we studied: (1) the effects of protein size and amino acid contents on the nanocluster formation and fluorescent properties, (2) the chemical and photo stability of Au nanoclusters produced by three different proteins, and (3) the immobilization effects on Au nanoclusters generated by different proteins. We discovered that the balance of amine and tyrosine/tryptophan containing residues was critical for nanocluster formation. Protein templates with low cysteine content caused blue shifts in the fluorescent emissions and differences in fluorescent lifetimes of the Au nanoclusters. Furthermore, the protein size served as a critical factor for the photostability and long-term stability of Au

nanoclusters. The size of the protein also affected the Au nanocluster behaviour after immobilization. The fundamental understanding of protein-Au nanocluster interactions will lead to further advancement in nanocluster design and synthesis, beneficial to biological and biomedical applications.

4.2 Experiments

4.2.1 Chemicals

All the proteins were purchased in lyophilized-powder form and used without further purification. These proteins include: Bovine serum albumin (BSA, OmniPur), lysozyme (egg white, OmniPur), trypsin (bovine pancreas, Alfa Aesar), and pepsin (proteomic grade, Amresco). Gold chloride aqueous solution (HAuCl_4 , 0.2 wt%) was purchased from Electron Microscopy Sciences.

4.2.2 Synthesis of protein-encapsulated gold nanoclusters

The fluorescent Au nanoclusters were synthesized following a procedure similar to our previously-reported method.²⁸ To investigate the effects of protein characteristics, four sets of experiments were performed: (1) The molar ratios of proteins to Au were kept the same, where 1 mL of freshly prepared protein solutions (BSA - 12.5 mg, trypsin - 4.6 mg, lysozyme - 2.7 mg, or pepsin - 6.5 mg) were mixed with 0.85 mL of cold HAuCl_4 solutions (0.2 wt%). (2) The ratios of the amine functional groups to Au were kept the same (4 to 1, where 1 mL of freshly prepared protein solutions (BSA - 12.5 mg, trypsin - 24.4 mg, and lysozyme - 15.0 mg) were mixed with 0.85 mL of cold HAuCl_4 solutions (0.2 wt%). (3) The molar ratios of tyrosine/tryptophan to Au were kept the same, where 0.85 of freshly prepared protein solutions (BSA - 12.5 mg, trypsin - 7.8 mg, lysozyme - 7.1 mg) were mixed with 0.85 mL of cold HAuCl_4 solutions (0.2 wt%). (4) The Au amount was kept the same while the amounts of proteins were adjusted to achieve the

highest fluorescent intensities. Specifically, 1 mL of freshly prepared protein solutions (BSA-12.5 mg, lysozyme-12.5 mg, or trypsin-15 mg) were mixed with 0.85 mL of cold HAuCl_4 solutions (0.2 wt%). For all the reactions, the reaction mixtures were stirred at room temperature for an hour, allowing for the complexation of Au ions with protein molecules. Then, 0.5 mL of NaOH solution (1 M) was added into each reaction mixture and kept at 45 °C for desirable times depending on the protein. The obtained yellowish Au nanocluster solutions were used for characterization, stability tests, and immobilization studies. The isoelectric points (PIs) of the proteins were measured by titrating HCl to the solution until proteins were fully precipitated out, forming a clear solution.

4.2.3 Lifetime measurements

Fluorescence lifetimes of the protein-Au nanoclusters in HEPES bufer (20 mM, pH 7.4) were measured with an Edinburgh Photonics Mini-Tau time-resolved fluorimeter using the time-correlated single photon counting technique (TC-SPC). The samples were excited by a diode laser emitting at 485 nm, with pulse width of 150 ps set to a 20 kHz pulse repetition rate. Control of the excitation power was achieved through a continuously variable neutral density filter wheel to collect ca. 400 photons/s (2% of excitation rate). A Thorlabs long-pass filter with a 600 nm cut-on wavelength was used for emission selection. Photons were detected over a time range up to 20 μs by a high-sensitivity photomultiplier tube. Decay curves were accumulated until 10,000 counts were collected at the highest peak in the curve. The sample temperature was controlled to 25°C by an external circulating water bath. The intensity decay data was fitted to the following two-exponential model using a non-linear curve fitting routine implemented in house in the Mathematica v. 9.0 software.

4.2.4 Stability tests

The stability of the protein-encapsulated Au nanoclusters was studied by monitoring their fluorescence change under various conditions, such as pH, buffers, temperature, and UV radiation. The pH effects were studied by adjusting the pHs of the protein-encapsulated Au nanoclusters solutions with HCl/NaOH in a cycle (pH= 12→9→7→5→7→9→12). At each pH, the solution was allowed equilibrating for 20 minutes before fluorescence measurement. The effects of the buffer conditions were achieved via dialysis of the nanocluster water solution in buffers for 4 hours. These buffers include phosphate buffered saline (PBS), 4-(2-hydroxyethyl)-1-piperazineethanesulfonic acid (HEPES), 2-(N-morpholino)ethanesulfonic acid (MES), and 2-amino-2-hydroxymethyl-propane-1,3-diol (Tris). The photostability was studied by measuring the fluorescence of the Au nanoclusters after UV radiation (0, 15 min, 30 min, 1, 2, 5 hours). The temperature effects were studied by merging the nanocluster solutions in a water bath at pre-set temperatures for 20 minutes and then immediately measuring their fluorescent emission. The temperature was set in a cycle (22→37→45→55→45→37→22 °C). The long-term stability of the nanoclusters was studied in both in solution and powder form samples.

4.2.5 Immobilization effects

The immobilization effects were studied by immobilizing the protein-encapsulated Au nanoclusters onto iron oxide nanoparticle surfaces following our previously reported procedures.²⁸ In brief, 12 nm spherical iron oxide nanoparticles were prepared using our modified "heat-up" method.³⁵⁻³⁷ and then dopamine molecules were attached on the nanoparticle surfaces via a ligand exchange approach.³⁵ The catechol groups on the nanoparticle surface can effectively interact with proteins upon activation. Briefly, 1.28 mL freshly-prepared lysozyme-gold nanocluster solution was mixed with 0.5 mL activated iron oxide nanoparticle solution (1 mg/mL). After 12 hour incubation (22 °C), the conjugated nanoparticles were magnetically

separated out of the solution. This process was repeated twice to remove the free nanoclusters. The integrated nanostructures were then re-dispersed in water (0.5 mL) for further characterization. Alternatively, the nanoclusters were immobilized onto the inner surface of glass vials (2 mL) through a dopamine coating layer, and then the immobilized nanoclusters was immersed inside water to avoid drying. The glass vials with the immobilized nanoclusters were measured directly on the fluorescent spectrometer.

4.2.6 Characterization

The fluorescent spectra of protein-encapsulated Au nanoclusters were collected using a Cary Eclipse fluorescence spectrophotometer. The UV–vis spectra were recorded on a Shimadzu UV–vis spectrophotometer (UV-1700 series). The morphology and size of the protein-encapsulated gold nanoclusters were examined under transmission electron microscopy (TEM, FEI Tecnai, F-20, 200 kV). The surface chemistry of the nanoparticles was studied by Fourier transform infrared spectroscopy (FTIR).

4.3 Results and Discussion

The effects of the protein size and amino acid content on the formation of the fluorescent Au nanocluster were studied using four model proteins (BSA, lysozyme, trypsin, and pepsin). During the synthesis of Au nanoclusters, several groups of amino acids are critically important to the formation and stabilization of the nanoclusters. First, the positively charged amino acids (*e.g.*, arginine, and lysine) are responsible for the coordination of the AuCl_4^- ions, which determine the amounts of Au can be incorporated into the proteins. Second, the amount of trypsin/tryptophan residues is important to reduce the Au ions, thus directly influencing the reaction rate. Finally, the cysteine residues are an important group to stabilize the Au nanoclusters because of the strong interaction between Au and thiol groups. Table 4.1 shows the

characteristics of the four proteins, including protein sizes and contents of key amino acid residues. The difference in these characteristics serves as the basis for cross-comparison. The sizes of proteins decrease in the order of BSA > pepsin > trypsin > lysozyme, while except for BSA, the other three proteins have similar cysteine content (pepsin-7, trypsin-7, and lysozyme-8). The considerable difference in amine-containing residues among these four proteins, such as lysine (BSA-60, trypsin-14, lysozyme-6, and pepsine-1) allows studying the role of amine groups in the nanocluster formation. The amine-containing residues are key groups to complex Au ions and subsequently determine the Au uptake.

Table 4.1. The characteristics of four model proteins

Proteins		BSA (66 kDa) (636 AA)	Trypsin (24 kDa) (223 AA)	Lysozyme (14 kDa) (129 AA)	Pepsin (34 kDa) (327 AA)
Amino acid # (to Au ³⁺)					
(a)	Arginine: Au ³⁺	26	2	11	2
	Lysine: Au ³⁺	60	14	6	1
	Histidine: Au ³⁺	16	3	1	1
	<i>Total (positive-charged) AA to Au³⁺</i>	102	19	18	4
(b)	Tyrosine: Au ³⁺	21	10	3	18
	Tryptophan: Au ³⁺	3	4	6	6
	<i>Total (reducing) AA to Au³⁺</i>	24	14	9	24
(c)	Cysteine: Au ³⁺	35	7	8	7

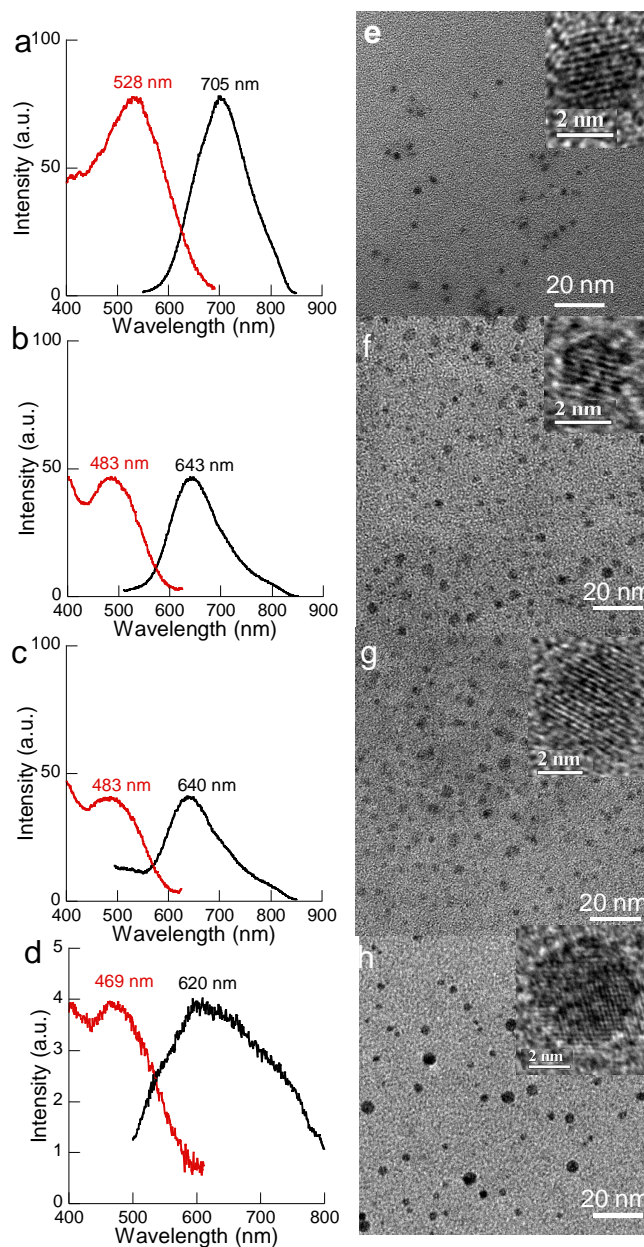


Figure 4.1. Protein-encapsulated Au nanostructures: fluorescent emission (black)/excitation (red) spectra and TEM images of Au nanoclusters generated from BSA (a and e), trypsin (b and f), lysozyme (c and g), and pepsin (d and h).

To investigate the effects of protein characteristics, four sets of experiments were performed: (1) the same molar ratio of protein to Au, (2) the same molar ratio of the amine functional groups to Au, (3) the same molar ratio of tyrosine/tryptophan to Au, and (4) excess proteins with the same amount of Au. The molar ratio of protein to Au was set at 0.04 based on

previous reports that Au₂₅ nanoclusters were generally produced with BSA proteins.²³ Figure 4.1 a-d shows the fluorescent emission and excitation spectra of the nanoclusters generated using BSA, trypsin, lysozyme, and pepsin respectively. Compared to the emission peak ($\lambda_{em, max}$ 705 nm) of BSA-Au nanoclusters, the emission maxima of the Au nanoclusters produced using trypsin, lysozyme, and pepsin showed more than 60 nm blue shift (e.g., trypsin - 643 nm; lysozyme - 640 nm, and pepsin - 620 nm) and with much lower fluorescent intensity, in particular for the pepsin reaction. The low fluorescent intensities were mainly due to the ineffective protection of the protein templates, leading to the formation of large size nanoparticles (Figure 4.1f-h). However, the typical 520 nm absorption peak of Au nanoparticles was barely detected for both trypsin and lysozyme samples (Figure S4.1), likely because of the percentage of the large nanoparticles was low. Interestingly, the pepsin reaction only showed detectable fluorescence after 1 h reaction and then the fluorescence kept decreasing and was barely detectable after 4 h. Instead, the typical UV-visible absorption peak at 520 nm of Au nanoparticles was clearly observed (Figure S4.2), indicating the formation of larger Au nanoparticles. The formation of Au nanoparticles rather than fluorescent nanoclusters for pepsin can be understood by the amine-containing and tyrosine/tryptophan residues in pepsin. Pepsin only contains 4 amine-containing residues, which did not allow effective complexation with AuCl₄⁻ ions. Further, the high tyrosine/tryptophan content rapidly reduced the Au ions, leading to the formation of Au nanoparticles. This observation is inconsistent with previous reports on the formation of Au nanoclusters with pepsin.²⁵ We believe that the inconsistency is due to the protein source and purity, where other components might contribute to the formation of Au nanoclusters. Because of the difficult to produce pepsin-Au nanoclusters with high fluorescence,

the rest of comparison studies were primarily on the other three proteins (BSA, trypsin and lysozyme).

The blue shifts in fluorescent emissions of trypsin and lysozyme could be from either smaller nanoclusters or environmental effects. Based on the TEM images (Figure 4.1 f and g), wide size distribution of the Au nanoclusters were observed for both samples. In addition, the HRTEM did show a smaller cluster size. We attributed the low fluorescent intensity and wide size distribution of the Au nanoclusters to the ineffective protection because of the smaller sized proteins and low cysteine contents. To ensure that enough proteins were available to protect the nanoclusters, the protein amounts of trypsin and lysozyme were adjusted to achieve the highest fluorescent intensity. After optimization, the proteins to Au ratios were found to be 0.13 to 1 for trypsin and 0.18 to 1 for lysozyme, which was much higher than that of BSA to Au (0.04 to 1). Trypsin and lysozyme have similar numbers of thiol groups; the higher amount of lysozyme required to stabilize the Au nanoclusters suggested the importance of protein size.

Figure 4.2 shows the fluorescent emission/excitation plots and TEM images of Au nanoclusters generated with excess trypsin and lysozyme. Compared to the emission peak ($\lambda_{em, max}$ 705 nm) of BSA-Au nanoclusters in Figure 4.1a, the emission maxima of the Au nanoclusters produced using excess trypsin and lysozyme showed more than 30 nm blue shift (e.g., trypsin - 669 nm; lysozyme - 671 nm). However, with enough proteins, uniform Au nanoclusters were produced using both trypsin and lysozyme (Figure 4.2b and d). Interestingly, the sizes of the Au nanoclusters from excess lysozyme and trypsin were very similar to that of the BSA-Au nanoclusters (Figure 4.1e). Therefore, we believed that the blue shifts in fluorescent emissions were a result of local environments (e.g., coordinating functional groups, hydrophobicity). Previous reports on BSA-Au nanoclusters suggested that the fluorescent emission was from Au₂₅

nanoclusters, including a core (Au₁₃) emission at higher wavelength and an emission from the surface staple motif [-S-Au-S-Au-S-] at lower wavelength.^{29, 30} With this assumption, 18 cysteine residues are required to form six staple surface motifs. For proteins with less thiol contents, such as trypsin (7) and lysozyme (8), the formation of the surface staple motif in a single protein is limited. To stabilize the Au nanoclusters, either multiple proteins are involved or other amino acids (e.g., -NH₂) contribute to stabilizing the Au nanoclusters.

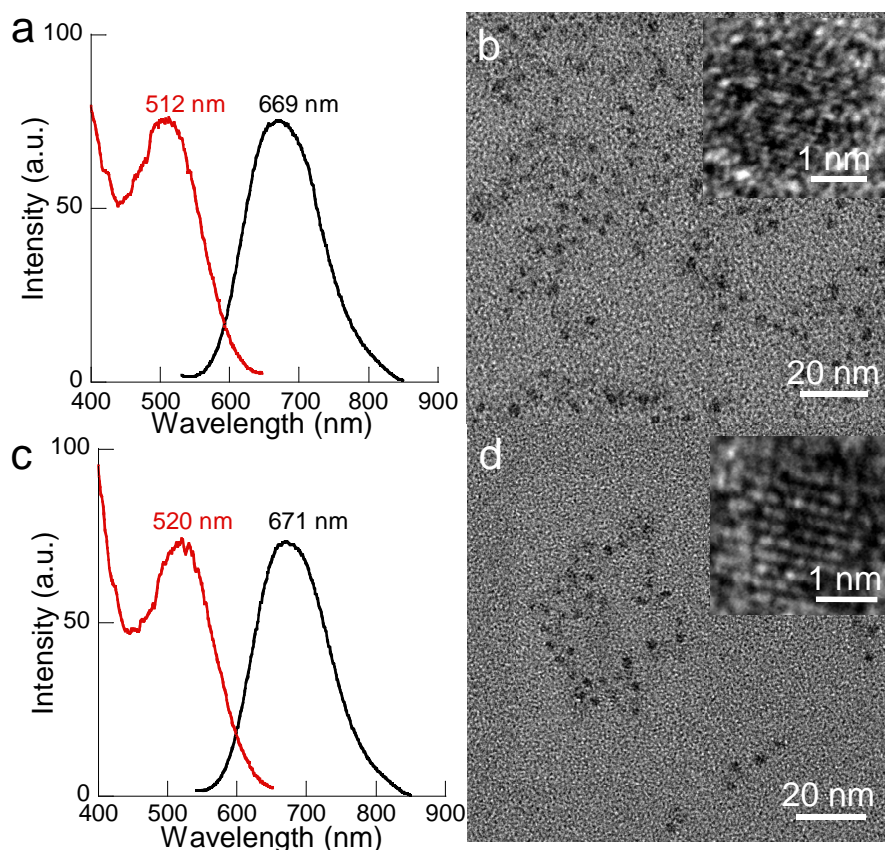


Figure 4.2. Fluorescent emission (black)/excitation (red) spectra and TEM images of Au nanoclusters generated from excess trypsin (a and b), and lysozyme (c and d).

Here, we proposed that the amine groups were involved in the stabilization of the Au nanoclusters for proteins without enough thiol groups based on previous reports on Au surface interactions with various functional groups (thiol > amine > hydroxyl).^{38, 39} Lack of cysteine residues causing blue shifts in fluorescent emissions of protein-Au nanoclusters was also

observed in myoglobin (no cysteine) stabilized Au nanoclusters.⁴⁰ Thiol groups are known to form chemical bonds on Au surfaces; In contrast, amine groups are generally believed to form coordination bonds, where the lone electron pair of nitrogen involving coordination with the empty orbital of Au complex. These two types of bindings led to different ability of providing electrons and thus surface states of Au complex. Our hypothesis of amine-involvement in nanocluster stabilization was further supported by measuring the pIs of the proteins before and after Au nanocluster encapsulation via titration. Before Au nanocluster encapsulation, the pIs of BSA, trypsin and lysozyme were experimentally determined to be 4.5, 7, and 10.5, respectively. After Au nanocluster encapsulation, the pI of BSA remained unchanged, but the pIs of trypsin and lysozyme significantly reduced to 5 and 5.5, respectively. The pI changes in lysozyme and trypsin indicated the involvement of the amine groups during the encapsulation of Au nanoclusters.

To further investigate the effects of ligands on the properties of the Au nanoclusters, the fluorescent lifetimes of all three types of Au nanoclusters were measured with an Edinburgh Photonics Mini-Tau time-resolved fluorimeter using the time-correlated single photon counting technique (TC-SPC). Figure 4.3 shows the fluorescent emission lifetime decays and fit curves, which were fitted with multi-exponential models containing two lifetimes. The two-exponential lifetimes were 765 ns and 1976 ns for lyso-Au nanoclusters, accounting for 23.3% and 76.7% of the integrated fluorescence emission; 766 ns and 2062 ns for Try-Au nanoclusters, accounting for 24.8% and 75.2% of the integrated fluorescence emission; 711 ns and 1871 ns for BSA-Au nanoclusters, accounting for 29.4% and 70.6% of the integrated fluorescence emission. The reduced chi-square values (χ^2) for each fit were: 1.12, 1.16, and 1.06, respectively.

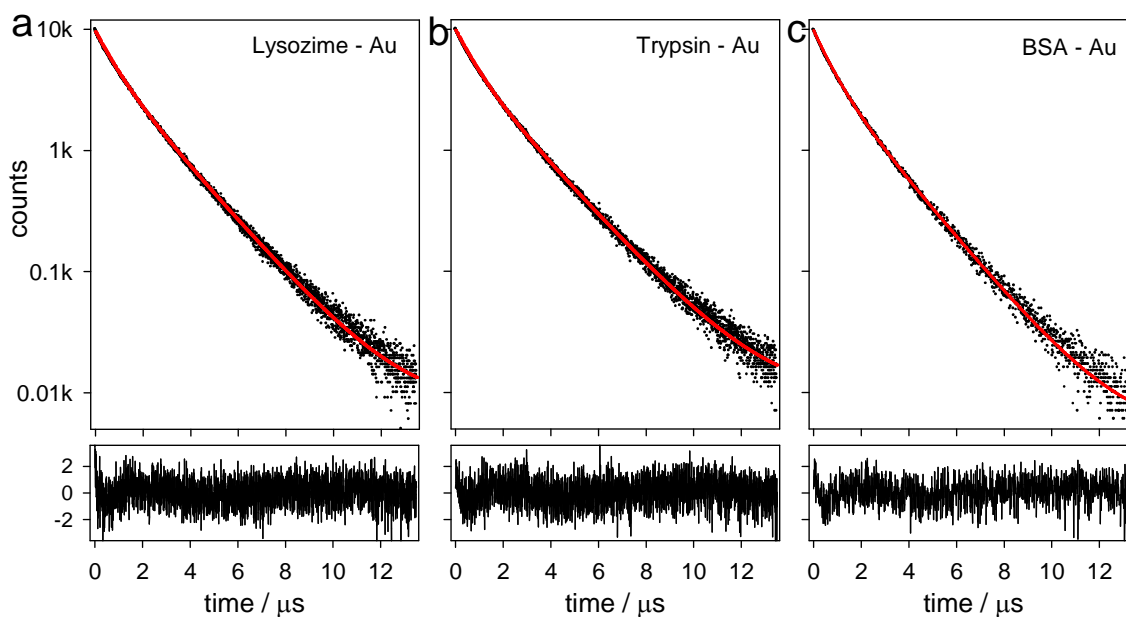


Figure 4.3. Time-resolved fluorescence lifetime analysis of (a) Lyso-Au (b) Try-Au and (c) BSA-Au nanoclusters.

Because multiple exponentials were necessary to fit the lifetime decays, we found it useful to present the intensity-weighted average lifetime τ_{ave} as an overall descriptor of the average time delay with which photon emission occurs after the laser pulse, which led to 1529 ns for BSA-Au, 1741 ns for trypsin-Au, and 1689 ns for lyso-Au. In all cases, the most important contribution to the emission came from the species with the longest lifetime. The study of BSA-Au nanoclusters has attributed the slow component to the triplet formation and the fast component to the trapping of surface Au(I) states.²⁹ The higher percentage of the fast component for BSA-Au (29.4%) than that of try-Au and lyso-Au (23.3% or 24.8%) suggested higher amount of Au(I) surface states from thiol interactions.

When the ratios of the amine functional groups to Au (4:1) were kept the same, the protein-Au nanoclusters showed similar fluorescent emission/excitation behaviours (Figure S4.3a) to the nanoclusters generated with excess proteins (Figure 4.2). When the amine to Au ratios were kept the same, the proteins to Au ratios turned out to be 0.04 to 1 for BSA, 0.2 to 1

for both trypsin and lysozyme. The ratios for trypsin and lysozyme are much higher than that of the proteins needed to stabilize Au nanoclusters, such as 0.13 to 1 for trypsin and 0.18 to 1 for lysozyme. In contrast, when keeping the ratios of tyrosine/tryptophan to Au the same (1:1), the fluorescent emission/ excitation behaviours for BSA-Au nanoclusters did not change, but the fluorescent emission and excitation spectra of trypsin and lysozyme-Au nanoclusters exhibited blue shifts (Figure S4.3b). At the 1 to 1 reducing power to Au ratio, the proteins to Au ratios were 0.04 to 1 for BSA, about 0.06 to 1 for trypsin, and 0.1 to 1 for lysozyme. The ratios of trypsin and lysozyme were lower than the proteins needed to stabilize Au nanoclusters, such as 0.13 to 1 for trypsin and 0.18 to 1 for lysozyme.

It is expected that the encapsulation of the Au nanoclusters inside the protein template interferes with the protein structure. Infrared spectroscopy offers an effective tool to study the secondary structure and the structural change of proteins.⁴¹ In addition, the side chains of some amino acids exhibit characteristic peaks as key marker identification.⁴² The FTIR spectra provide information on the secondary structural change after Au nanocluster encapsulation, because the amide bands are highly sensitive to environmental change, including amide I mainly -C=O stretching ($1600\text{-}1680\text{ cm}^{-1}$),⁴¹ amide II band arising from -N-H bending (60%) and -C-N stretching (40%),⁴³ and amide III, the in phase combination of C-N stretching, C=O in plane bending, and C-C stretching.⁴⁴

Compared to the IR spectra of native proteins (Figure S4.4), the IR spectra of the denatured proteins showed several distinct changes, such as intensity reduction of the amide I and II bands, appearance of IR bands of hydrophobic residues, and peak shifts in the amide III region. For all three proteins, the CH_2 in plane and out plane bending and rocking bands became dominant, including 1422 , 991 , and 877 cm^{-1} for BSA, 1429 and 880 cm^{-1} for trypsin and

lysozyme. The peak shifts in the amide III regions (1129-1301 cm^{-1}) included C-N stretching and N-H bending, such as 1243 to 1278 cm^{-1} for BSA, 1236 to 1278 cm^{-1} for trypsin, and 1236 to 1305 cm^{-1} for lysozyme. Further, each protein also exhibited its specific feature. For instance, BSA showed mainly hydrophobic features with the C-H out-of plane bending at 991 cm^{-1} . In addition to the exposure of hydrophobic residues, the denatured trypsin showed several typical tyrosine residues band shifts, including band 1007 cm^{-1} (phenol-OH) to 1114 cm^{-1} (phenol-O⁻) after denature under basic environment along with the Tyr-O⁻ (C-C stretching) at the 1560 cm^{-1} and Try-O⁻ at 1496 cm^{-1} (CH in plane bending). Tyrosine is a very strong IR absorber, which over dominated the amide II bands. Lysozyme showed typical bands of Tryptophan CH and NH bending of the indole ring at 1506 cm^{-1} and 1004 cm^{-1} along with the out plane mode of indole mode at 740 cm^{-1} .⁴¹

Figure 4.4 shows the IR spectra of denatured proteins and protein-Au nanoclusters. After Au nanocluster encapsulation, all three proteins refolded to some extent with enhanced signals of the amide I and amide II bands. The shifts observed in amide III region shifted back to native states, such as 1287 to 1241 and 1310 cm^{-1} for BSA, 1278 to 1240 cm^{-1} for trypsin, and 1305 to 1278 cm^{-1} for lysozyme. The refold of BSA was also supported by the disappearance of -CH out of plane bending band (991 cm^{-1}). The -CH₂ bending band at 1442 cm^{-1} became a shoulder of the major 1398 cm^{-1} band (Figure 4.4a). In addition to the change in the hydrophobic residues, several IR bands related to -COO⁻ groups appeared, including the asymmetric/symmetric stretching vibration of -COO⁻ groups at 1564 cm^{-1} (overlapped with the amide II band) and 1398 cm^{-1} , COO⁻ scissoring and rocking at 860 cm^{-1} and 830 cm^{-1} ,^{45,46} and -C=O out of plane bending at 780 cm^{-1} .⁴⁷ The spectra change can be easily understood by the large amount of negatively charged residues (99) in BSA and these carboxylic groups were entirely ionized at the reaction

pH 12. In contrast, trypsin protein only has 9 negatively charged residues. Compared to the free protein, the IR spectrum changes suggested the negatively charged residues were either highly exposed or close to the Au nanocluster, which enhanced the IR signal.

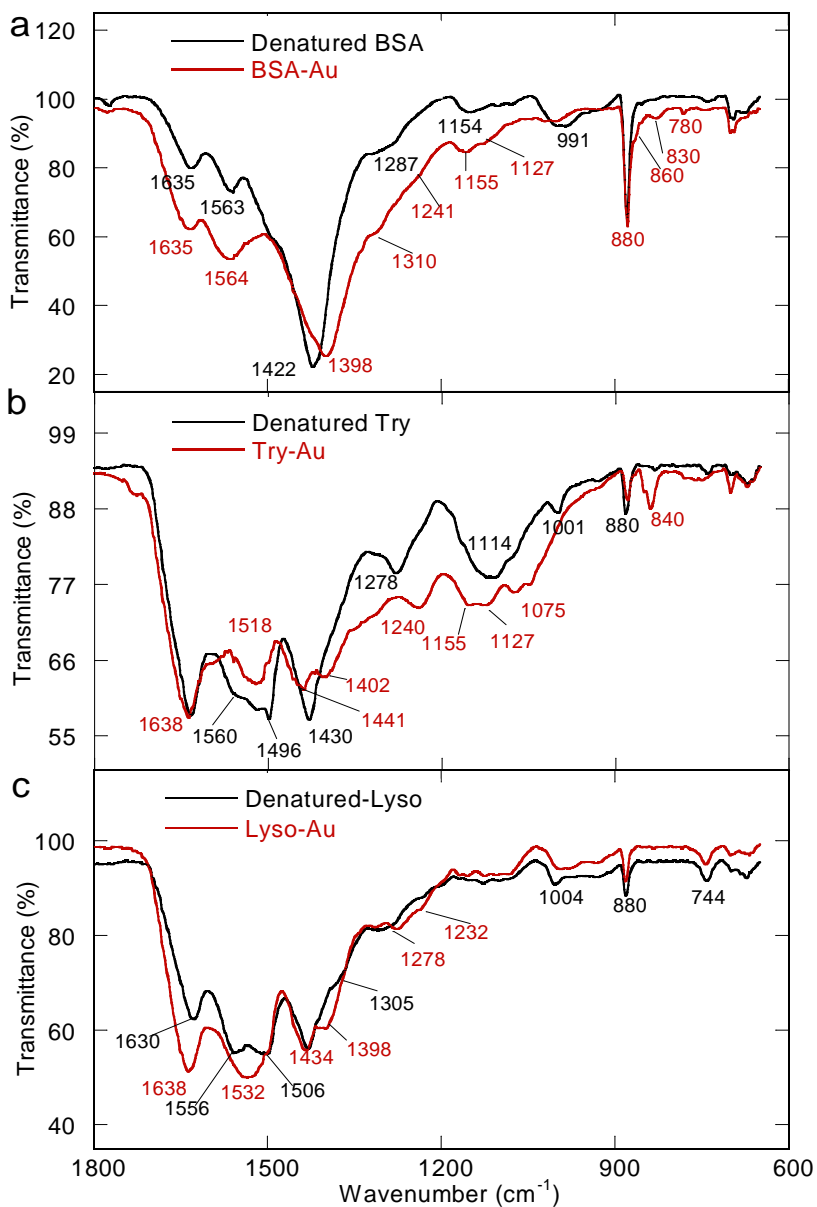


Figure 4.4. FTIR spectra of protein-encapsulated Au nanoclusters and its corresponding free protein under denatured conditions: (a) BSA, (b) trypsin, and (c) lysozyme.

After Au nanocluster encapsulation, the amide I band (1638 cm^{-1}) of trypsin showed little variation, but the Tyr-O⁻ bands at the 1560 cm^{-1} and 1496 cm^{-1} became the characteristic tyrosine band at 1518 cm^{-1} (Figure 4.4b).⁴¹ Interestingly, the side chain bands of tyrosine residues showed a significant band at 840 cm^{-1} , a key marker of tyrosine-tyrosine crosslinker,⁴⁸ which is a result of Au ion and tyrosine reduction/oxidation. The amide I and II bands of lysozyme were much enhanced (Figure 4.4c) after Au nanocluster encapsulation. However, no other significant changes were observed except for the disappearance of indole ring band at 1506 cm^{-1} , and the appearance of a shoulder band at 1398 cm^{-1} .

The stability of fluorescence is a key parameter to the application of Au nanoclusters as tag molecules for sensing, imaging, or detection. The stabilities of the Au nanoclusters (generated from various proteins) were systematically studied in terms of pH effects, buffer environments, photo, thermal, and long-term stability. The chemical, physical, and long-term stabilities of the protein-Au nanoclusters were studied using the nanoclusters produced with excess proteins because of the high fluorescent intensity and enough materials from the same batch for stability studies.

All of the Au nanoclusters were produced under highly basic conditions (pH 12); however, these nanoclusters are generally utilized in physiological conditions. The pH effects were studied by monitoring the fluorescent emissions of the protein-Au nanoclusters at different pHs (12→9→7→5→7→9→12). At each pH value, the solution was equilibrated for 20 minutes before measuring. Figure 5 shows the pH effects on the fluorescent emissions of the protein encapsulated Au nanoclusters. For BSA-Au nanoclusters (Figure 4.5a and b), we observed an approximately 30% reduction in fluorescent intensity and a 15 nm blue shift of the $\lambda_{\text{em, max}}$ from pH 12 to 9. The emission intensity at pH 7 was similar to that at pH 9, but the $\lambda_{\text{em, max}}$ blue

shifted another 10 nm. By pH 5, most of the proteins were precipitated out of the solution because of the pI of the protein and a very low fluorescent signal was detected. The lost fluorescence intensity was recovered after adjusting the pH of the solution (Figure 4.5b). However, the fluorescence intensities were slightly lower because of the dilution during the pH adjustment with HCl and NaOH solutions and the difficulty in re-dissolving the protein precipitates entirely. This pH dependent behaviour of the BSA-Au nanoclusters was related to the structural conformation of BSA protein. BSA remains its native conformation in a pH range of 5-7.5; but it changes into the basic form above pH 8. Continuous pH increase to 12 causes the completely unfold of domain I and III.⁴⁹

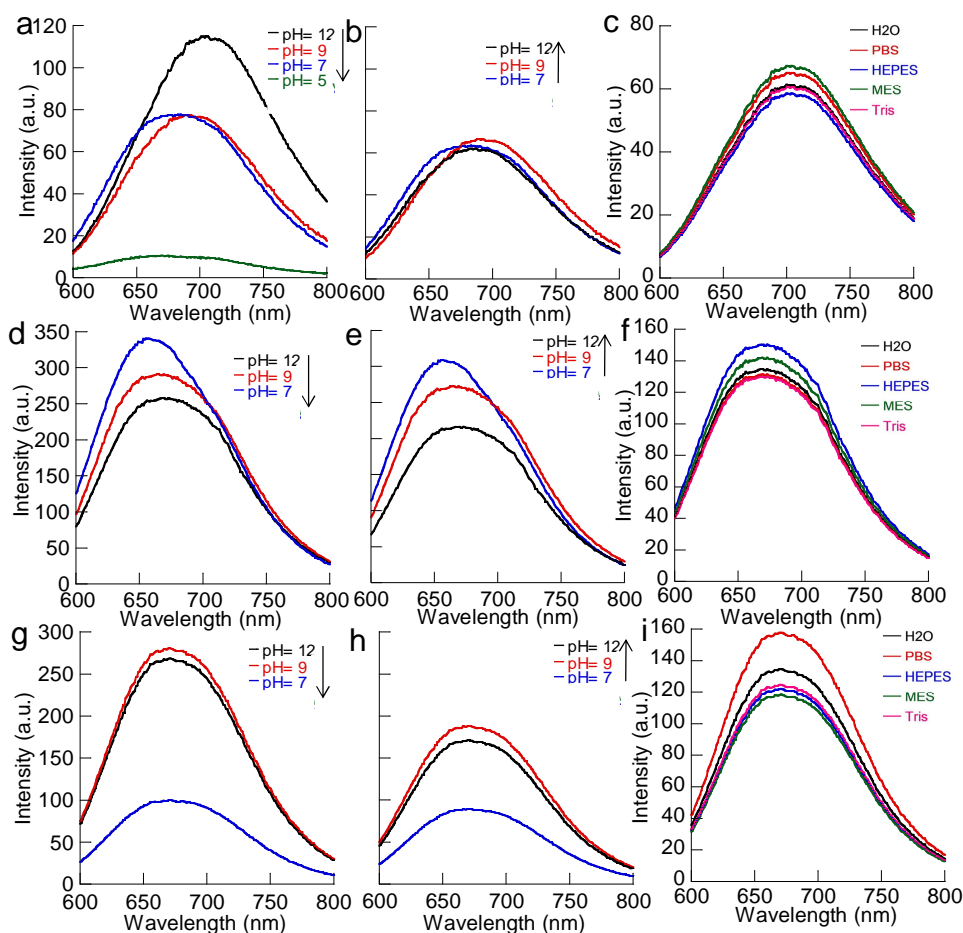


Figure 4.5. pH and buffer condition effects on the fluorescent emission of Au nanoclusters generated by (a-c) BSA, (d-f) trypsin, and (g-i) lysozyme.

For trypsin-Au nanoclusters (Figure 4.5d and e), the highest fluorescent intensity was observed at pH 7 because trypsin has a well ordered conformation between pH 7 and 8, but becomes considerably less ordered at more acidic and more basic pH values.⁵⁰ After going through the pI of the protein, the fluorescent intensities were slightly lower due to dilution of the solution and the difficulty in re-dispersing the aggregates entirely. Compared to the ~ 25 nm blue shift of the $\lambda_{em, max}$ from pH 12 to 7 for BSA-Au nanoclusters, the fluorescent emission of trypsin-Au nanoclusters exhibited ~10 nm blue shift from pH 12 to 7. At pH 5, the protein-Au nanoclusters were precipitated out and no fluorescent spectrum was collected. For lysozyme-Au nanoclusters (Figure 4.5g and h), the $\lambda_{em, max}$ did not shift with pH likely due to the high stability of lysozyme in a wide pH range. The decrease in intensity was mainly due to the precipitation of the lysozyme-Au nanoclusters.

For biological applications, fluorescent nanoclusters are generally applied in biological buffers, therefore, the stability of the Au fluorescent nanoclusters were studied in various buffers, including PBS, MES, Tris, and HEPES. Figure 4.5c, f, and i shows the fluorescent emission plots at various conditions. Compared to emissions of the Au nanoclusters in water at pH 7, dialysis with biological buffers at pH 7 did not affect the fluorescence emission much. However, we did observe a slight intensity variation among these three types of Au nanoclusters. For example, the highest intensities were observed in MES for BSA-Au nanoclusters, HEPES for trypsin-Au nanoclusters and PBS for lysozyme-Au nanoclusters.

Generally, during applications, a laser is applied to excite the nanoclusters. Depending on the duration, the laser can heat up and/or photobleach the tag molecules. The temperature effects on the protein-Au nanoclusters were studied in a cycle (22→37→45→55→45→37→22 °C) by merging the nanocluster solutions in a water bath at pre-set temperatures. After 20 minute

equilibration, the nanocluster solutions were immediately measured. Figure 4.6 shows the fluorescent emission plots of the protein-Au nanoclusters at different temperatures. For all of the three types of Au nanoclusters, the fluorescence intensities decreased as the temperature increased, mainly due to the increased photo collision at higher temperatures. However, the fluorescence was largely recovered once the nanocluster solutions were at lower temperature. In addition to the decrease in fluorescent intensity, the lysozyme-Au nanoclusters also showed an approximately 20 nm red shift likely because of aggregation. However, this aggregation process was reversible, similar to the pH effects.

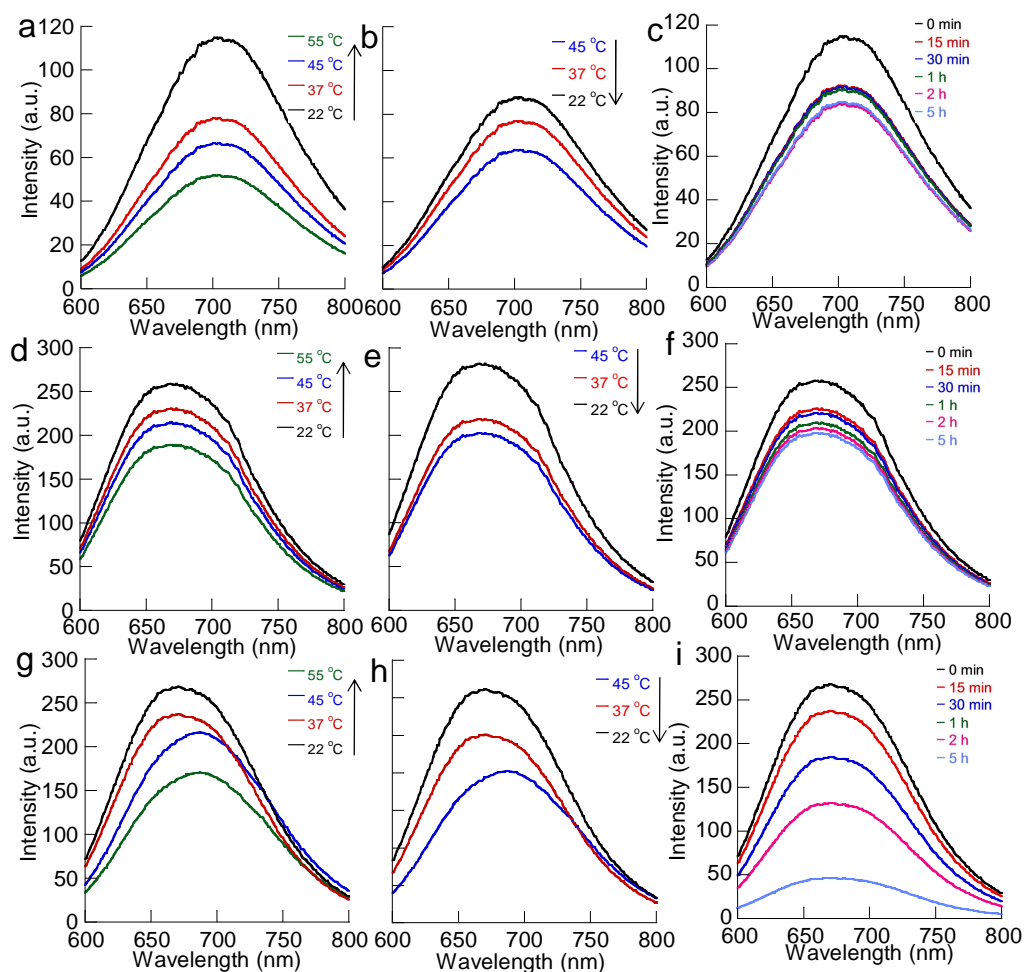


Figure 4.6. Temperature and UV-radiation effects on the fluorescent emission of Au nanoclusters generated by (a-c) BSA, (d-f) trypsin, and (g-i) lysozyme.

The photostability (i.e. the decrease in fluorescent intensity upon light irradiation) of a fluorescent tag determines the duration of a measurement or test. The photostability of the protein-Au nanoclusters were studied under UV light radiation (365 nm, 6 W/cm²) in water at pH 12 (Figure 4.6 c, f and i). The fluorescence intensity of BSA-Au nanoclusters dropped 20% at the first 15 minutes. Then, the Au nanoclusters showed great photo stability with only ~ 5% loss after 5 hour radiation (Figure 4.6c). The great UV stability of BSA-Au nanoclusters can be understood by the large size of the protein template (636 aa) and the formation of the complete surface staple motifs with the involvement of 18 thiol groups. Similar to the BSA-Au nanoclusters, the trypsin-Au nanoclusters exhibited 25% fluorescence drop after 5 h with a quick loss of 15% at the first 15 minutes (Figure 4.6f). Compared to BSA, trypsin has a much smaller size (223 aa) and fewer thiol groups (7) without the formation of a complete coverage of surface staple motifs. The fluorescent intensity of lysozyme-Au nanoclusters dropped approximately 60% after 1 h and 80% after 5 hours. The lysozyme has similar thiol content to trypsin, but with a much smaller size (129 aa) (Figure 4.6i). Therefore, we concluded that protein size was the main factor contributing to the photostability of the protein-encapsulated nanoclusters, not the $-S-Au(I)-S-Au(I)-S-$ staple surface motifs.

The long-term stability of the Au nanoclusters was studied in powder and solution form for each protein. The Au nanoclusters generated from all three proteins showed higher stability in powder form than that in solution (Figure S4.5). For example, at 4 °C, the BSA-Au nanoclusters stored in powder form retained 96% of the fluorescent intensity after one year, while the fluorescence intensity of the same sample in solution reduced to 75% after one month. Similar trends were observed for the trypsin-Au nanoclusters (92% in powder and 80% in solution) and lysozyme-Au nanoclusters (90% in powder and 75% in solution) after one month.

Except for the fluorescent intensity, the $\lambda_{em, max}$ of BSA-Au nanoclusters showed no shift. In contrast, trypsin-Au nanoclusters showed no change in powder form, but with a red shift in $\lambda_{em, max}$ in solution, an indication of aggregation. The aggregation in solution was likely because the proteins were subject to protease in solution. The lysozyme-Au nanoclusters showed red shifts in both powder and solution form. This observation suggested that the protein size is a key parameter for long-term stability.

To understand the immobilization effect, protein-encapsulated Au nanoclusters were covalently conjugated onto iron oxide nanoparticle surfaces using our previously reported procedure (Figure 4.7).²⁸ Because of the extremely small sizes of the Au nanoclusters, they were barely seen on the iron oxide nanoparticles. However, small darker spots on the nanoparticle surfaces could be observed via carefully examination. After immobilization, the $\lambda_{em, max}$ of the BSA-Au nanoclusters blue shifted about 25 nm and maximum excitation blue shifted about 10 nm. The blue shifts were likely resulted from conformational change of BSA protein, which altered the local environment of the Au nanoclusters. BSA is known to have several dynamic conformations. After immobilization on the nanoparticle surfaces, the dynamic conformation of BSA was significantly reduced. In contrast to BSA-Au nanoclusters, both trypsin-Au and lysozyme-Au nanoclusters showed much broader fluorescent emission and excitation peaks after immobilization. The fluorescent emission peaks were blue shifted while the fluorescent excitation peaks were red shifted. We attributed these changes to the involvement of iron oxide nanoparticles during excitation and emission, because iron oxide nanoparticles have strong absorption in the visible range. This effect could only take place when the nanoclusters were close to the surface of iron oxide nanoparticles. The size of BSA protein is much larger than that of trypsin and lysozyme, and showed only minimal effects from the iron oxide nanoparticles.

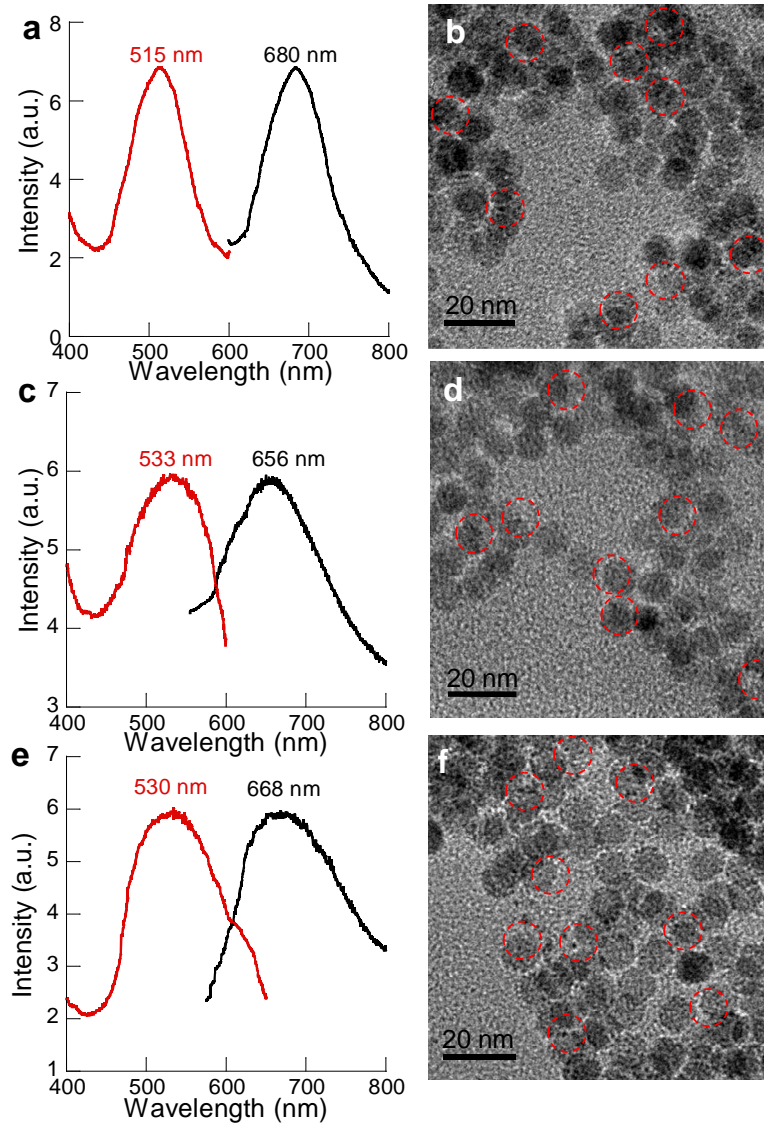


Figure 4.7. Protein-Au nanoclusters immobilized on iron oxide nanoparticle surface: fluorescent emission/excitation plots and TEM images of BSA (a and b), trypsin (c and d), and lysozyme (e and f).

To verify our hypothesis, we conducted experiments by simply mixing the Au nanocluster solutions with iron oxide nanoparticles and then measured the fluorescent emission and excitation before and after the addition of iron oxide nanoparticles. Figure S4.6 showed the fluorescent excitation/emission plots of protein-Au nanoclusters before and after the addition of iron oxide nanoparticles. For all these samples, significant intensity decrease was observed due to the strong absorption of iron oxide nanoparticles in visible range, but the emission peak (λ_{em} ,

max) was not affected. In contrast, the excitation peak red shifted. This observation was mainly because the iron oxide nanoparticles have absorption in the visible range, which interfered with the excitation but not the emission. Compare the spectra of the simply mixed and the immobilized nanocluster samples, the immobilization effects on the Au nanoclusters can be clearly identified.

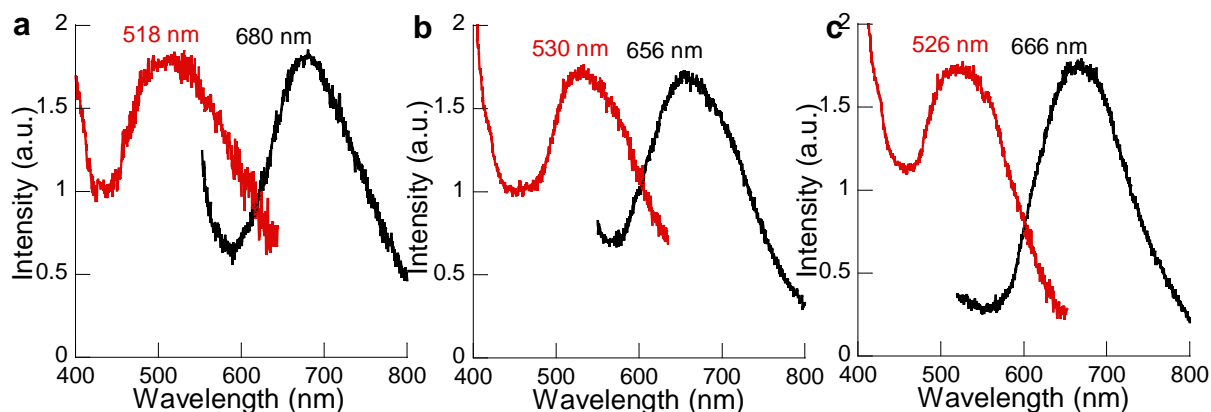


Figure 4.8. The fluorescent emission/excitation plots of protein-Au nanoclusters immobilized on the inner surface of glass vials: (a) BSA, (b) trypsin, and (c) lysozyme.

Alternatively, the protein-Au nanoclusters were immobilized on the inner surface of glass vials. Figure 4.8 shows the fluorescent emission/excitation plots of the immobilized Au nanoclusters immersed in water. Similar emission and excitation shifts were observed for both immobilizations experiments. Therefore, we believe that the protein dynamic were primarily responsible for changes in the fluorescence.

4.4 Conclusions

In summary, the effects of protein size and amino acid sequence on the protein-encapsulated Au nanoclusters were studied systematically. The experimental results suggested that a balance of the amine-containing and tyrosine/tryptophan residues was critical for the formation and stabilization of the Au nanoclusters. For example, pepsin with a few amine-

containing residues but much higher amount of tyrosine/tryptophan was not able to produce Au nanoclusters, leading to the formation of larger size Au nanoparticles. In addition, the cysteine content is critical to form surface staple residue and fluorescent emission. Lower cysteine content (< 18 per protein) caused blue shifts of the emission spectra and difference in fluorescent lifetimes due to the possible contribution from amine-containing residues in the stabilization of the Au nanoclusters. Furthermore, the size of the protein template was found to be critical to the photo, thermal, and chemical stability of the Au nanoclusters. Finally, regardless of the size of the protein, immobilization effects were observed for all three types of Au nanoclusters.

Acknowledgments

This work is supported by NSF-DMR 0907204 and DMR1149931. We acknowledge the UA Central Analytical Facility (CAF) and the Biological Science Department for the use of TEM. We also acknowledge the highly useful discussion with Professor Jin Zhang (University of California-Santa Cruz).

4.5 References

1. Makarava N, Parfenov A, and Baskakov IV. *Biophys. J.* **2005**, *89*, 572-580.
2. Triulzi RC, Micic M, Giordani S, Serry M, Chiou WA, and Leblanc RM, *Chem. Commun.* **2006**, *48*, 5068-5070.
3. Slocik JM, Moore JT, and Wright DW, *Nano Lett.* **2002**, *2*, 169-173.
4. Zheng J, Nicovich PR, and Dickson RM, *Annu. Rev. Phys. Chem.* **2007**, *58*, 409-431.
5. Link S, Beeby A, FitzGerald S, El-Sayed MA, Schaaff TG, and Whetten RL, *J. Phys. Chem. B* **2002**, *106*, 3410-3415.
6. Bigioni TP, Whetten RL, and Dag O. *J. Phys. Chem. B* **2000**, *104*, 6983-6986.
7. Varnavski O, Ispasoiu RG, Balogh L, Tomalia D, and Goodson T. *J. Chem. Phys.* **2001**, *114*, 1962-1965.
8. Bao Y, Zhong C, Vu DM, Temirov JP, Dyer RB, and Martinez JS. *J. Phys. Chem. C* **2007**, *111*, 12194-12198.
9. Negishi Y, and Tsukuda T. *Chem. Phys. Lett.* **2004**, *383*, 161-165.
10. Bao Y, Yeh HC, Zhong C, Ivanov SA, Sharma JK, Neidig ML, Vu DM, Shreve AP, Dyer RB, Werner JH, and Martinez JS, *J. Phys. Chem. C* **2010**, *114*, 15879-15882.
11. An W, Wintzinger L, Turner CH, and Bao Y, *Nano-Life* **2010**, *1*, 133-143.
12. Liu G, Shao Y, Wu F, Xu S, Peng J, and Liu L. *Nanotechnol.* **2013**, *24*, 015503.
13. Liu G, Shao Y, Ma K, Cui Q, Wu F, and Xu S. *Gold Bull.* **2012**, *45*, 69-74.
14. Kennedy TAC, MacLean JL, and Liu J. *Chem. Comm.* **2012**, *48*, 6845-6847.
15. Chevrier DM, Chatt A, and Zhang P. *J. Nanophoton* **2012**, *6*, 064504(13).
16. Xie J, Zheng Y, and Ying J. *J. Am. Chem. Soc.* **2009**, *131*, 888-889.
17. Guevel XL, Hotzer B, Jung G, Hollemeyer K, Trouillet V, and Schneider M. *J. Phys. Chem. C* **2011**, *115*, 10955-10963.
18. Yue Y, Liu T, Li H, Liu Z, and Wu Y. *Nanoscale* **2012**, *4*, 2251-2254.
19. Wei H, Wang Z, Yang L, Tian S, Hou C, and Lu Y. *Analyst* **2010**, *135*, 1406-1410.
20. Chen T, and Tseng W. *Small* **2012**, *8*, 1912-1919.
21. Guevel XL, Daum N, and Schneider M. *Nanotechnol.* **2011**, *22*, 275103.
22. Xavier PL, Chaudhari K, Verma PK, Pal SK, and Pradeep T. *Nanoscale* **2010**, *2*, 2769-2776.

23. Chaudhari K, Xavier PL, and Pradeep T. *ACS Nano* **2011**, *5*, 8816-8827.
24. Kawasaki H, Yoshimura K, Hamaguchi K, and Arakawa R. *Anal. Sci.* **2011**, *27*, 591-596.
25. Kawasaki H, Hamaguchi K, Osaka I, and Arakawa R. *Adv. Funct. Mater.* **2011**, *21*, 3508-3515.
26. Liu C, Wu H, Hsiao Y, Lai C, Shih C, Peng Y, Tang K, Chang H, Chien Y, Hsiao J, Cheng J, and Chou P. *Angew. Chem. Int. Ed.* **2011**, *50*, 7056-7060.
27. Wen F, Dong Y, Feng L, Wang S, Zhang S, and Zhang X. *Anal. Chem.* **2011**, *83*, 1193-1196.
28. Xu Y, Palchoudhury S, Qin Y, Macher T, and Bao Y. *Langmuir* **2012**, *28*, 8767-8772.
29. Wen X, Yu P, Toh YR, Hsu AC, Lee YC, and Tang J. *J. Phys. Chem. C* **2012**, *116*, 19032-19038.
30. Wen X, Yu P, Toh YR, Hsu AC, Lee YC, and Tang J. *J. Phys. Chem. C* **2012**, *116*, 11830-11836.
31. Cao X, Li H, Yue Y, and Wu Y. *Vib. Spectrosc.* **2013**, *65*, 186-192.
32. Xiang D, Zeng G, Zhai K, Li L, and He Z. *Anal.* **2011**, *136*, 2837-2844.
33. Luo Z, Yuan X, Yu Y, Zhang Q, Leong DT, Lee JY, and Xie J. *J. Am. Chem. Soc.* **2012**, *134*, 16662-16670.
34. Shang L, Brandholt S, Stockmar F, Trouillet V, Bruns M, and Nienhaus GU, *Small* **2012**, *8*, 661-665.
35. Xu Y, Qin Y, Palchoudhury S, and Bao Y, *Langmuir* **2011**, *27*, 8990-8997.
36. Palchoudhury S, Xu Y, Goodwin J, and Bao Y. *J. Mater. Chem.* **2011**, *21*, 3966-3970.
37. Palchoudhury S, Xu Y, Goodwin J, and Bao Y. *J. Appl. Phys.* **2011**, *109*, 07E314.
38. Zhu X, Yang Q, Huang J, Suzuki I, and Li G. *J. Nanosci. Nanotechnol.* **2008**, *8*, 353-357.
39. Polavarapu L, and Xu Q. *Nanotechnol.* **2008**, *19*, 075601.
40. Volden S, Lystvet SM, Halskau O, and Glomm WR. *RSC Adv.* **2012**, *2*, 11704-11711.
41. Barth A. *Biochim. Biophys. Acta-Bioenerg.* **2007**, *1767*, 1073-1101.
42. Barth A. *Prog. Biophys. Mol. Bio.* **2000**, *74*, 141-173.
43. Jackson, M, and Mantsch, HH. *Crit. Rev. Biochem. Mol.* **1995**, *30*, 95-120.
44. Anderle G, and Mendelsohn, R. *Biophys. J.* **1987**, *52*, 69-74.
45. Rehman I, Movasaghi Z, and Rehman S. *Vibrational Spectroscopy for Tissue Analysis*. CRC press. Taylor & Francis Group: **2013**; p 356.

46. Navarrete JTL, Hernandez V, and Ramirez FJ. *J.Mol. Struct.* **1995**, 348, 249-252.
47. Rudbeck ME, Kumar S, Mroginski MA, Lill SON, Blomberg MRA, and Barth A. *J. Phys. Chem. A* **2009**, 113, 2935-2942.
48. Anderson KD, Slocik JM, McConney ME, Enlow JO, Jakubiak R, Bunning TJ, Naik RR, and Tsukruk VV. *Small* **2009**, 5, 741-749.
49. Ahmad B, Kamal MZ, and Khan RH. *Protein Pept. Lett.* **2004**, 11, 307-315.
50. Simon ML, László K, Kotormán M, and Szajáni B. *Acta Biol. Szeged.* **2001**, 45, 43-49.

4.6 Supporting information

Figure S1 shows the UV-visible absorption spectra of Au nanoclusters from trypsin and lysozyme, where the protein to Au ratio was kept the same. Even though larger sized clusters were observed from the transmission electron microscopy images (Figure 4.1d and f), the typical 520 nm absorption of large Au nanoparticles was barely seen.

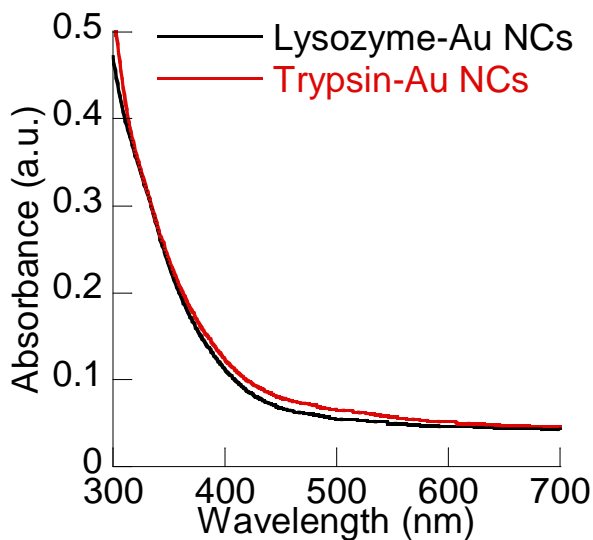


Figure S4.1. UV-vis spectra of protein-Au nanoclusters generated from trypsin and lysozyme.

Figure S4.2 shows the UV-visible absorption spectra of Au nanoclusters from pepsin, where the protein to Au ratio was kept 0.04 to 1, the same as other proteins. The typical 520 nm absorption band of Au nanoparticles was clearly observed, indicating the formation of large Au nanoparticles. This observation was also consistent with dark red color (Figure S4.2b) and the loss of fluorescence of the pepsin-Au solution.

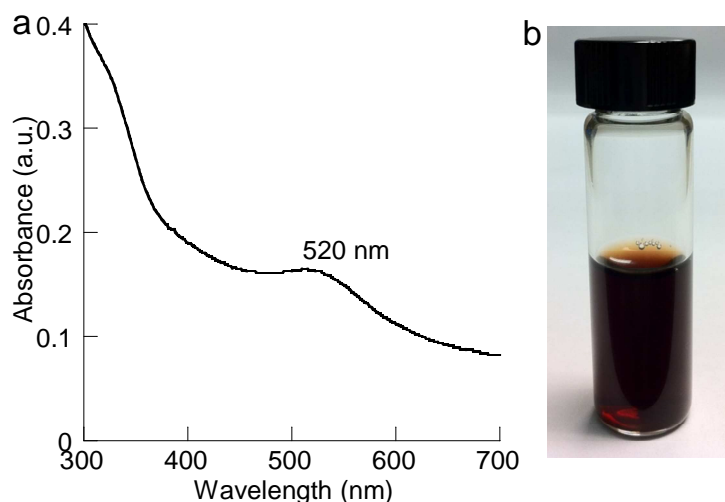


Figure S4.2. (a) a UV-visible spectrum of pepsin-Au nanostructures, (b) a photo image of pepsin-Au nanoparticles in solution.

Figure S4.3 shows the fluorescent emission/excitation plots of Au nanoclusters generated using the same ratios of amine to Au and trypsin/tryptophan to Au. When the amine functional groups and Au ratios (4:1) were kept the same, the protein-Au nanoclusters showed exact the same fluorescent emission and excitation behaviors as the nanoclusters generated with excess proteins shown in Figure 4.2. When the amine to Au ratios were kept the same, the proteins to Au ratios turned out to be 0.04 to 1 for BSA, 0.2 to 1 for both trypsin and lysozyme. The ratios for trypsin and lysozyme are much higher than that of the proteins needed to stabilize Au nanoclusters, such as 0.13 to 1 for trypsin and 0.18 to 1 for lysozyme. In contrast, when keeping the ratios of tyrosine/tryptophan, the reducing power, to Au the same (1:1), we observed the same fluorescent emission and excitation behaviors for BSA protein, but both the fluorescent emission/excitation spectra of trypsin and lysozyme-Au nanoclusters exhibited blue shifts, as shown in Figure S4.4. This observation was mainly because the lower contents of amine groups in trypsin and lysozyme. At the 1 to 1 reducing power to Au ratio, the proteins to Au ratios were 0.04 to 1 for BSA, about 0.06 to 1 for trypsin, and 0.1 to 1 for lysozyme. The ratios of trypsin and lysozyme were lower than the proteins needed to stabilize Au nanoclusters, such as 0.13 to 1 for

trypsin and 0.18 to 1 for lysozyme. Therefore a larger blue shift than the excess protein reactions but smaller blue shift than that with the same protein to Au ratios.

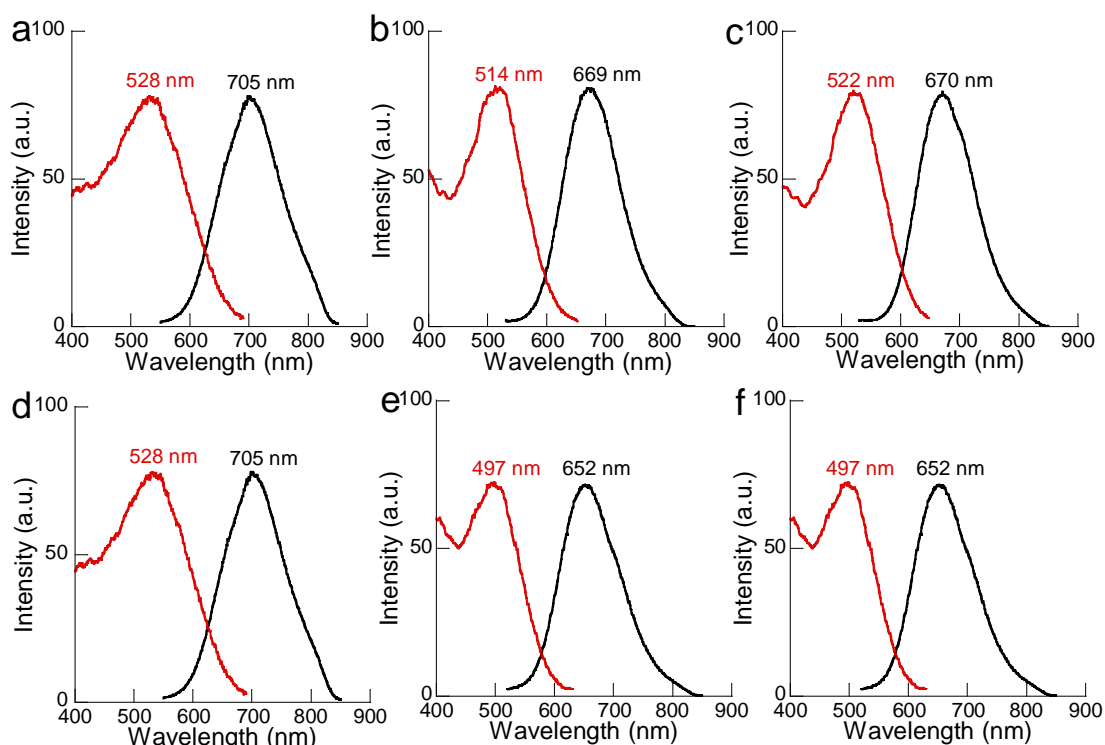


Figure S4.3. Fluorescent emission and excitation plots of protein –Au nanoclusters generated with the same amine group to Au ratios: (a) BSA, (b) trypsin, and (c) lysozyme; and protein-Au nanoclusters generated with the same tyrosine/tryptophan to Au ratios: (d) BSA, (e) trypsin, and (f) lysozyme.

Compared with the IR spectra of native proteins, the IR spectra of the denatured proteins mainly showed signal reduction in the amide I and amide II bands. Evident signals of hydrophobic chains also appeared, such as $-\text{CH}_2$ bending and rocking bands at 1422 and 877 cm^{-1} for BSA and 1429 and 880 cm^{-1} for trypsin and lysozyme. Another notable feature was the band shift in amide III regions (1129 - 1301 cm^{-1}) including $-\text{C}-\text{N}$ stretching and $\text{N}-\text{H}$ bending, such as 1243 to 1308 cm^{-1} for BSA, 1236 to 1278 cm^{-1} for trypsin, and 1236 to 1305 cm^{-1} for lysozyme. Compared to BSA and lysozyme, the IR spectrum of the native trypsin showed the signature

peak of tyrosine at 1515 cm^{-1} and a clear shift from 1007 cm^{-1} (phenol-OH) to 1114 cm^{-1} (phenol-O⁻) after denature under basic environment along with the Tyr-O⁻ (stretching vibration of -C-C) at the 1559 cm^{-1} and Try-O⁻ (-C-H in plane bending) at 1496 cm^{-1} . In contrast, lysozyme exhibited the CH and NH bending of the indole ring at 1506 cm^{-1} along with the out plane mode of indole mode at 740 cm^{-1} .

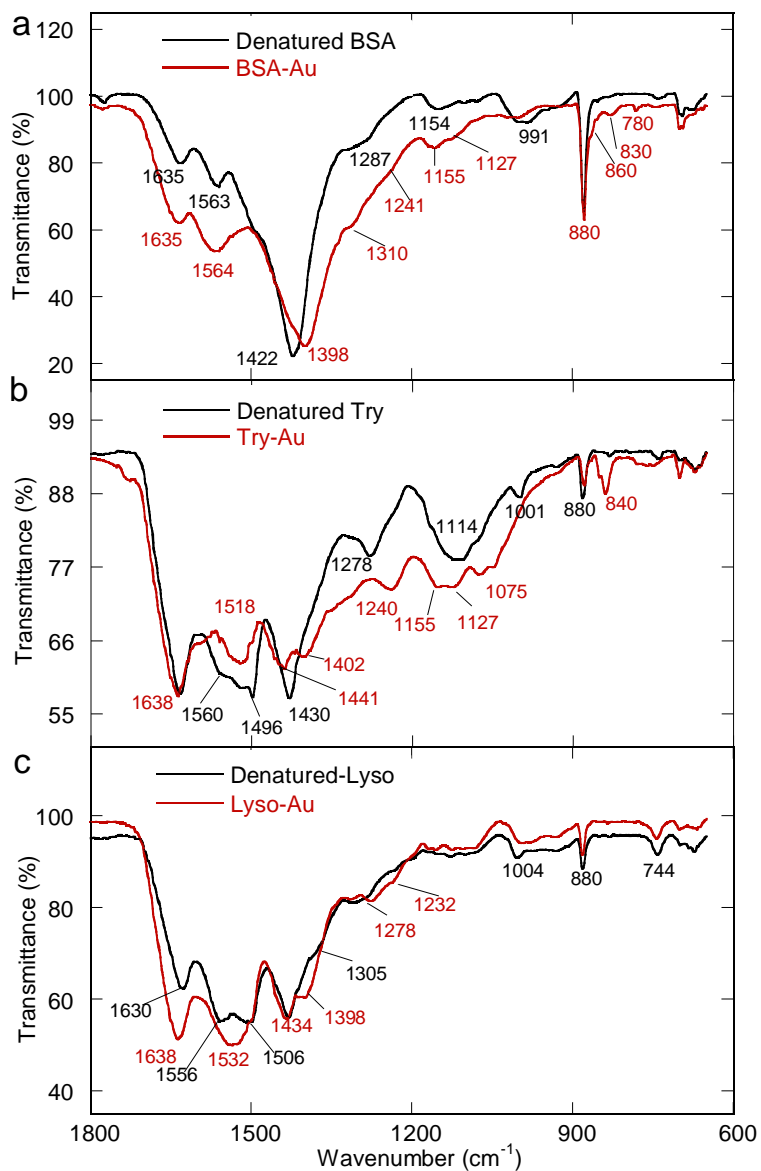


Figure S4.4. FTIR spectra of proteins and denatured proteins in basic environments: (a) BSA, (b) trypsin, and (c) lysozyme.

The long-term stability of the Au nanoclusters was studied in powder and solution forms. The Au nanoclusters generated from all of the three proteins showed a higher stability in powder form than that in solution. In addition, the protein size is important to the stability of the nanoclusters. BSA encapsulated Au nanoclusters showed great stability in both solution and powder forms; The trypsin-Au nanoclusters was stable in powder form, but some aggregation was observed in solution suggested by the red shift of the fluorescent emission; in contrast, the smallest protein, lysozyme encapsulated Au nanoclusters showed red shift in both powder and solution formed samples (Figure S4.5).

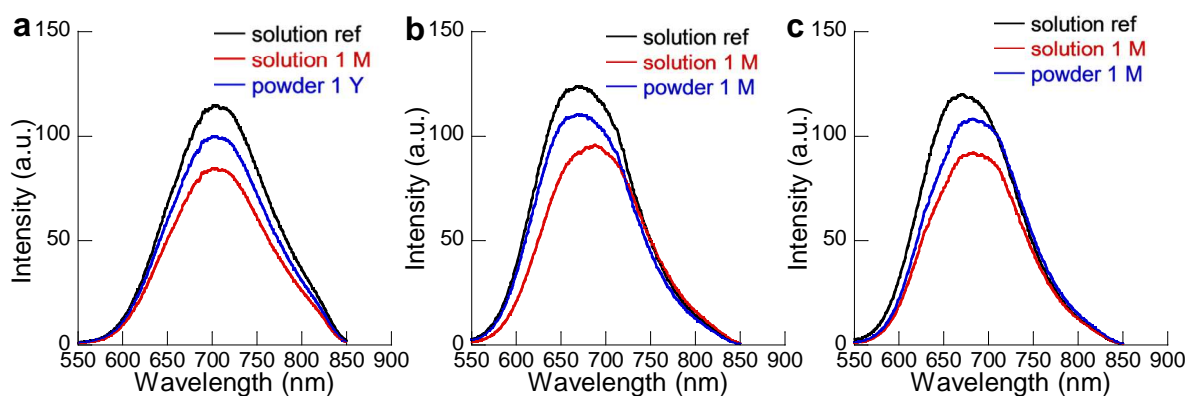


Figure S4.5. Fluorescent emission plots of protein-Au nanoclusters in solution and powder forms (a) BSA-Au nanoclusters, (b) trypsin-Au nanoclusters, and (c) lysozyme-Au nanoclusters.

Figure S4.6 shows the fluorescent excitation/emission plots of protein-Au nanoclusters before and after the addition of iron oxide nanoparticles. For all these samples, significant intensity decrease was observed due to the absorption of iron oxide nanoparticles, but the emission peak ($\lambda_{em, max}$) was not affected. In contrast, the excitation peak was red shift. This observation was mainly because the iron oxide nanoparticles have absorption in the visible range, which interfered with the excitation but not the emission.

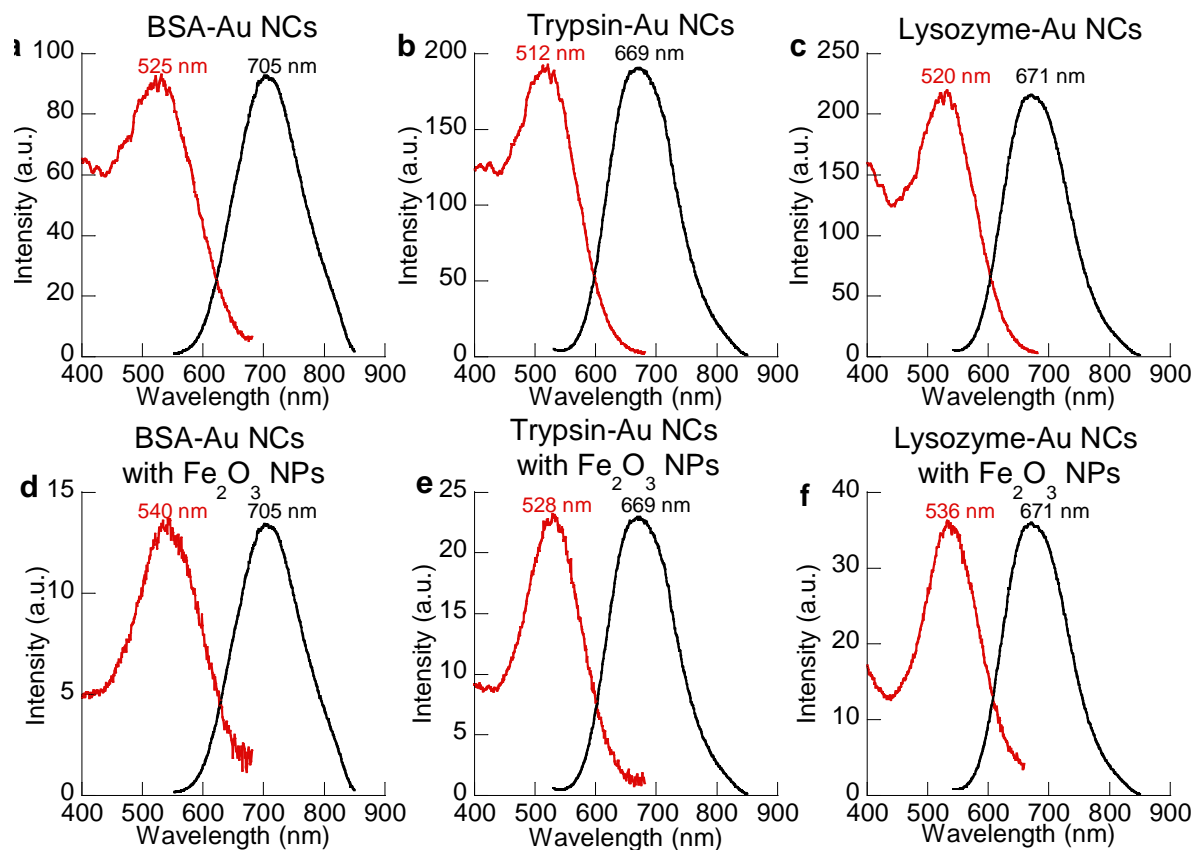


Figure S4.6. Fluorescent emission/excitation plots of Au nanoclusters before and after addition of iron oxide nanoparticles: (a and d) BSA-Au nanoclusters, (b and e) trypsin-Au nanoclusters, and (c and f) lysozyme-Au nanoclusters.

CHAPTER 5

A LINKER-FREE METHOD FOR THE EFFECTIVE CONJUGATION OF BIOACTIVE MOIETIES ONTO IRON OXIDE NANOPARTICLES

(Submitted to *Biomaterials* and under review)

Yaolin Xu, Dana C. Baiu, Jennifer Sherwood, Meghan R. McElreath, Ying Qin, Kimberly H. Lackey, Mario Otto,^{*} and Yuping Bao^{*}

ABSTRACT

Specific targeting is a key step to realize the full potential of iron oxide nanoparticles in nanomedicine. Facile and effective conjugation of the targeting molecules onto iron oxide nanoparticle surface is critically important. Here, we report an easy, linker-free method based on catechol reactions to attach antibodies to iron oxide nanoparticle surfaces for specific cell targeting. The antibody-conjugated nanoparticles exhibited highly selective targeting on GD2-positive neuroblastoma cells, compared with GD2-negative control cells. The specific cell targeting was examined by flow cytometry, fluorescence microscopy, Prussian blue staining and transmission electron microscopy. These detailed studies indicated that antibody-conjugated nanoparticles were quickly recognized by GD2-positive cells at four hours, and the cell membrane bound nanoparticles were subsequently internalized into cytosol at 12 hours, either by directly penetrating the cell membrane or escaping from the endosomes. The uniquely designed functional surfaces of the nanoparticles allow easy conjugation of bioactive molecules onto iron oxide nanoparticles without the need for any type of chemical linkers and maintain the activity of

the attached molecules. Eliminating the use of chemical linkers significantly simplifies the conjugation process, reduces the requirements of well-trained personnel, and increases the efficiency of the conjugation. Importantly, this conjugation method can be effectively extended to other molecules.

KEYWORDS

Iron oxide nanoparticles, Functional surfaces, Antibody conjugation, Neuroblastoma cell targeting, Antibody-conjugated nanoparticles, Tumor-targeting nanoparticles.

5.1 Introduction

Iron oxide nanoparticles are being actively explored in drug delivery^{1,2}, cancer therapy via magnetic hyperthermia³, and diagnostic imaging⁴. In particular, these nanoparticles have been clinically used as contrast agents for magnetic resonance imaging (MRI)⁵, suggesting their great potential in nanomedicine. A significant challenge of using nanoparticles for in vivo diagnostic or therapeutic applications is the delivery efficiency to targeted locations. In fact, several Food and Drug Administration (FDA) approved MRI contrast agents were taken off the market due to lack of clinical use, owing to the fact that these nanoparticles could only passively accumulate in the liver or spleen because of the lack of targeting moieties and surface modifications protecting them from non-specific uptake^{6,7}. To fully realize the potential of iron oxide nanoparticles in nanomedicine, a key step is to effectively attach targeting, therapeutic, or other functional molecules onto the nanoparticle surface to increase the targeting efficiency, broadening the applicability and minimizing the administration dose. Therefore, it is essential to develop a highly efficient, facile, and versatile approach to attaching desired molecules onto iron oxide nanoparticle surfaces.

Among the various targeting molecules, antibody and antibody fragments are some of the most promising moieties for targeted cancer therapy, because of the high affinity and molecular specificity for an antigenic target. The GD2 disialoganglioside is an antigen expressed on neuroblastoma cancer cells, most melanomas and a large fraction of small cell lung cancers and other tumors of neuroectodermal origin^{8,9}. Since GD2 expression on healthy tissue is restricted to the cerebellum and certain peripheral nerve tissue at very low levels¹⁰, it has been considered a very attractive antibody target for neuroblastoma. Hu14.18MoAb (hu14.18-K322A) is a humanized anti-GD2 antibody currently being investigated in a phase-I immunotherapy study in

neuroblastoma patients at St. Jude Children's Research Hospital, Memphis, TN.^{11, 12} This antibody was utilized as a model system to test the conjugation approach.

Several approaches have been applied to conjugate antibodies or other molecules onto iron oxide nanoparticle surfaces¹³⁻¹⁸. The most common approach is the linker chemistry, where chemical linkers cross-link nanoparticles and conjugating molecules^{19, 20}. Even though a number of chemical linkers are available, the entire chemical linker approach suffers from a number of disadvantages. First, special reaction conditions must be met depending on the chemical linker, such as acidic condition (pH 4.5-5.5) for carbodiimide (EDC) chemical linker, pH 7.2-8.0 at 4 °C for N-hydroxysuccinimide (NHS) ester crosslinker, and reducing condition for maleimide chemistry. Second, low conjugation efficiency is always a concern because of competing reactions. For example, the EDC/NHS linker directly links carboxylic and amino groups, for conjugating molecules with multiple carboxylic and amino groups (e.g., proteins). EDC/NHS chemistry causes cross conjugation, thus greatly decreasing the conjugation efficiency^{21, 22}. Finally, multiple cleaning steps are necessary to remove the excess chemical linkers and other assisting reagents.

Besides the chemical linker chemistry, specific molecular recognition based on biotin-streptavidin is another common strategy²³. The biotin-avidin interaction requires prior attachment of biotin molecules onto nanoparticles. The biotin-labeled nanoparticles react with any biotin-binding protein, reducing the specificity. In addition, biotin is a natural biological molecule, causing concerns about the specificity and background when performing assays involving biotin-rich tissues and extracts (e.g., brain, liver, milk, or eggs)²⁴.

In this paper, we developed a facile conjugation approach to attach proteins onto iron oxide nanoparticle surfaces based on catechol reactions. This conjugation approach was

evaluated using a clinically relevant antibody as a model system. Specifically, iron oxide nanoparticles were functionalized with dopamine molecules through amino group attachment, leaving the catechol groups on the nanoparticle surfaces for further conjugation. Upon activation at basic conditions, the catechol groups can be oxidized into quinone and subsequently react with amino or thiol groups of proteins, such as antibodies. After conjugation, the targeting efficiency of the antibodies on nanoparticles was evaluated on GD2-positive neuroblastoma cells. The uniquely designed functional surfaces of the nanoparticles will allow effective conjugation of biological molecules without the need for any type of chemical linkers. Eliminating the use of chemical linkers significantly simplifies the conjugation process, potentially avoids interactions with the biological activity of the targeting moiety, increases the efficiency of the conjugation and last but not least reduces the requirements of well-trained personnel. The method described herein for antibody conjugation to iron oxide nanoparticles can be readily extended to the conjugation of other biological molecules with iron oxide nanoparticles.

5.2 Materials and methods

5.2.1 Materials

All the chemical reagents were commercially purchased and used without further purification. These reagents include(FeCl_3 , ACROS, 98 %), sodium oleate (TCL, 95 %), oleic acid (OA, Fisher, 95 %), trioctylphosphine oxide (TOPO, 90%), 1-octadecene (Sigma-Aldrich, 90 %), chloroform (Sigma-Aldrich, 99%), dimethyl sulfoxide (DMSO, VWR, 99 %), Bis-Tris ($\text{C}_8\text{H}_{19}\text{O}_5\text{N}$, Fisher, enzyme grade), sodium chloride (NaCl , ACROS, 99+%), and Hu 14.18 MoAb (in PBS, 100 mM Arginine, 0.03 % Tween-80). Trypsin-versene mixture (0.05%, Lonza), fetal bovine serum (FBS, Thermo Scientific), Iscove's Modified Dulbecco's Media (IMDM) and Eagle's minimal essential medium (EMEM) were purchased from ATCC. Poly-1-

lysine (Mw: 150,000-300,000 g/mol, Sigma-Aldrich, 0.1% w/v in water), paraformaldehyde (Alfa Aesar, 97%), and Prussian blue iron stain kit (Polysciences, Inc.) (Solution A: Potassium ferrocyanide aqueous ($C_6N_6FeK_4$, 4%), Solution B: Hydrochloric acid (HCl, 4%), Solution C: Nuclear fast red aqueous ($C_{14}H_8NNaO_7S$, 1%) were also used.

5.2.2 Nanoparticle synthesis

Iron oxide nanoparticles were produced by heating up the iron oleate precursor (2.5 g, 2.8 mmol) in 1-octadecene (10 mL, 90%) in the presence of TOPO (90%)/OA (97%) (TOPO-0.2 g, 0.5 mmol, OA-0.22 mL, 0.7 mmol) following our previously published procedures²⁵⁻²⁷. After two and half hour reaction at 320 °C, the nanoparticles were washed and collected for surface modification. The morphology and size of the iron oxide nanoparticles were examined under transmission electron microscopy (TEM, FEI Tecnai, F-20, and 200 kV).

5.2.3 Surface modification

The iron oxide nanoparticles were functionalized with dopamine through a similar procedure used to attach charged polymers onto iron oxide nanoparticle surfaces²⁷. In brief, 1 mL of iron oxide nanoparticles in chloroform (5 mg/mL) was mixed with dopamine-HCl (1.7 mg) in 49 mL of DMSO. After 48 h mixing at room temperature, the iron oxide nanoparticles were collected by centrifugation and re-dispersed in water (1 mg/mL) for further conjugation. The surface functionalization and conjugation were verified by Fourier transform infrared spectroscopy (FTIR). The hydrodynamic sizes and the surface charges of the nanoparticles were measured using a Malvern Zetasizer Nano series dynamic light scattering (DLS).

5.2.4 Antibody conjugation

The dopamine functionalization of iron oxide nanoparticles allows for easy attachment of proteins through thiol or amino groups upon activation²⁸. The catechol groups on the

nanoparticle surfaces can be easily oxidized into dopamine quinone at higher pH (>8.5), creating an active surface for the conjugation. The clinical-grade, humanized, monoclonal anti-GD2 Hu14.18K322A antibody (referred to as hu14.18MoAb in this manuscript) was produced at Children's GMP LLC, Memphis, TN and kindly provided by Dr. R. Barfield. Briefly, 1 mL of activated, dopamine-coated iron oxide nanoparticles (1 mg/mL) was simply mixed with 100 μ L of hu14.18MoAb (8.6 mg/mL) in Bis-Tris (10 mM)-NaCl (10 mM) buffer for four hours. After centrifugation (10 min, 15000 rpm) and cleaning twice with Bis-Tris buffer solution to remove free antibodies, the cleaned, conjugated nanoparticles were re-dispersed in Bis-Tris (20 mM)-NaCl (20 mM) solution at a concentration of 1 mg/mL for cellular study. In addition to FTIR and DLS measurements, the presence of the antibody on nanoparticle surfaces was visualized by TEM negative staining technique. The TEM grid with antibody conjugated nanoparticles were immersed into uranyl acetate solution (2 %) with the sample side facing down for 10 min, and then rinsed in distilled water and Reynolds' lead citrate for seven minutes. After washing off the excess staining solution with 0.1 M NaOH and DI water, the stained TEM grids were dried on a filter paper and examined under TEM (Hitachi 7860).

5.2.5 Cell culture

The GD2-positive neuroblastoma cell line (CHLA-20), was kindly provided by Dr. Wayne A. Warner (Children's Hospital Los Angeles). The GD2 negative PC-3 prostate cancer cell line was obtained from ATCC. CHLA-20 cells were cultured in IMDM supplemented with 15% (v/v) FBS while PC-3 cells were grown in EMEM supplemented with 10% (v/v) FBS. Primary cultures of skin fibroblasts, cultured in DMEM supplemented with 10% (v/v) FBS, were used as normal cell controls. All the cells were incubated at 37 °C under a humidified atmosphere with

5% CO₂. The cell morphology and growth was daily monitored. Cell passage was performed every four days by detaching cells with trypsin-versene and re-growing in 75 cm² flasks.

5.2.6 Cellular targeting with antibody conjugated nanoparticles

To study the antibody activity after conjugation, CHLA-20 cells were treated with antibody-conjugated and unconjugated nanoparticles under the same conditions. Briefly, 2 mL of cells (5×10^4 cells/mL) were seeded in 6-well plates and cultured overnight. Subsequently, 400 μ L of nanoparticles (1 mg/mL) in 1.6 mL medium were added into each well and incubated for four or 12 hour. Finally, the nanoparticle treated cells were detached with trypsin-versene and washed three times with 1XPBS for further analysis.

The cell binding was evaluated by flow cytometry and fluorescence microscopy. Specifically, cells treated with nanoparticles for one hour were further incubated with a fluorescent goat-anti-human IgG Alexa Fluor 488 antibody. After incubation and washing, the cells were analyzed on a MACSQuant Analyzer 10 flow cytometer (Miltenyi Biotec), or on a Nikon Eclipse Ti-U fluorescence microscope with Intensilight C-HGFI, equipped with a DS-QiMc digital camera and Nis-Elements D3.10 software. In flow cytometry, propidium iodide was added to samples to allow the evaluation and exclusion of dead cells from the analysis; for fluorescence microscopy, DAPI was used as nuclear counter stain.

For iron staining, nanoparticle treated cells were attached onto the X-TRA permanent positively charged glass slides (Leica Biosystems. Inc) (1×10^5 cells/slide) by cytopsin. The attached cells were fixed with cold acetone for 10 min followed by the two-step Prussian blue staining at room temperature. Briefly, pre-mixed solutions of hydrochloric acid-potassium ferrocyanide were added to the cell-mounted slide for 30 min. This step was repeated once for fully staining the antibody-conjugated nanoparticles taken up by cells. After rinsing off the

excess stain solution with water, nuclear fast red solution was added to stain the nuclei and cytoplasm of cells for two minutes. Finally, the stained cells were dehydrated in a graded series of ethanol and xylene and fastened with the cover slip for staining pattern observation under inverted phase microscope.

The iron uptake by cells was quantified by ferrozine colorimetry²⁹. Briefly, 5×10^5 cells were treated with 60 $\mu\text{g/ml}$ nanoparticles for one hour at room temperature. After several washes, the cells were then lysed with 0.5M NaOH. The cell lysate was acidified with HCl and oxidized with 4% (w/v) KMnO_4 for two hours at 60°C . After reduction with 1M L-ascorbic acid, the ferrous ions were quantified by measuring the absorption at 570nm of their reaction product with 6.5mMferrozine, in the presence of 2.5 mM ammonium acetate and 6.5 mM neocuproine.

5.2.7 Cell targeting and competition experiments

To study the specific targeting ability of antibody-conjugated nanoparticles, CHLA-20 and PC-3 cells were treated with antibody-conjugated and unconjugated nanoparticles under the same conditions. To further confirm that indeed the interaction of GD2 receptor and hu14.18MoAb was responsible for the cellular uptake, a competition inhibition experiment was conducted. Specifically, 2 mL of CHLA-20 cells were seeded into 6-well plates (5×10^4 cells/mL) and cultured to 80% confluency before use. Free Hu 14.18 MoAb (100 nM) was then added to each well. After four hours incubation, 400 μL of antibody-conjugated nanoparticles (1 mg/mL) in 1.6 mL medium were added to both blocked and unblocked CHLA-20 cell cultures and incubated for four hours. For both experiments, ultrathin sections of nanoparticle-treated cells were prepared and scanned under TEM (Hitachi 7860, 120 kV). Specially, for the preparation of thin cell sections for TEM analysis, the NP-treated cells were firstly collected, and washed three times with SPB (sodium-phosphate buffer). SPB solution was simply prepared by mixing equal

volume of 0.2 M Na₂HPO₄·7H₂O and 0.2 M NaH₂PO₄·H₂O. Subsequently, the collected cells were fixed with SPB-diluted glutaraldehyde solution (2.5 %) at 4 °C for 30 min. After three washes with SPB, the cells were post-fixed with SPB-diluted osmium tetroxide (2 %) for 20 min at room temperature. After removing the free fixation agents with SPB, the cell samples were dehydrated in a graded series of ethanol (25, 50, 75, 95, and 100 %) and then infiltrated within 100 % resin solution. Finally, the solidified cell-resin blocks were trimmed and sectioned. The optimal cell section thickness was selected as 90 nm for this work.

5.3 Results and Discussion

5.3.1 Synthesis and functionalization of dopamine-coated iron oxide nanoparticles

The development of the iron oxide nanoparticle conjugation platform involved nanoparticle synthesis and dopamine surface functionalization steps. Iron oxide nanoparticles were synthesized using our modified heat up method^{25-28, 30, 31}, which produces nanoparticles with controlled size and narrow size distribution. After synthesis, the nanoparticles are only soluble in organic solvent, and must be transferred into aqueous solution for biological studies. We have recently developed a ligand exchange method to attach charged molecules onto iron oxide nanoparticle surfaces for water solubility²⁷. The success of this approach is based on the design of introducing a ligand with low affinity to the iron oxide nanoparticle (e.g., TOPO) as a co-capping molecule during synthesis. The introduction of TOPO molecules is critical for the surface functionalization, where the weaker binding affinity to iron oxide surfaces of TOPO molecules³² and its bulky C₈ tails³³ create preferred sites or “naked” spots on the nanoparticle surfaces for hydrophilic ligands to attach or bind, ensuring an effective ligand exchange process.

In this paper, dopamine was chosen as the surface functionalization molecule because of the easy oxidation property of the catechol group. The reaction was performed in DMSO, a non-

aqueous solution, which limits the formation of poly-dopamine like in many other aqueous reactions³⁴⁻³⁸. The use of dopamine molecules as functional surface coatings is key to the subsequent conjugation, where the amino group of the dopamine molecule attaches to the iron oxide nanoparticle surfaces, leaving the catechol group out. The catechol groups on the nanoparticle surfaces can be easily oxidized into dopamine quinone at higher pH (>8.5), creating an active surface for further conjugation. The activated dopamine groups allow for the direct conjugation of biological molecules containing amine and/or thiol groups through Michael addition and/or Schiff base formation^{39, 40}. The amino group attachment is different from iron oxide nanoparticles synthesized via the co-precipitation method at high pH, where the nanoparticles have surface bounded with hydroxyl groups. These surface hydroxyl groups interact with the catechol groups of dopamine molecules and leave the amino groups out^{41, 42}. The availability of the catechol groups on the nanoparticle surfaces is critically important to the direct conjugation of biological molecules. Importantly, this conjugation can be generalized for attaching other biological molecules to the iron oxide nanoparticle surfaces.

Fig 5.1a shows the TEM image of the well-dispersed dopamine-coated, 12 nm iron oxide nanoparticles in water. The high resolution TEM image indicated that the nanoparticles were highly crystalline (Fig 5.1b). The sharper lattice fringes and the clean boundary also suggested the absence of thick poly-dopamine layer, because the formation of thick poly-dopamine layer has been observed on several nanoparticle systems³⁵⁻³⁸. This observation also supports our hypothesis that the amino group of the dopamine molecule was attached onto iron oxide nanoparticle surface, which limited the formation of thick poly-dopamine layer. However, it is possible to form some patches of thin poly-dopamine due to the presence of excess free dopamine after water dispersion, as shown in selected HRTEM images (Fig. S5.1).

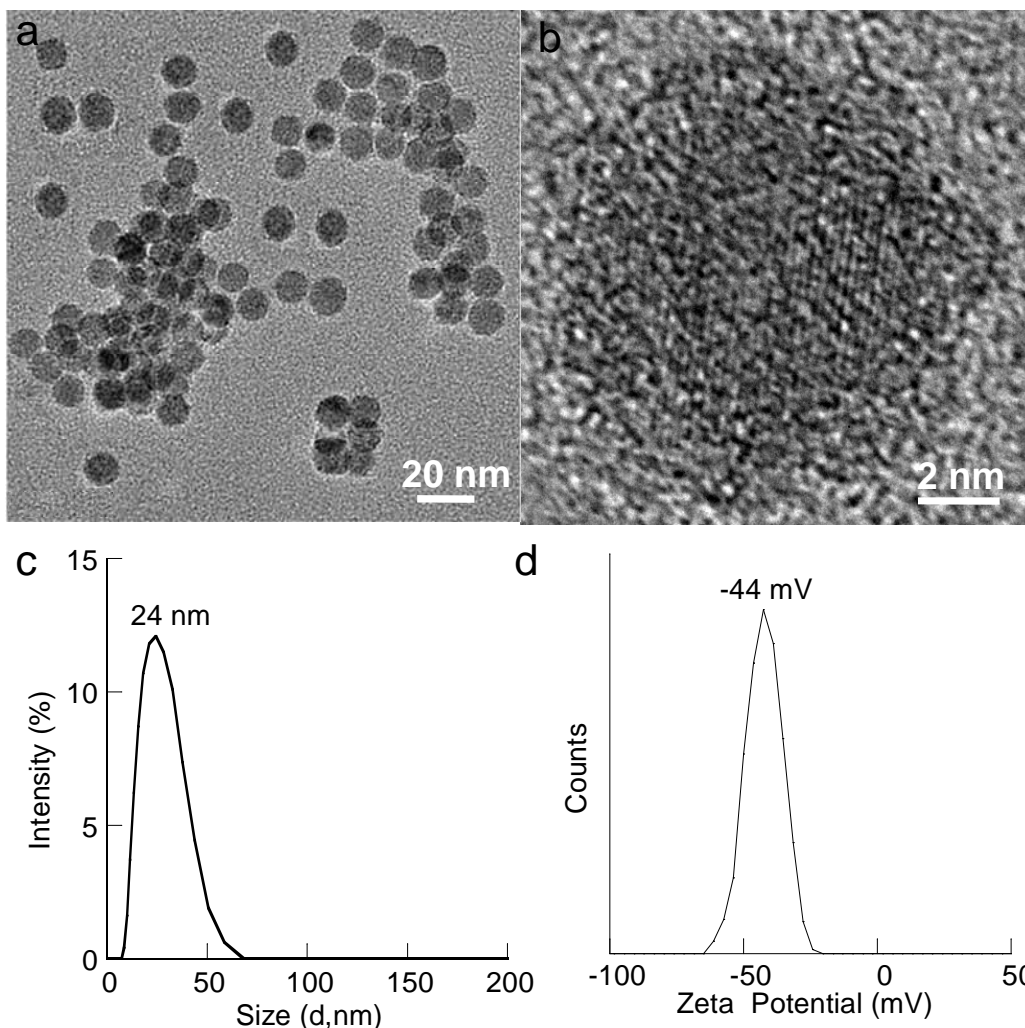


Figure 5.1 Dopamine functionalized iron oxide nanoparticles: (a) TEM image, (b) high resolution TEM image, (c) DLS plot, and (d) zeta-potential plot.

The amino group attachment was consistent with our previous studies showing that the amino group has a preferable binding to iron oxide nanoparticles over other functional groups^{27, 28, 32}. The hydrodynamic size of the dopamine-coated nanoparticles increased to 24 nm (Fig 5.1c), compared to the 18 nm in organic solvent (Figure S5.2). The presence of the catechol groups on the dopamine-coated nanoparticle surface was also supported by the negative zeta-potential (-44 mV, Fig 5.1d). If catechol functional groups are attached to the nanoparticles, the amino groups on the nanoparticle surfaces would lead to a positive zeta-potential. The catechol

groups on the nanoparticle surfaces can be easily oxidized into dopamine-quinone at higher pH (>8.5), creating an active surface for further effective conjugation of antibody.

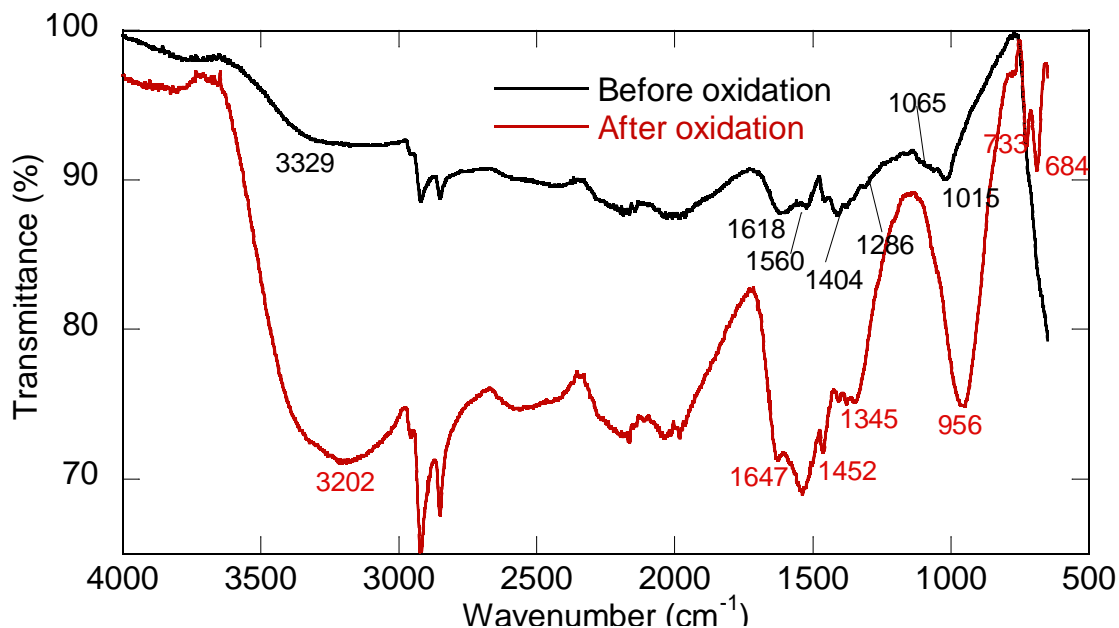


Figure 5.2. FTIR spectra of dopamine – coated iron oxide nanoparticles before and after oxidation.

The IR spectra of the dopamine-functionalized iron oxide nanoparticles before and after activation were shown in Fig 5.2. Compared with the IR spectrum before activation, a peak at 1647 cm⁻¹ appeared, which is the characteristic of -C=O band in quinone structure⁴³. Accordingly, the characteristic band of -C-O at 1282 cm⁻¹ disappeared after activation. In addition, the typical phenol alcohol band at 1065 cm⁻¹ disappeared, and a strong -CH=CH- ring breathing mode at 956 cm⁻¹ showed up. All these IR absorption changes indicated the dopamine oxidation process on the nanoparticle surfaces. The activated dopamine groups allowed for the direct conjugation of biological molecules through Michael addition and/or Schiff base formation^{39, 40}. Because of the stability issue with the Schiff base⁴⁴, the Michael addition reaction commonly happens⁴⁵.

5.3.2 Characterization of antibody-conjugated iron oxide nanoparticles

Fig. 3a shows the negative stained TEM image of the hu14.18MoAb conjugated iron oxide nanoparticles, where the lighter shells around the nanoparticles were from the antibodies. Depending on the orientation of the antibody, the shell region can be larger or small. The tiny black spots around the nanoparticles were from the staining solution, where possible undissolved uranyl acetate stain or lead carbonate precipitation from lead citrate stain absorbed CO₂ from air.

The antibody conjugation shifted the zeta-potential of the nanoparticles from -44 eV to -34 eV (Fig 5.3b). Even through the zeta-potential increased about 10 mV, the suspension of the antibody conjugated nanoparticle solution was still stable. After antibody conjugation, the hydrodynamic sizes of the nanoparticles increased about 20 nm, another indication of antibody attachment (Fig 5.3c). The FTIR spectrum of the antibody conjugated nanoparticles showed clear amide I (1633 cm^{-1}) and amide II (1520 cm^{-1}) bands, also suggesting the attachment of antibodies. After conjugation, the amine or thiol groups normally attached to the fourth position adjacent to a hydroxyl group through Michael addition and the quinone shifted back to hydroxyl groups. This process was supported by the IR spectrum of antibody-conjugated nanoparticles, where hydroxyl and its C-O bands at 1065 and 1005 cm^{-1} were clearly seen, compared with the strong $-\text{CH}=\text{CH}-$ ring breathing peak at 956 cm^{-1} (Fig 5.2). In fact, the IR bands in the range of $900\text{-}1100\text{ cm}^{-1}$ of the antibody conjugated nanoparticles was very similar to the dopamine coated nanoparticles before oxidation.

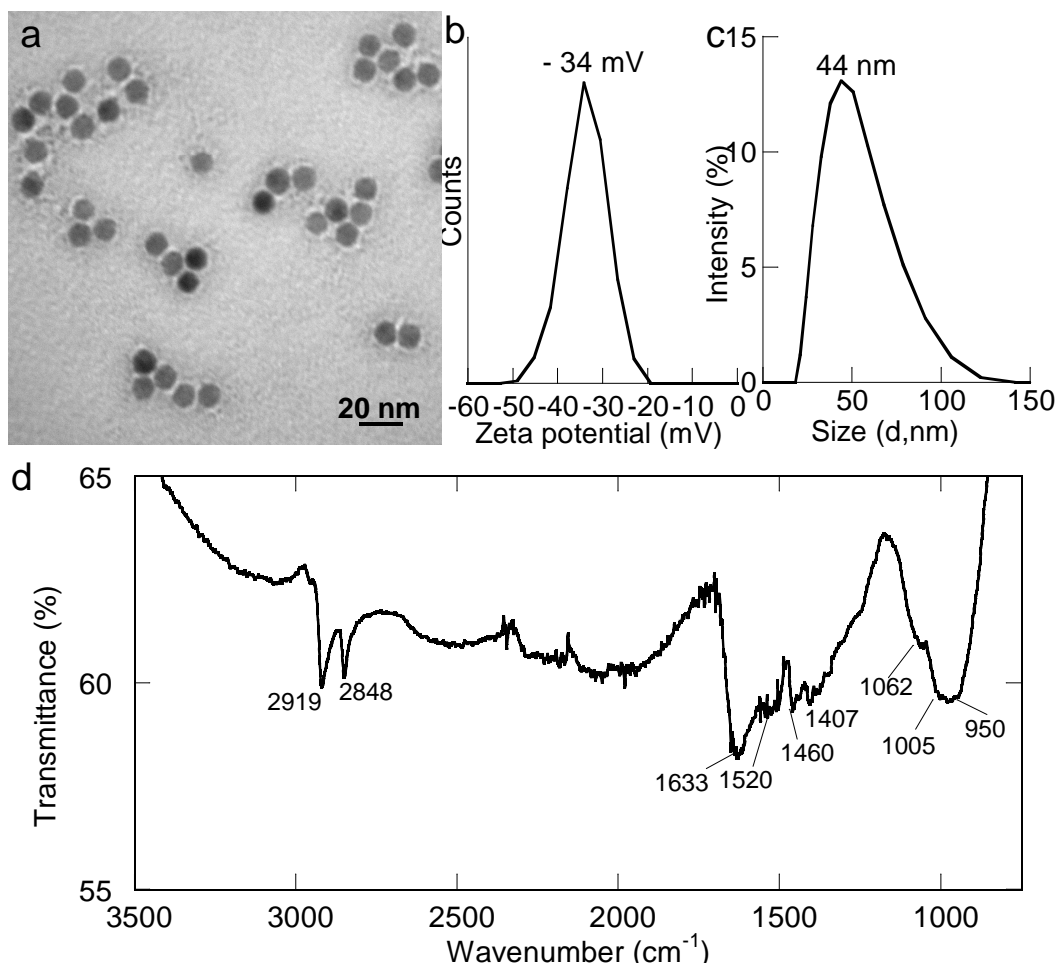


Figure 5.3. Antibody conjugated iron oxide nanoparticles: (a) TEM image, (b) Zeta-potential plot, (c) DLS plot, and (d) FTIR spectrum.

5.3.3 Cell targeting evaluation of antibody-conjugated iron oxide nanoparticles

To evaluate the targeting capability of the hu14.18MoAb after attaching on the iron oxide nanoparticles, several cellular targeting experiments were performed on GD2-positive cell lines (CHLA-20) and GD2 negative control cell lines (PC-3) or normal fibroblasts. CHLA-20 neuroblastoma cells have a high level of expression of GD2 antigen on the cell surface while PC-3 cells and normal fibroblasts do not express the GD2 receptor, serving as suitable negative controls⁴⁶. The localization of the nanoparticles on CHLA-20 cell surface was visualized by fluorescence microscopy using green-fluorescent Alexa 488-labeled anti-human IgG antibody.

The lack of green fluorescence after the treatment of cells with unconjugated nanoparticles and anti-human IgG antibody (Fig 5.4a) indicated the absence of a nonspecific reaction of the detection system used. Remarkably, the sharp green shell around the cell surface (Fig 5.4b) suggested the high level of binding of the antibody-conjugated nanoparticles to GD2-positive cells.

In contrast, the antibody-conjugated nanoparticles did not bind to GD2-negative cells (such as normal fibroblasts, Fig 5.4c, 4d), indicating their high specificity of recognizing of GD2 receptors. The binding of antibody-conjugated nanoparticles to GD2-positive cells (CHLA-20) was quantified by flow cytometry, yielding a up to 250-fold increase of the mean fluorescence intensity above the autofluorescence of the cells (Fig 5.4e), whereas the binding to GD2-negative cells (such as normal fibroblasts and PC-3) did not increase the cell fluorescence more than 1.2 fold (data not shown), strongly supporting the binding specificity of antibody-conjugated nanoparticles. The antibody binding increased with increasing nanoparticle concentrations and reached saturation at a Fe concentration of $\sim 60 \mu\text{g/mL}$ (corresponding with $2 \mu\text{g}$ antibody/million cells) (Fig 5.4f). A comparison of the binding of the antibody-conjugated nanoparticles with the original hu14.18MoAbby flow cytometry indicated minor differences in binding, especially after reaching saturation (Fig 5.4f), indicating that the conjugation process did not substantially alter the antibody binding properties.

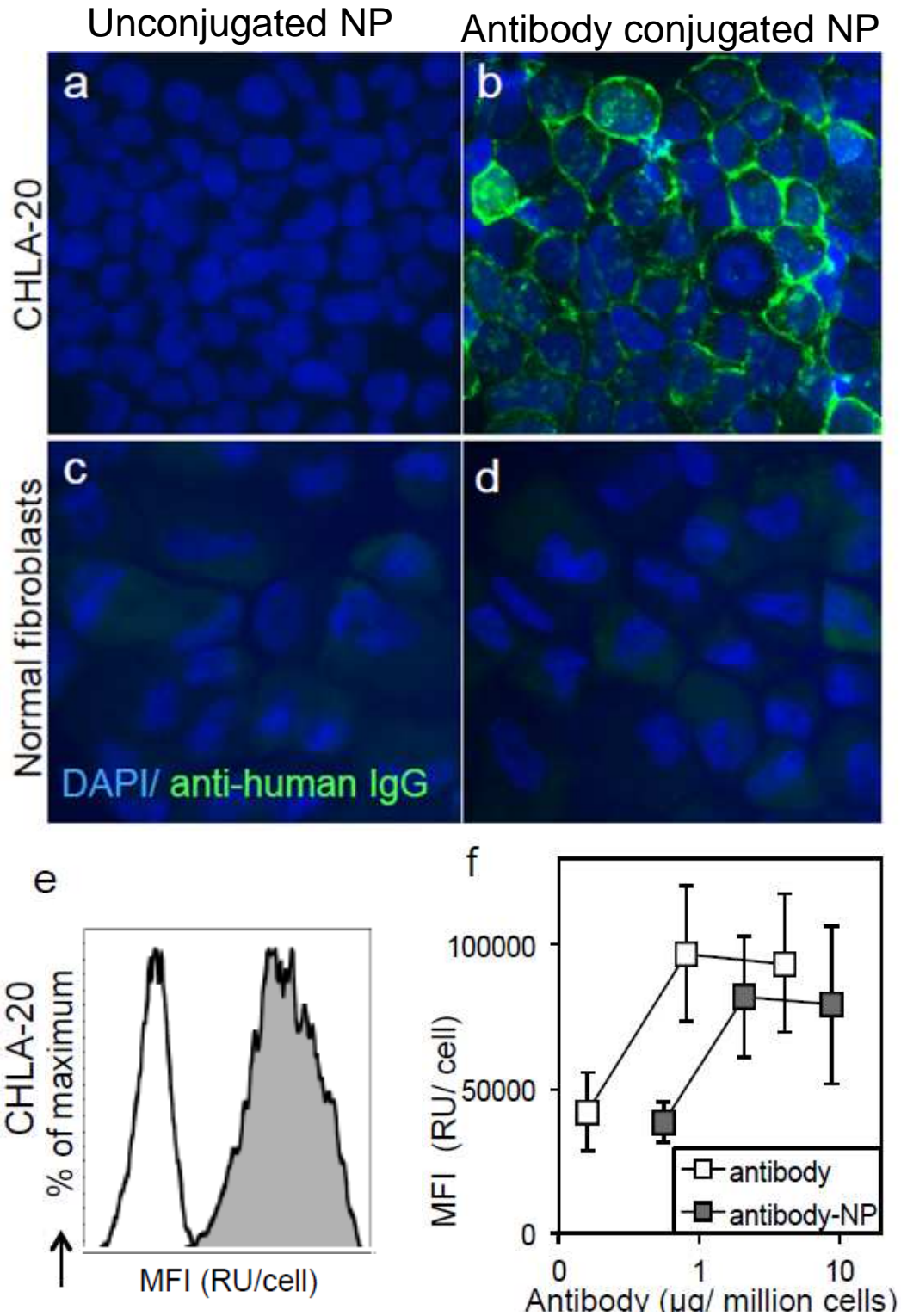


Figure 5.4. Binding evaluation of hu14.18MoAb-conjugated iron oxide nanoparticles to neuroblastoma cells (CHLA-20) : (Fluorescence microscopy (400X) of CHLA-20 cells or normal fibroblasts treated with unconjugated (a, c) or antibody-conjugated (b, d) nanoparticles and Alexa 488-anti-human IgG antibody. (e) Flow cytometry of cell auto-fluorescence (clear

histogram) and antibody-conjugated nanoparticles bound to cells (tinted histogram). (f) Flow cytometry binding curves of Hu14.18MoAb (antibody) and hu14.18MoAb-conjugated nanoparticles (antibody-NP) to CHLA-20 cells. Averages \pm SD of three experiments. NP, nanoparticles. DAPI, nuclear counterstain. MFI, mean fluorescence intensity. RU, relative units.

To confirm the co-localization of the nanoparticles with antibody, Prussian blue iron staining was performed on CHLA-20 cells treated with conjugated and unconjugated nanoparticles. CHLA-20 cells treated with unconjugated, dopamine-coated nanoparticles only showed occasional big blue spots from nanoparticle aggregates (Fig 5.5a). In contrast, the cells treated with antibody conjugated nanoparticles showed clear blue shells around the cells, suggesting the presence of the nanoparticles around the cell membranes (Fig 5.5b). In conjunction with the fluorescent microscopy image, this observation suggested the co-localization of nanoparticles and antibodies. The quantification of cellular iron uptake by ferrozine colorimetry indicated significant increase in iron concentration for cells treated with antibody conjugated iron oxide nanoparticles (Fig 5.5c). The flow cytometry evaluation of the biocompatibility of the iron oxide nanoparticles by propidium iodide exclusion, following cell treatment with medium alone (no NP), unconjugated (NP) or antibody-conjugated nanoparticles (antibody-NP) suggested that the conjugation did not alter the cell viability significantly (Fig 5.5d).

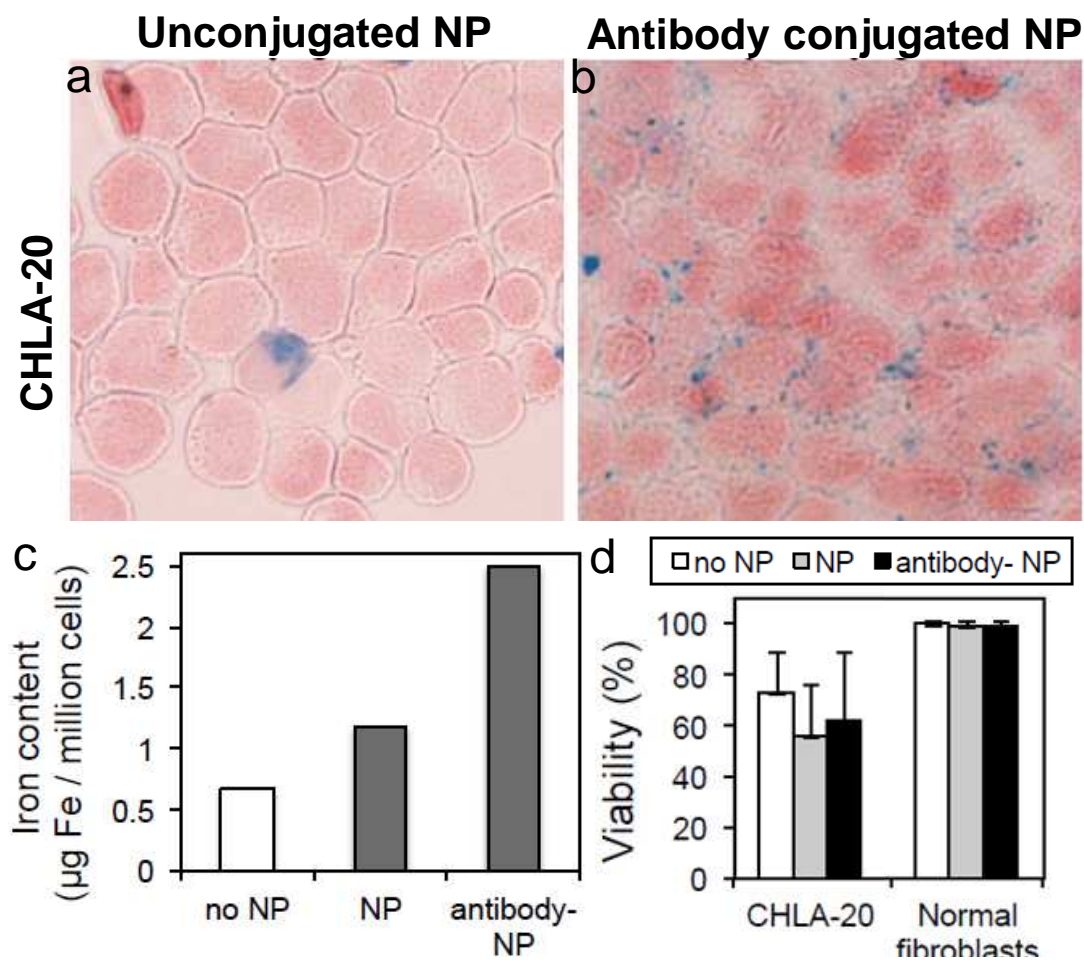


Figure 5.5. Perls staining using Prussian blue reaction detecting iron for (a) unconjugated and (b) antibody-conjugated iron oxide nanoparticles. (c) Quantification by ferrozine reaction of the iron content of CHLA-20 cells following treatment with medium alone (no NP), unconjugated (NP) or antibody-conjugated nanoparticles (antibody-NP). (d) Flow cytometry evaluation of the biocompatibility of the dopamine-coated iron oxide nanoparticles by propidium iodide exclusion, following cell treatment with medium alone (no NP), unconjugated (NP) or antibody-conjugated nanoparticles (antibody-NP). Averages +/- SD of three independent experiments are shown.

5.3.4 Cellular uptake of antibody-conjugated nanoparticles

The detailed cellular uptake of the antibody-conjugated nanoparticles was further studied using TEM. Fig 5.6 shows the time-dependent cellular uptake and distribution of nanoparticles on GD2 positive CHLA-20 cells and GD2-negative PC-3 cells. The GD2 binding of the antibody-conjugated nanoparticles was compared with the unconjugated, dopamine-coated nanoparticles. After four hours incubation, the cellular uptake and localization of unconjugated

nanoparticles on CHLA-20 and PC-3 cells showed little difference (Fig 5.6a-d). The unconjugated nanoparticles were primarily taken up through endocytosis and ended up inside endosomal- or lysosomal-like organelles (red circles). The corresponding detailed information was shown in Fig 5.6b, 6d. In contrast, after four hours incubation with antibody-conjugated nanoparticles, many nanoparticles were attached onto CHLA-20 plasma membranes (Fig 5.6e), and the nanoparticle morphology could be clearly observed at higher magnification (Fig 5.6f). No cell membrane anchored nanoparticles were observed on PC-3 cells, which lack GD2 cell receptors (Fig 5.6g). Instead, antibody-conjugated nanoparticles were localized inside endosomal- or lysosomal-like organelles, indicated by the visible membrane edge in Fig 5.6h. This study demonstrated the specific GD2 recognition and binding of the antibody-conjugated nanoparticles. Besides the high selective targeting capacity, the internalized conjugated nanoparticles were well dispersed inside the cells without morphology change and free of aggregation.

At 12 hours, nanoparticles on CHLA-20 cell membranes were internalized, leading to much cleaner cell surfaces. Some internalized nanoparticles were found inside endosomal- or lysosomal-like organelles but some nanoparticles were localized in the cytosol because the nanoparticles might enter cells by penetrating the plasma membrane or endosomal or lysosomal-like organelles membranes were ruptured (blue-dashed circles in Fig 5.6i and the enlarged image of Fig 5.6j). At 12 hours, not much difference was observed on TEM images of the PC-3 cells treated antibody-conjugated nanoparticles, compared with that from the four hour treatment (Fig 5.6k). The internalized, conjugated nanoparticles were still located in endosomal- or lysosomal-like organelles with the clearly observed membrane (Fig. 5.6l). This result suggested that the

hu14.18MoAb-GD2 interaction was responsible for the specific uptake of antibody-conjugated nanoparticles by GD2-positive cells.

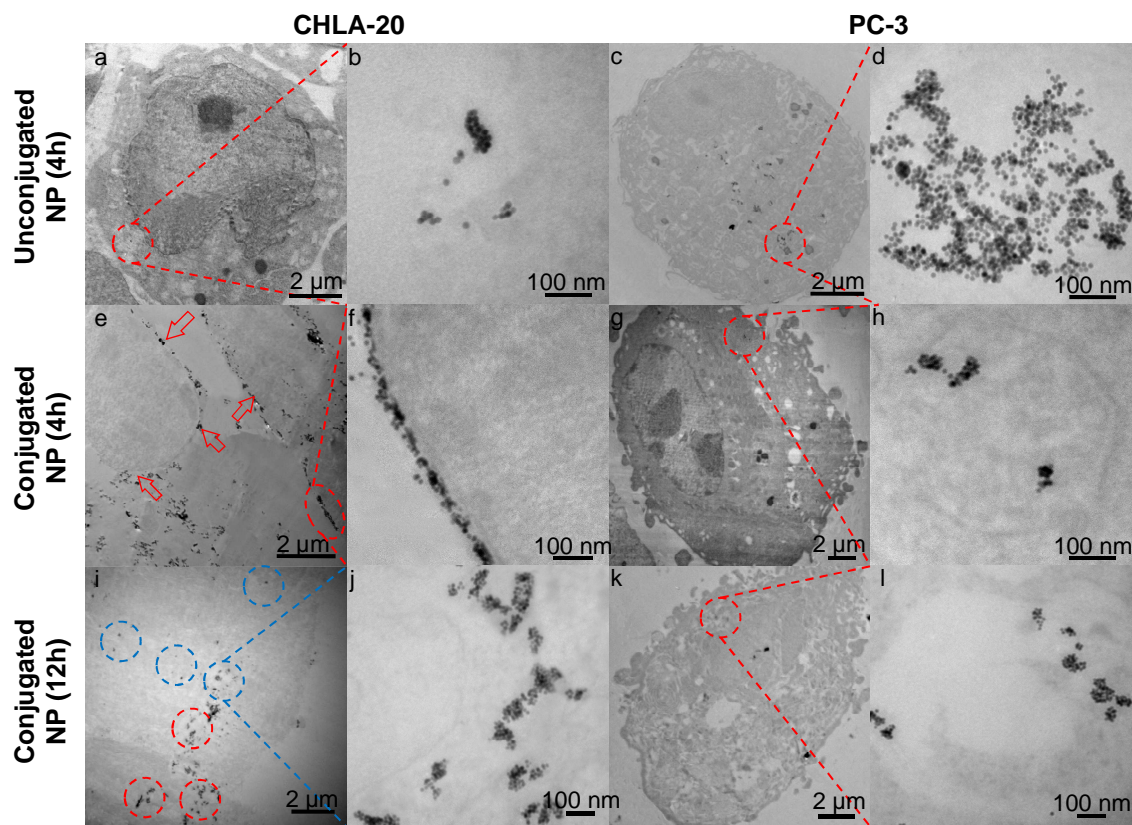


Figure 5.6. Comparison of nanoparticle recognition and internalization on CHLA-20 and PC-3 cells: (a and c) cells treated with dopamine-coated nanoparticles for four hours, (e and g) cells treated with antibody-conjugated NPs for four hour, and (i and k) cells treated with antibody-conjugated NPs for 12 hour, (b, d, f, h, j, l) higher magnification of the areas that red/blue-dashed circle indicates.

To further confirm the role of the hu14.18MoAb in the recognition of nanoparticles by CHLA-20 cells, an antibody competition experiment was performed (Fig 5.7). The CHLA-20 cells were first treated with free hu14.18MoAb (100 nM) for four hours, followed by the addition of antibody-conjugated nanoparticles for another four hours. The incubation of CHLA-20 cells with free hu14.18MoAb was designed to block all the GD2 receptors on the cell surfaces. Such a blockade would subsequently limit the GD2 recognition and binding of the antibody-conjugated nanoparticles. Then, the cellular uptake was compared with unblocked CHLA-20

cells treated with antibody-conjugated nanoparticles. Fig 5.7a shows the TEM images of the unblocked and blocked CHLA-20 cells treated with antibody-conjugated nanoparticles. Without the blockage of GD2 receptors by free antibody, the nanoparticles were primarily localized on the surface of the CHLA-20 cells (Fig 5.7b), similar to Fig 5.6c. After blockage of the GD2 receptors by free antibodies, the nanoparticle surface recognition and binding were barely seen and the internalization was significantly reduced (Fig 5.7c, 7d). These results demonstrated that the enhanced cell binding in GD2-positive neuroblastoma cells was a direct result of GD2-hu14.18MoAb interactions.

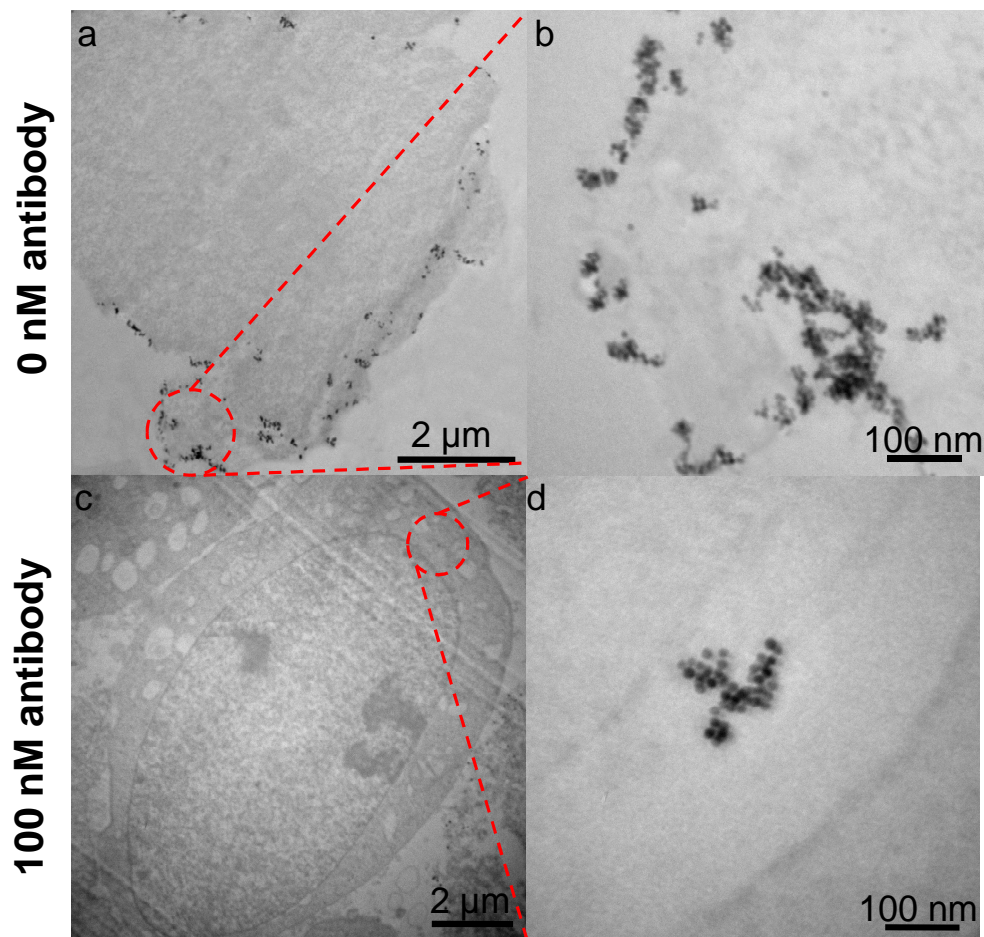


Figure 5.7. The binding competition experiments on CHLA-20 cells: (a) GD2 unblocked CHLA-20 cells treated with antibody-conjugated NPs for four hours, (c) GD2 blocked CHLA-20 cells

treated with antibody-conjugated nanoparticles for four hours. (b and d) Higher magnification of the areas that red-dashed circle indicates.

5.4 Conclusion

In this paper we describe the development of a novel and facile conjugation platform for iron oxide nanoparticles. The method circumvents the use of chemical linkers, thereby eliminating the disadvantages inherent to this type of conjugation chemistry, such as non-physiological reaction conditions and competition of reactive groups leading to low conjugation efficiency. To show proof of principle with a therapeutically relevant, biologically active targeting moiety, we used a humanized antibody for conjugation to the nanoparticles (Fig 5.8 left section). Our method utilizes a simple, one-step approach, which is both time-saving as well as economical and could facilitate large-scale production of diagnostically and therapeutically valuable iron oxide nanoparticles. The antibody-conjugated nanoparticles fully retained the antibody binding capacity and presented a high targeting selectivity on GD2-positive cells (CHLA-20), as compared to GD2-negative cells (PC-3, and normal fibroblasts). The targeting efficiency was verified with several complementary techniques, including flow cytometry, fluorescence microscopy, Prussian blue staining and transmission electron microscopy. Importantly, we observed the membrane-anchored, conjugated nanoparticles via GD2 receptors were capable of transporting into cytosols, providing a promising platform to load the cancer-curing drug on and perform targeted therapy in future applications.

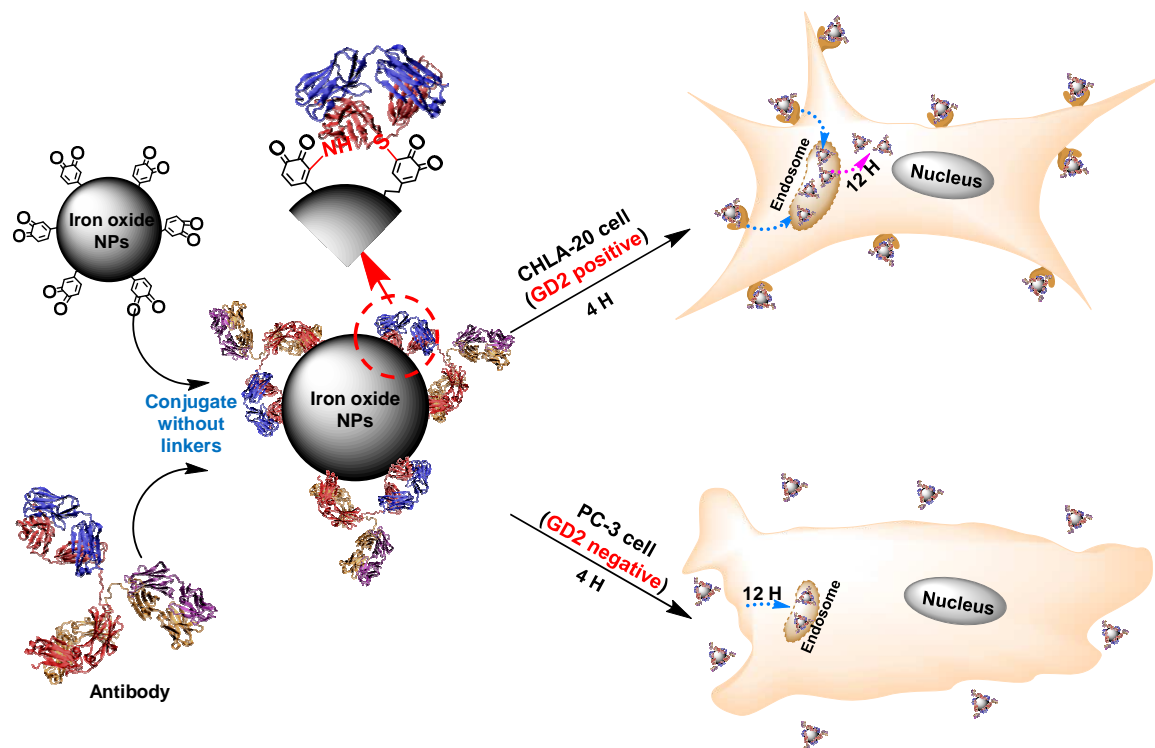


Figure 5.8. Schematic drawing of Hu14.18MoAb antibody conjugation with iron oxide nanoparticles (left section) and their targeting efficiency tests on GD2-positive (CHLA-20) and GD2-negative (PC-3) cells (right section).

Acknowledgements

This work is supported by NSF-DMR 0907204 and DMR1149931. We acknowledge the UA Central Analytical Facility (CAF) and the Biological Science Department for the use of TEM. The authors would like to thank the University of Wisconsin Carbone Comprehensive Cancer Center (UWCCC) for use of its facilities to complete this research. This work was supported in part by NIH/NCI P30 CA014520-UWCCC Comprehensive Cancer Center Support. The work was also supported in part by the MACC Fund (Midwest Athletes against Childhood Cancer).

Supplementary data

Electronic Supplementary Information (ESI) available: [details of any supplementary information available should be included here]. See DOI: 10.1039/b000000x/

5.5 References

1. Xie J, Huang J, Li X, Sun S, Chen X. *Curr. Med. Chem.* **2009**, *16*, 1278-1294.
2. Namdeo M, Saxena S, Tankhiwale R, Bajpai M, Mohan YM, Bajpai SK. *J. Nanosci. Nanotechnol.* **2008**, *8*, 3247-3271.
3. Gazeau F, Levy M, Wilhelm C. *Nanomed.* **2008**, *3*, 831-844.
4. Krishnan KM. *IEEE Trans. Magn.* **2010**, *46*, 2523-2558.
5. Reimer P, Balzer T. *Eur. Radiol.* **2003**, *13*, 1266-1276.
6. Hamm B, Staks T, Tapuiz M, Maibauer R, Speidel A, Huppertz A, Frenzel T, Lawaczeck R, Wolf KJ, Lange L. *Jmri: J. Magn. Reson. Imaging* **1994**, *4*, 659-668.
7. Baiu DC, Brazel C, Bao Y, Otto M. *Curr. Pharm. Des.* **2013**, *19*, 6606-6621.
8. Modak S, Cheung NK. *Cancer Invest.* **2007**, *25*, 67-77.
9. Yoshida S, Fukumoto S, Kawaguchi H, Sato S, Ueda R, Furukawa K. *Cancer Res.* **2001**, *61*, 4244-4252.
10. Navid F, Santana VM, Barfield RC. *Curr. Cancer Drug Targets* **2010**, *10*, 200-209.
11. Navid F, Barfield R, Handgretinger R, Sondel P, Shulkin B, Kaufman R, Billups C, Wu J, Furman WL, McGregor LM, Otto M, Gillies S, Santana VM. *J. Clin. Oncol.* **2011**, *29*, 9523. Available from URL: http://meeting.ascopubs.org/cgi/content/short/29/15_suppl/9523?rss=1
12. Navid F, Sondel PM, Barfield RC, Shulkin BL, Kaufman R, Allay JA. *J. Clin. Oncol.* **2014**, in press.
13. Sperling RA, Parak WJ. *Phil. Trans. R. Soc. A: Math Phys. Eng. Sci.* **2010**, *368*, 1333-1383.
14. Hadjipanayis CG, Machaidze R, Kaluzova M, Wang LY, Schuette AJ, Chen H, Wu X, Mao H. *Cancer Res.* **2010**, *70*, 6303-6312.
15. Mahmoudi M, Simchi A, Imani M. *J. Iran Chem. Soc.* **2010**, *7*:S1-S27.
16. Nam J, Won N, Bang J, Jin H, Park J, Jung S, Park Y, Kim S. *Adv. Drug Delivery Rev.* **2013**, *65*, 622-648.
17. Erathodiyil N, Ying JY. *Acc. Chem. Res.* **2011**, *44*, 925-935.
18. Montenegro JM, Grazu V, Sukhanova A, Agarwal S, Fuente JM, Nabiev I, Greiner A, Parak WJ. *Adv. Drug Delivery Rev.* **2013**, *65*, 677-688.
19. Kalia J, Raines RT. *Curr. Org. Chem.* **2010**, *14*, 138-147.

20. Hermanson GT. Bioconjugate Techniques. *Academic Press*, **2008**. 2nd edn.
21. Madler S, Bich C, Touboul D, Zenobi R. *J. Mass Spectrom.* **2009**, *44*, 694-706.
22. Kalkhof S, Sinz A. *Ana. Bioanal. Chem.* **2008**, *392*, 305-312.
23. Wilchek M, Bayer EA, Livnah O. *Immunol. Lett.* **2006**, *103*, 27-32.
24. <http://www.piercenet.com/>, technical notes.
25. Palchoudhury S, Xu Y, Goodwin J, Bao Y. *J. Appl. Phys.* **2011**, *109*, 07E314.
26. Palchoudhury S, Xu Y, Goodwin J, Bao Y. *J. Mater. Chem.* **2011**, *21*, 3966-3970.
27. Xu Y, Qin Y, Palchoudhury S, Bao Y. *Langmuir* **2011**, *27*, 8990-8997.
28. Xu Y, Palchoudhury S, Qin Y, Macher T, Bao Y. *Langmuir* **2012**, *28*, 8767-8772.
29. Riemer J, Hoepken HH, Czerwinska H, Robinson SR, Dringen R. *Anal. Biochem.* **2004**, *331*, 370-375.
30. Palchoudhury S, An W, Xu Y, Qin Y, Zhang Z, Chopra N, Holler RA, Turner CH, Bao Y. *Nano Lett.* **2011**, *11*, 1141-1146.
31. Palchoudhury S, Xu Y, Rushdi A, Holler RA, Bao Y. *Chem. Commun.* **2012**, *48*, 10499-10501.
32. Palchoudhury S, Xu Y, An W, Turner CH, Bao Y. *J. Appl. Phys.* **2010**, *107*, 09B311.
33. Bao Y, Beerman M, Pakhomov AB, Krishnan KM, *J. Phys. Chem. B* **2005**, *109*, 7220-7222.
34. Black KCL, Yi J, Rivera JG, Zelasko-Leon DC, *Nanomed.* **2013**, *8*, 17-28.
35. Zeng T, Zhang X, Niu H, Ma Y, Li W, Cai Y. *Appl. Catal. B: Environ.* **2013**, *134*, 26-33.
36. Si J, Yang H. *Mater. Chem. Phys.* **2011**, *128*, 519-524.
37. Zhang M, Zhang X, He X, Chen L, Zhang Y. *Nanoscale* **2012**, *4*, 3141-3147.
38. Feng J, Zhang P, Wang A, Liao Q, Xi J, Chen J. *New J. Chem.* **2012**, *36*, 148-154.
39. Lee H, Rho J, Messersmith PB. *Adv. Mater.* **2009**, *21*, 431-434.
40. Lee H, Dellatore SM, Miller WM, Messersmith PB. *Science* **2007**, *318*, 426-430.
41. Durgadas CV, Sharma CP, Sreenivasan K. *Nanoscale* **2011**, *3*, 4780-4787.
42. Shultz MD, Reveles JU, Khanna SN, Carpenter EE. *J. Am. Chem. Soc.* **2007**, *129*, 2482-2487.

43. Wang X, Jin B, Lin X. *Anal. Sci.* **2002**, *18*, 931-933.
44. Belowich ME, Stoddart JF. *Chem. Soc. Rev.* **2012**, *41*, 2003-2024.
45. Dagnino-Subiabre A, Cassels BK, Baez S, Johansson AS, Mannervik B, Segura-Aguilar J. *Biochem. Biophys. Res. Commun.* **2000**, *274*, 32-36.
46. Jiao P, Zhou H, Otto M, Mu Q, Li L, Su G, Zhang Y, Butch ER, Snyder SE, Jiang G, Yan B. *J. Am. Chem. Soc.* **2011**, *133*, 13918-13921.

5.6 Supporting information

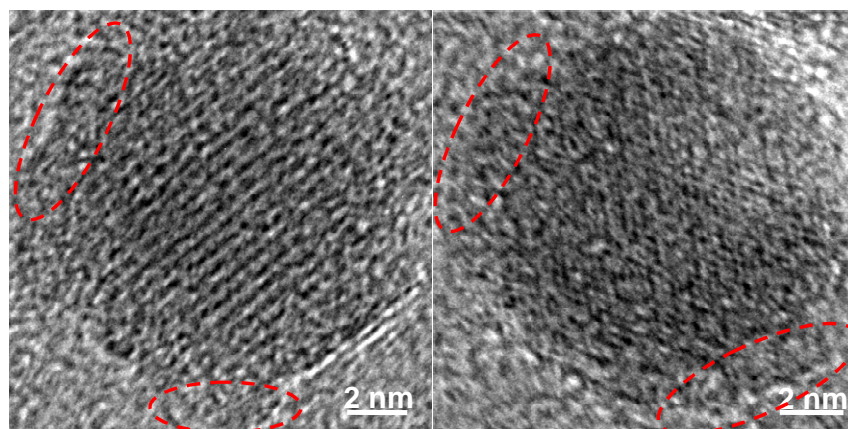


Figure S5.1. HRTEM images of dopamine-coated iron oxide nanoparticles, where the possible polydopamine patches were highlighted with red circles.

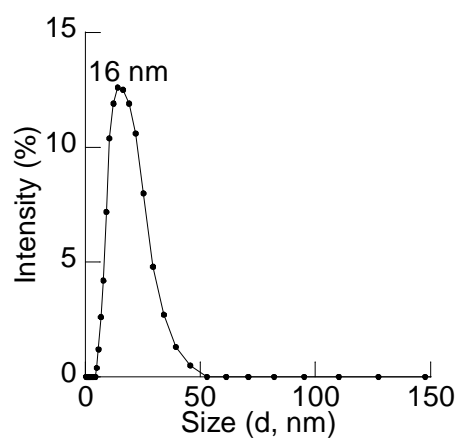


Figure S5.2. DLS plot of iron oxide nanoparticles in hexane.

CHAPTER 6

CONCLUSIONS AND FUTURE WORKS

In this dissertation, two multifunctional nanoparticles were successfully prepared by integrating fluorescent gold nanoclusters or antibodies with activated, dopamine-coated iron oxide nanoparticles, namely, dual-imaging or cancer-cell targeting nanoparticles. After integration, both hydrodynamic sizes and zeta potential values of integrated nanoparticles were increased, compared to dopamine-coated nanoparticles, which were the first indicators for the successful integration. The success of integration was also reflected from the retained property of each component in integrated nanoparticles. Specifically, for dual-imaging nanoparticles, their fluorescent and magnetic properties were detected using fluorescent spectroscopy and AGM measurements. The structural integrity was observed using high-resolution TEM and HAADF, which suggested single gold nanocluster attachment onto one dopamine-coated nanoparticle. For cancer-cell targeting nanoparticles, the antibodies on nanoparticle surfaces were clearly observed using TEM negative staining. Subsequently, flow cytometry, fluorescent microscopy, Prussian blue staining, and TEM were applied and all indicated the efficient and specific targeting of antibody-conjugated nanoparticles to cancer cells. The creation of these two multifunctional nanoparticles open up new possibilities for exploring iron oxide nanoparticles in biomedical applications.

Through the course of studies, I found several critical steps to the success of this project. During the preparation of water-soluble iron oxide nanoparticles, I firstly discovered that TOPO must be used as the co-surfactant during the synthesis of iron oxide nanoparticles. This

modification did not change the dimensions or properties of iron oxide nanoparticles, but was critical for the subsequent step, ligand exchange process. With OA used only, water-soluble nanoparticles would not be achieved. Second, an optimized ligand-to-nanoparticle ratio (5:1) was set for the ligand exchange reactions. The as-prepared water-soluble nanoparticles possessed small hydrodynamic size and narrow size distribution. Lack of enough hydrophilic ligands significantly caused nanoparticle aggregation. Finally, the buffer species and concentration was found greatly affecting the stability of water-soluble nanoparticles. Nanoparticles presented great stability in HEPES, MES, and NaCl solution, but not stable in PBS. Increased salt concentration in HEPES, MES, and NaCl solution led to the alternation of nanoparticle hydrodynamic size and zeta potential values, but the resulting nanoparticle dispersion still remained stable. These results provided new insight into nanoparticle behavior in biological conditions.

Most importantly, the ligand exchange strategy can be applied to many different molecules, such as dopamine, amine-terminated PEG, and dextran. Among these hydrophilic ligands, dopamine attracted great attention because the dopamine-coated iron oxide nanoparticles could easily integrate with other surface moieties. Easy oxidization of the catechol groups on nanoparticle surfaces led to the formation of dopamine-quinone, which was confirmed using both UV-vis and FTIR. The resulting structure can directly conjugate with amine and/or thiol group-containing molecules through Michael addition and/or Schiff base formation. This facile approach eliminated the use of toxic linkers and harsh conjugation conditions, while providing the robust binding with new surface moieties and retaining the activities of the conjugated molecules to the greatest extent.

With this innovative integration strategy, magnetic-fluorescent dual-imaging nanoparticles were prepared by integrating activated, dopamine-coated nanoparticles with

protein (such as bovine serum albumin, trypsin and lysozyme) - encapsulated fluorescent nanoclusters. Both TEM and fluorescent spectroscopy confirmed that the dual-imaging nanoparticles remained their structural integrity and physical properties in various environments, such as PBS, HEPES, MES, and EMEM cell medium. Interestingly, during the stability tests, I also found the fluorescence intensity of dual-imaging nanoparticles was enhanced in buffer solution, and the detailed mechanism for this phenomenon will be studied in the future.

The mechanism study of gold nanocluster formation showed that the balance of amine-containing and tyrosine/tryptophan residues in protein templates was critical for the preparation of gold nanoclusters and determined their size and fluorescent properties. The cysteine contents of proteins also affected fluorescent emission, intensity, and lifetime of gold nanoclusters. Additionally, the protein size critically influenced the photo, thermal, chemical stability of gold nanoclusters, and also the fluorescent properties of immobilized gold nanoclusters. More detailed investigations be conducted in the future to fully understand the fluorescent property change.

With the activated, dopamine-coated nanoparticles, antibodies were also successfully conjugated onto nanoparticle surfaces, which created the cancer-cell targeting nanoparticles. The specificity and selectively targeting of antibody-conjugated nanoparticles to GD2-positive cancer cells were confirmed using flow cytometry, Prussian blue staining, TEM, and fluorescence microscopy. More interestingly, time-dependent TEM studies on treated cancer cells revealed that the membrane-anchored, conjugated nanoparticles were capable of transporting into cytosols.

Besides the already-published work, I also conducted studies on the biological responses of human monocytes to different surface-charged iron oxide nanoparticles, and this manuscript will be submitted in the near future. For any biological application, nanomaterials need to be injected

into the human body and directly interact with the patients' immune system.¹ Human monocytes, derived from bone marrow stem cells and circulating in the bloodstream, are considered the front line of host immune systems.² In our studies, three surface-charged (e.g. negatively, positively and neutral) iron oxide nanoparticles were prepared by choosing polyacrylic acid-PAA, polyethylenimine-PEI and polyethylene glycol-PEG as surface coatings, respectively. The stability and surface charges of nanoparticles were fully tested in both water and cell medium. Subsequently, nanoparticle concentration- and time-dependent experiments were conducted to study the biological effects of surface-charged nanoparticles on human monocytes. All three surface-charged nanoparticles were considered biocompatible after toxicity evaluation, and nearly-no immune response was observed in nanoparticle-treated monocytes.

The stability studies of dual-imaging nanoparticles in biological systems are also very important, which will be conducted in the future. Any *in vitro* stability test of dual-imaging nanoparticles probably cannot fully represent the real biological environments. Here, phorbol myristate acetate (PMA)-treated human monocytes will be used for stability tests. PMA will differentiate monocytes into macrophages,³ which have enhanced nanoparticle uptake capability. After cells were incubated with dual-imaging nanoparticles, cell slides will be prepared for further studies using differential interference contrast (DIC) and confocal microscopy. DIC microscopy has been used to study nanoparticle uptake in living cells,^{4,5} and in our studies, DIC microscopy will be used to localize iron oxide nanoparticles inside cells. Confocal microscopy will be applied to access the fluorescence brightness of the integrated nanoparticles at different incubation time, and thus, to obtain the stability of gold nanoclusters. Therefore, by comparing the DIC images with fluorescent images, the structural integrity of dual-imaging nanoparticles

will be obtained. These results will provide information on the localization of nanostructures inside a cell and demonstrate the potential of the integrated nanoparticles in bio-imaging.

REFERENCES

1. Gagner, J. E.; Shrivastava, S.; Qian, X.; Dordick, J. S.; Siegel, R. W. *J. Phys. Chem. Lett.* **2012**, *3*, 3149-3158.
2. Auffray, C.; Sieweke, M. H.; Geissmann, F. *Annu. Rev. Immunol.* **2009**, *27*, 669-692.
3. Takashiba, S.; Van Dyke, T. E.; Amar, S.; Murayama, Y.; Soskolne, A. W.; Shapira, L. *Infect. Immun.* **1999**, *67*, 5573-5578.
4. Tkachenko, A. G.; Xie, H.; Liu, Y. L.; Coleman, D.; Ryan, J.; Glomm, W. R.; Shipton, M. K.; Franzen, S.; Feldheim, D. L.. *Bioconjugate Chem.* **2004**, *15*, 482-490.
5. Sun, W.; Fang, N.; Trewyn, B. G.; Tsunoda, M.; Slowing, II; Lin, V. S. Y.; Yeung, E. S. *Anal. Bioanal. Chem.* **2008**, *391*, 2119-2125.